UC San Diego
UC San Diego Electronic Theses and Dissertations

Title
High performance RF MEMS metal-contact switches and switching networks

Permalink
https://escholarship.org/uc/item/6qg6x7d6

Authors
Patel, Chirag D.
Patel, Chirag D.

Publication Date
2012

Peer reviewed|Thesis/dissertation

eScholarship.org Powered by the California Digital Library
University of California

UNIVERSITY OF CALIFORNIA, SAN DIEGO

High Performance RF MEMS Metal-Contact Switches and Switching Networks

A dissertation submitted in partial satisfaction of the
requirements for the degree
Doctor of Philosophy

in

Electrical Engineering (Electronic Circuits and Systems)

by

Chirag D. Patel

Committee in charge:

Professor Gabriel Rebeiz, Chair
Professor Prabhakar Bandaru
Professor Brian Keating
Professor Larry Larson
Professor Daniel Sievenpiper

2012

Copyright
Chirag D. Patel, 2012
All rights reserved.

The dissertation of Chirag D. Patel is approved, and it is acceptable in quality and form for publication on microfilm and electronically:

Chair

University of California, San Diego

2012

DEDICATION

To my wife and family, to my parents,
and to my uncle.

EPIGRAPH

Froth at the top, dregs at bottom, but the middle excellent.

—Voltaire

TABLE OF CONTENTS

Signature Page iii

Dedication iv

Epigraph iv

Table of Contents vi

List of Figures ix

List of Tables xv

Acknowledgements xvi

Vita xviii

Abstract of the Dissertation xix

Chapter 1 Introduction 1
- 1.1 MEMS and RF MEMS Technology in Summary 1
- 1.2 Applications of Metal-Contact RF MEMS Switches 6
- 1.3 Considerations for Reliable Metal-Contact Switches 10
  - 1.3.1 The Contact 10
  - 1.3.2 Actuator Design 12
  - 1.3.3 Packaging 14
  - 1.3.4 Electromagnetic Performance 14
- 1.4 Status of the Technology and Dissertation Scope 14

Chapter 2 Stress- and Temperature-Insensitive mN-Force-Level Metal-Contact Switches Based on a Tethered Cantilever Topology 17
- 2.1 Introduction 17
- 2.2 Device Structure 18
- 2.3 Design and Analysis 21
  - 2.3.1 Basic Theory and Device Operation 21
  - 2.3.2 Effects of Stress Gradients, Biaxial Stress, and Temperature 26
  - 2.3.3 Electromagnetic Analysis 29
- 2.4 Fabrication 31
- 2.5 Measurements 33
- 2.6 Conclusion 38

Chapter 3 An Improved Cantilever-Based RF MEMS Switch for High-Power Applications . . . 41
3.1 Introduction . . . 41
3.2 Design . . . 41
3.2.1 Switch Overview . . . 41
3.2.2 Effect of Stopper Dimples . . . 42
3.2.3 Mechanical Design . . . 42
3.2.4 Stress and Temperature Effects . . . 46
3.2.5 Contact Temperature Simulations . . . 46
3.3 Fabrication . . . 49
3.4 Measurements . . . 49
3.4.1 Temperature Measurements . . . 49
3.4.2 Electrical Measurements . . . 49
3.4.3 Reliability and Power Measurements . . . 52
3.5 Conclusion . . . 52

Chapter 4 A Compact Cantilever-Based RF MEMS Switch and Switching Networks . . . 55
4.1 Switch Design . . . 56
4.2 Fabrication and SPST Measurements . . . 59
4.3 Switching Networks . . . 60
4.3.1 Series/Shunt Design and Measurement . . . 60
4.3.2 SP4T Design and Measurement . . . 61
4.3.3 SP6T Design and Measurement . . . 61
4.4 Conclusion . . . 64

Chapter 5 A High-Performance RF MEMS Metal-Contact Switch and Switching Networks . . . 65
5.1 Introduction . . . 65
5.2 Design and Analysis . . . 66
5.2.1 Device Design and Operation . . . 66
5.2.2 Stress and Temperature Effects . . . 70
5.2.3 RF Power Handling Analysis . . . 75
5.2.4 Contact Dynamics . . . 78
5.2.5 Multi-Contact Power Handling Analysis . . . 82
5.2.6 Electromagnetic Analysis . . . 85
5.3 Fabrication . . . 86
5.4 Measurements . . . 88
5.4.1 Temperature Measurements . . . 88
5.4.2 DC Measurements . . . 92
5.4.3 RF Measurements . . . 92
5.4.4 Mechanical Measurements . . . 95
5.4.5 Reliability, Creep, and Power Handling . . . 100

5.4.6 Contact Area 105
5.5 High Performance Switching Networks 107
5.6 Conclusion 110

Chapter 6 Conclusion and Future Work 111
6.1 Summary 111
6.2 Future Work 112
6.3 Summary of Appendices 113

Appendix A Miscellaneous RF MEMS Switching Networks 114
A.1 Compact Double-Pole Double-Throw Switching Networks . 114
A.2 Simulations of a Single-Pole Double-Throw Switch for High Frequency Applications 116

Appendix B High-Q 3-/4-Bit RF MEMS Digitally Tunable Capacitors for 0.8-3 GHz Applications 120
B.1 Introduction 120
B.2 Design 121
B.3 Fabrication 123
B.4 Measurement 124
B.5 Conclusion 126

Appendix C The UCSD Metal-Contact Process in Detail 129

Bibliography 135

LIST OF FIGURES

Figure 1.1: (a) An SEM image of an accelerometer by Analog Devices, and (b) a microphotograph of a micro-mirror by Alcatel-Lucent. 2
Figure 1.2: The electrostatic actuation mechanism. 2
Figure 1.3: Examples of RF MEMS devices - (a) clock-wise from top left: Raytheon, MIT-LL, UCSD, and WiSpry capacitive devices; and (b) Radant (left) and Omron (right) metal-contact switches. 4
Figure 1.4: Typical electromagnetic relays used in NxM switch matrices (left) compared with a packaged Radant MEMS switch (right). 7
Figure 1.5: (a) Switching matrices, as switching elements; (b) wideband front-end receivers, as high linearity tunable attenuator and SPNT switching networks; and (c) passive base-station antennas, as low loss and high linearity phase shifters. 7
Figure 1.6: An illustrated example of the components required to achieve a reliable high-performance RF MEMS metal-contact switch. 11
Figure 1.7: A close-up view of the contact. 11
Figure 1.8: A Survey of contact resistance versus contact force - data from (a) [7] and (b) [8]. 13

Figure 2.1: Top view and cross section of the direct contact switch (z-axis expanded). 19
Figure 2.2: Simplified mechanical model of the tethered contact switch under (a) actuation and (b) release. 22
Figure 2.3: Simplified model for the down-state position and contact force calculations. 22
Figure 2.4: Estimated shape of the deformed beam under actuation voltages of 50-80 V. The z-direction is greatly exaggerated compared to the length. 25
Figure 2.5: The effect of a z-directed stress gradient-(a) linear stress gradient versus a two layer model, and (b) calculated and simulated tip deflection versus stress gradient for the tethered design and a free cantilever. 27
Figure 2.6: Switch properties versus stress gradient-(a) pull-in and release voltage, (b) restoring force, and (c) contact force. 28
Figure 2.7: The effect of biaxial stress and temperature-(a) origin of stress and temperature dependent deflection (α_s and α_m are the coefficients of thermal expansion for the substrate and metal beam), (b) simulated tip deflection vs. stress and (c) vs. temperature. 30
Figure 2.8: (a) Details of switch capacitance, and (b) capacitance components versus feed distance. 31
Figure 2.9: (a) Microphotograph and (b) lumped-element model of the switch. . 32

Figure 2.10: The fabrication process sequence-formation of (a) actuation electrodes, (b) hard metal contact, (c) anchors and dimples, (d) electroplating seed metal and mold, and (e) final device. 33
Figure 2.11: (a) Interferometry profiles of free cantilever test structures and tethered devices and (b) 2-D profiles of the devices. 34
Figure 2.12: Measured and simulated S-parameters for (a) up- and (b) down-state positions. 36
Figure 2.13: (a) Measured tip deflection versus temperature and (b) pull-in and release voltage versus temperature. 37
Figure 2.14: Switch resistance versus voltage on several samples. The resistance is as low as 1.2 Ω with a Au/Ru contact for an unpackaged switch in a standard laboratory environment. 39
Figure 2.15: Pull-in voltage versus time under prolonged actuation conditions. . 39

Figure 3.1: Top view and cross section of the direct contact switch (z-axis expanded). All dimensions in μm. 43
Figure 3.2: A comparison of anchor geometry on beam deflection due to temperature. 44
Figure 3.3: The effect of beam collapse and stoppers on the contact force at V_{act} = 90 V. 45
Figure 3.4: Simulated total contact (top) and release force (bottom) versus stress gradient. 45
Figure 3.5: The simulated thermal behavior of the switch - (a) peak contact temperature versus RF power and (b) temperature distribution (10 W of RF power, 1 Ω/contact). 48
Figure 3.6: Picture of a fabricated device. All dimensions are μm. 50
Figure 3.7: Behavior of the switch versus temperature: (a) measured profile of the switch and (b) measured pull-in and release voltages versus temperature. 50
Figure 3.8: Measured S-parameters: (top) isolation; (bottom) return loss and insertion loss for V_{act}=90 V. 51
Figure 3.9: Measured switch resistance versus actuation voltage for several switches (resistance measured using a 4-wire setup). 53
Figure 3.10: Reliability of several metal contact switches under 2 W of cold-switched RF power and 90 V actuation. The resistance was measured using a 4-wire setup. 53
Figure 3.11: Measured power handling of switch - (a) switch resistance versus time under 2 W of continuous RF power and (b) measured S-parameters before and after 24 hours of continuous actuation under 5 W of RF power. 54

Figure 4.1: Top view and cross section of the RF MEMS metal-contact switch. All dimensions are in μm. 57

Figure 4.2: Simulated (total) contact and release force, F_c and F_r, versus actuation voltage. 58
Figure 4.3: Measured average change in pull-in and release voltage versus temperature. The switches showed negligible hysteresis with temperature. 58
Figure 4.4: Measured and modeled S-parameters of the RF MEMS metal-contact switch. The actuation voltage is 90 V (F_c=380 μN). 59
Figure 4.5: (a) Microphotograph of the RF MEMS metal-contact switch and bottom metallization in series/shunt configuration, and (b) measured and modeled S-parameters. All dimensions are in μm. 60
Figure 4.6: (a) Microphotograph of the RF MEMS metal-contact switch in an SP4T configuration, and (b) measured S-parameters of the metal-contact SP4T switching network. All dimensions are in μm. The isolation performance improves by $\sim$6 dB with all ports terminated with 50 Ω. 62
Figure 4.7: (a) Microphotograph of the RF MEMS metal-contact switch in an SP6T configuration, and (b) measured S-parameters of the metal-contact SP6T switching network. All dimensions are in μm. The isolation performance improves by $\sim$6 dB with all ports terminated with 50 Ω. 63

Figure 5.1: Top view and cross section of the metal-contact switch (z-axis not to scale). All dimensions are in μm. 67
Figure 5.2: Simulated contact and restoring force per contact versus actuation voltage for dimple height, d = 0.25 - 0.35 μm. 68
Figure 5.3: Von Mises stress induced at anchors due to a contact force of 1.5 mN (90 V actuation voltage). 68
Figure 5.4: Pull-in and release voltage versus stress gradient. 71
Figure 5.5: Simulated contact and restoring force per contact versus stress gradient. 71
Figure 5.6: Simulated contact and restoring force per contact versus dimple dimension for various stress gradients (90 V actuation). 72
Figure 5.7: Simulated contact and restoring force per contact versus biaxial stress. 73
Figure 5.8: Simulated contact and restoring force per contact versus dimple dimension for various biaxial stresses (90 V actuation). 73
Figure 5.9: Simulated contact and restoring force per contact versus temperature. The coefficient of thermal expansion of the substrate is assumed to be zero for worst case behavior. 74
Figure 5.10: Contact temperature versus RF power for clean metal contacts (Ru) with various contact forces. 76

Figure 5.11: Contact temperature versus RF power for metal contacts contaminated with a resistive film resulting in a contact resistance of R_c = 0.5 Ω/contact. For R_c = 1 Ω/contact, the temperature increase above T_0 is doubled per (5.7). 78
Figure 5.12: Temperature distribution due to 10 W of RF power passing through the switch with a contact resistance of 0.5 Ω/contact and 1.5 mN of contact force. The oxide is 0.25 μm thick. 79
Figure 5.13: Contact temperature versus the thermal conductivity of the substrate for 10 W of RF power and 1.5 mN of contact force. Assumes 0.25 μm of separating oxide. 79
Figure 5.14: Contact temperature versus the separating oxide thickness (on a silicon substrate) for 10 W of RF power, a contact resistance of 0.5 Ω per contact, and 1.5 mN of contact force. 79
Figure 5.15: Calculated contact position (top) and velocity (bottom) versus time under pull-down conditions for various bias voltages. 81
Figure 5.16: Calculated bounce characteristics for 90 V actuation assuming a purely elastic contact and no adhesion (worst-case behavior). Initial contact is at time = 0 μs. 81
Figure 5.17: Calculated impact force versus actuation voltage assuming a purely elastic contact for Ru-Ru and Au-Au contacts. 83
Figure 5.18: Calculated contact position and capacitance versus time under release conditions. 83
Figure 5.19: Contact temperature versus RF power for clean metal contacts with various contact forces, and current divided evenly into two contacts. 84
Figure 5.20: Contact temperature versus RF power for metal contacts contaminated with a resistive film resulting in a contact resistance of R_c = 0.5 Ω/contact, with current spit evenly between two contacts. 85
Figure 5.21: (a) Origin of lumped element components and (b) the lumped-element model of the RF MEMS contact switch. 87
Figure 5.22: Simulated S-parameters on high-resistivity silicon and quartz. Switch resistance, R_s, taken to be 1 Ω total (0.5 Ω/contact). 87
Figure 5.23: Fabrication sequence of the RF MEMS metal contact switch. 89
Figure 5.24: Microphotograph of fabricated device and bottom electrode. All dimensions are in μm. 89
Figure 5.25: SEM image of fabricated device. All dimensions are in μm. 90
Figure 5.26: Measured profile of the device at 25 and 105C (top), and close-up view of plate (bottom). 91
Figure 5.27: Measured pull-in and release voltages versus temperature. 91
Figure 5.28: Measured switch resistance versus voltage for several devices. . . . 93
Figure 5.29: Measured switch resistance versus DC current. The switches were fully operational after passing 1 A of DC current. 93
Figure 5.30: Emission current for 90 V actuation at 25°C and 85°C. The atmosphere was a standard lab environment with flowing nitrogen. . . . 94

Figure 5.31: (a) Measured and fitted S-parameters with simplified circuit models from 0.1-40 GHz; and (b) expanded view of isolation and insertion loss from 0.1-6 GHz. 96
Figure 5.32: (a) Linearity test setup, and (b) measured IIP3 (top) and IIP2 (bottom). Limited by test setup. 97
Figure 5.33: (a) Harmonics test setup and measured results, and (b) WCDMA signal at the output of a switch and a thru-line (channel power of 2 W). Limited by test setup. 98
Figure 5.34: Test setup and measured mechanical response of the RF MEMS metal contact switch, along with resonant modes predicted by FEM. 99
Figure 5.35: Test setup for creep, reliability, and power handling measurements. 101
Figure 5.36: Reliability of the metal contact switch for 0.1-5 W of RF power and 90 V actuation at 25 ^{o}C (top) and 85°C (bottom). All devices failed as *open*. 102
Figure 5.37: Reliability of the metal contact switch for 10-25 W of RF power and 90 V actuation at 25°C. All devices failed as *closed*. 103
Figure 5.38: Measured s-parameters before and after passing 10 W of RF power continuously for 1 hour. 103
Figure 5.39: Measured pull-in voltage for several devices under prolonged actuation conditions at 25 ^{o}C and 85 ^{o}C. 104
Figure 5.40: Measured switch resistance (top) and pull-in voltage (bottom) under prolonged hold-down conditions (unipolar actuation) and passing 2 W of RF power at 2 GHz. 104
Figure 5.41: SEM image of the bottom contact area of the switch implemented with an Ru/Au contact. The power through the switch was $<$1 mW with $<$1000 cycles. All dimensions in μm. 105
Figure 5.42: SEM images of functional contacts after 1M cycling operations - (a) 10 W, cold-switched, and (b) 500 mW, hot-switched. 106
Figure 5.43: SEM images of failed contacts after 20M cycling operations - (a) 10 W, cold-switched, and (b) 500 mW, hot-switched. 106
Figure 5.44: (a) Microphotograph of SP4T switching network, and (b) measured S-Parameters. All dimensions are in μm. Terminating all ports with 50 Ω will improve isolation performance by $\sim$6 dB. . . . 108
Figure 5.45: (a) Microphotograph of SP6T switching network, and (b) measured S-Parameters. All dimensions are in μm. Terminating all ports with 50 Ω will improve isolation performance by $\sim$6 dB. . . . 109

Figure A.1: (a) A compact DPDT switching network, and (b) measured S-parameters. All dimensions are in μm. 115
Figure A.2: (a) A high-performance DPDT switching network, and (b) measured S-parameters. All dimensions are in μm. 117
Figure A.3: Top view of series/shunt SPDT switching network. All dimensions are μm. 118

Figure A.4: A lumped element model of the SPDT switching network. 118
Figure A.5: Simulated S-parameters of the SPDT. Port 3 is actuated, and Port 2 is isolated. 119

Figure B.1: (a) Micro-photograph of a 4-bit digitally tunable varactor and (b) lumped-element model. The 3-bit version is identical but implemented without BIT 0. All dimensions are in μm. 122
Figure B.2: (a) A comparison of standard and "thick-metal" devices and (b) process sequence for forming the thick metallization. All dimensions μm. 125
Figure B.3: Measured capacitance-voltage behavior of a single switched capacitor co-fabricated with the digitally tunable varactor. 125
Figure B.4: (a) Digitally tuned capacitance states for 3- and 4-bit configurations, and (b) analog tuning range vs tuning state (3-bit design). . . 127
Figure B.5: (a) Parasitic inductance and (b) Q vs digital tuning state. Q is taken at 2 GHz. 127
Figure B.6: Capacitive reactance and Q for min/max capacitances from 0.8 to 4 GHz. 128

LIST OF TABLES

Table 1.1: Performance characterization of switch technologies [1,4] 8

Table 2.1: Simulated[a] parameters of the tethered switch and a free cantilever switch 20

Table 2.2: Measured Mechanical Properties of the Tethered Design (75 V actuation) 35

Table 3.1: Comparison of Switch Properties 47

Table 5.1: Effect of Anchor Design on Switch Performance 72

Table 5.2: Lumped Element Model Parameters 86

Table B.1: Comparison of Varactor Designs 123

ACKNOWLEDGEMENTS

This dissertation would not be possible without the help and support of many people. First, I would like to thank my advisor, Prof. Gabriel Rebeiz. His insights, support, and encouragement have been invaluable - both inside and outside of the lab. Through his efforts and expertise, the Telecomm Integrated Circuits and Systems (TICS) lab is state-of-the-art and we students are never in want - in either equipment or interesting projects. He has instilled a culture of persistence, rigour, and accountability upon the group - general traits which I feel are far more valuable than the specifics of our technical training. This is reflected in the level to which he supports his students; he is proactive in seeking opportunities for students and does not hesitate to advocate for us. His recommendation helped me get my foot in the door at Qualcomm, where I will begin my career. It has been an honour and pleasure working with Prof. Rebeiz.

Next, I would like to thank my dissertation committee members, Prof. Prabhakar Bandaru, Prof. Brain Keating, Prof. Larry Larson, and Prof. Daniel Sievenpiper, for taking time to be at my preliminary, qualifying, and defense exams.

I would also like to express my gratitude to the staff of the Nano3 cleanroom facility at UCSD for all of the support that they have given me, including, Bernd Fruhberger, Larry Grissom, Ryan Anderson, Sean Parks, Xuekun Lu, and Maribel Montero. Also, I would like to thank the undergraduate interns who met me at odd hours of the night for dicing and SEM support.

Next, I would like to thank all of my colleagues here in the TICS group for making this journey a pleasant experience, including Isak Reines, Alex Grichener, Romain Stefanini, Hojr Sedaghat-Pisheh, Berke Cetinoneri, Yusuf Atesal, Mehmet Uzunkol, Ozgur Inac, Fatih Golcuk, Jennifer Edwards, Kevin Ho, Yu-Chin Ou, Yi-Chyun Chiou, Chih-Chieh Cheng, Sangyoung Kim, Woorim Shin, Donghyup Shin, Hosein Zareie, Chenhui Niu, Sang-June Park, Michael Chang, Tiku Yu, Jason May, Mohammad El-Tanani, Rashed Mahameed, Ramadan Al-Halabi, Bon-Hyun Ku, Choul-Young Kim, and Dong-Woo Kang. Their friendships made this journey enjoyable and will make my graduation bittersweet.

Finally, I would like to thank my family for their steadfast support - particularly my wife and my parents, who have each invested considerable time and energy in my

education and personal development. My achievements are possible because of their sacrifices.

Chapter 2 is largely a reprint of material published in *IEEE Transactions on Microwave Theory and Techniques*, 2011; C. D. Patel and G. M. Rebeiz. The chapter also includes some material from *IEEE MTT-S International Microwave Symposium Digest*, 2010; C. D. Patel and G. M. Rebeiz. In both cases, the dissertation author is the primary author of the source material.

Chapter 3 is largely a reprint of material published in *IEEE MTT-S International Microwave Symposium Digest*, 2011; C. D. Patel and G. M. Rebeiz. The dissertation author is the primary author of the source material.

Chapter 4 is largely a reprint of material submitted for publication to *IEEE Microwave and Wireless Components Letters*; C. D. Patel and G. M. Rebeiz. The dissertation author is the primary author of the source material.

Chapter 5 is largely a reprint of material submitted for publication to *IEEE Transactions on Microwave Theory and Techniques*, 2012; C. D. Patel and G. M. Rebeiz. The chapter also includes some material published in *IEEE MTT-S International Microwave Symposium Digest*, 2012; C. D. Patel and G. M. Rebeiz. In both cases, the dissertation author is the primary author of the source material.

Appendix B is largely a reprint of material accepted for publication to *IEEE Microwave and Wireless Components Letters*; C. D. Patel and G. M. Rebeiz. The dissertation author is the primary author of the source material.

This work was supported by the Defense Advanced Research Projects Agency (DARPA) N/MEMS S&T Fundamentals program.

Chirag D. Patel
La Jolla, California
2012

VITA

2001-2005	B. S. E. in Computer Engineering, Academic Minor in Mathematics *Magna cum laude*, University of Michigan, Ann Arbor
2005-2007	Engineer with the U. S. Navy Space and Naval Warfare Systems Center - Pacific, San Diego
2007-2009	M. S. in Electrical Engineering, University of California, San Diego
2007-2012	Ph. D. in Electrical Engineering, University of California, San Diego

PUBLICATIONS

C. D. Patel and G. M. Rebeiz, "An RF-MEMS Switch for High-Power Applications", *IEEE MTT-S Int. Microwave Symp. Dig.*, Montreal, QC, Canada, pp. 1-4, June 2012

C. D. Patel and G. M. Rebeiz, "A High-Reliability, High-Linearity, High-Power RF MEMS Metal-Contact Switch for DC-40 GHz Applications," submitted to *IEEE Transactions on Microwave Theory and Tech.*, May 2012

C. D. Patel and G. M. Rebeiz, "A Compact RF MEMS Metal-Contact Switch and Switching Networks," submitted to *IEEE Microwave and Wireless Components Letters*, June 2012

C. D. Patel and G. M. Rebeiz, "High-Q 3-/4-Bit RF MEMS Digitally Tunable Capacitors for 0.8-3 GHz Applications," accepted to *IEEE Microwave and Wireless Components Letters*, May 2012

C. D. Patel and G. M. Rebeiz, "A High Power (>5 W) Temperature Stable RF MEMS Metal-Contact Switch with Orthogonal Anchors and Force-Enhancing Stoppers," *IEEE MTT-S Int. Microwave Symp. Dig.*, Baltimore, MD, pp. 1-4, June 2011

C. D. Patel and G. M. Rebeiz, "RF MEMS Metal-Contact Switches With mN-Contact and Restoring Forces and Low Process Sensitivity," *IEEE Transactions on Microwave Theory and Tech.*, vol. 59, no. 5, pp. 1230-1237, May 2011.

C. D. Patel and G. M. Rebeiz, "An RF MEMS Switch with mN Contact Forces," *IEEE MTT-S Int. Microwave Symp. Dig.*, Anaheim, CA, pp. 1242-1245, May 2010

S. Park, I. Reines, C. Patel, and G. M. Rebeiz, "High-Q RF-MEMS Tunable Evanescent-Mode Cavity Filter," *IEEE Transactions on Microwave Theory and Tech.*, vol. 58, no. 2, pp. 381-389, Jan. 2010.

ABSTRACT OF THE DISSERTATION

High Performance RF MEMS Metal-Contact Switches
and
Switching Networks

by

Chirag D. Patel

Doctor of Philosophy in Electrical Engineering (Electronic Circuits and Systems)

University of California, San Diego, 2012

Professor Gabriel Rebeiz, Chair

This dissertation presents the design and measurement of high performance RF MEMS metal contact switches capable of achieving mN-level contact and release forces. The switches are designed and demonstrated to be tolerant to a wide range stress effects and temperature.

Chapter 2 presents an electrostatic RF MEMS metal contact switch based on a tethered cantilever topology. The use of tethers results in a design that has low sensitivity to stress gradients, biaxial stresses, and temperature. A switch with a footprint of 160x190 μm^2 and based on a surface-micromachined 8-μm thick gold cantilever with a Au/Ru contact is implemented on a high-resistivity silicon substrate and results in a total

contact force of 0.8-1.2 mN at 80-90 V, a restoring force of 0.5 mN, a pull-in voltage of 61 V, an up-state capacitance of 24 fF, and an actuation time of 6.4 μs. The device achieves a switch resistance of 2.4$\pm$1.4 Ω to 1.8$\pm$0.6 Ω at 90-100 V in open laboratory environments (unpackaged).

Chapter 3 presents a temperature stable metal-contact RF MEMS switch capable of handling >5 W of RF power (a second generation of the tethered cantilever topology). The device achieves 0.7 - 1.5 mN of contact force for actuation voltages of 80 - 90 V, with a restoring force of 0.63 mN. Furthermore, the device is insensitive to stress effects and temperature. Temperature measurements showed excellent thermal stability - no deflection in the beam, and a change in pull-in voltage of only 4 V from 25 - 125 ^{o}C. The switch was tested under prolonged (>24 hrs) high-power RF conditions with excellent reliability.

Chapter 4 presents a compact RF MEMS metal-contact switch based on a tethered cantilever topology and orthogonal anchors. The switch is a ”medium-force” design capable of achieving 0.38-0.72 mN of contact force for actuation voltages of 90-100 V and a restoring force of 0.46 mN (simulated) in a 120$\times$160 μm^2 area. The pull-in and release voltages are 75 V and 70 V, respectively. In the down-state, the switch resistance is 1-2 Ω with a Au/Ru hybrid contact. In the up-state, the capacitance is 16 fF, resulting in an isolation of 20 dB at 10 GHz and 9 dB at 40 GHz for an SPST configuration. Furthermore, the switch demonstrated a reliability of >10 million cycles (1 W, cold-switching) and a power handling of >5 W. For a series/shunt configuration, the switch achieves an isolation of 55 dB at 10 GHz and 35 dB at 40 GHz. Compact SP4T and SP6T switching networks are also implemented. The SP4T is 850$\times$530 μm^2 (850$\times$650 μm^2 with bias pads); the SP6T is 850$\times$730 μm^2 (850$\times$855 μm^2 with bias pads). Both designs achieve an isolation $\sim$36 dB and insertion loss $<$ 0.3 dB at 3 GHz.

Chapter 5 presents a mN-level contact and restoring force RF MEMS metal-contact switch exhibiting high reliability, high linearity, and high power handing for DC-40 GHz applications. The device, which is insensitive to stress and temperature effects, achieves 1.2-1.5 mN of contact force (per contact) from 80-90 V and 1.0 mN of restoring force (per contact). The up-state capacitance is 8 fF, resulting in an isolation of -46, -31, and -14 dB at 1, 6, and 40 GHz, respectively. Measured results show switch re-

sistances of 1-2 Ω and a reliability of $>$100 million cycles at 2-5 W under cold-switching at 100 mW under hot-switching conditions, in an unpackaged and standard laboratory environment. Furthermore, the device was tested under prolonged hold-down conditions and demonstrated excellent RF power handling ($>$10 W) and DC current handling ($>$1 A) capability. Finally, SP4T and SP6T switching networks implemented with the metal-contact switch are demonstrated.

Chapter 1

Introduction

1.1 MEMS and RF MEMS Technology in Summary

Micro-electro-mechanical systems, or MEMS, are electro-mechanical systems fabricated with conventional integrated-circuit (IC) and semiconductor processing technologies. MEMS technology has been conceptualized since the 1950s and has been in active development since the 1970s [1, 2]. The use of IC processing techniques allows MEMS to tightly integrate mechanical and electronic components, enabling the development of sensors and actuators with small size, low cost, and often better performance when compared to conventionally constructed alternatives. Typical applications of MEMS are accelerometers and gyroscopes, pressure sensors, highly-integrated microphones, optical displays, and electronic switches - all with dimensions ranging from less than a μm to several mm. Some examples of MEMS devices are shown in Fig. 1.1 [3].

MEMS is a wide field of study, and there are many different types of MEMS devices. MEMS devices which mechanically manipulate or react to external radio-frequency (RF) or electromagnetic signals (excluding optical and higher frequencies) are broadly called RF MEMS - which itself is also a wide field of study. Within this field, there are micromechanical resonators and filters, acoustic resonators and filters, micromachined electromagnetic structures, and RF MEMS switches and varactors (variable capacitor) [1].

RF MEMS switches and varactors make use of mechanical movement to create

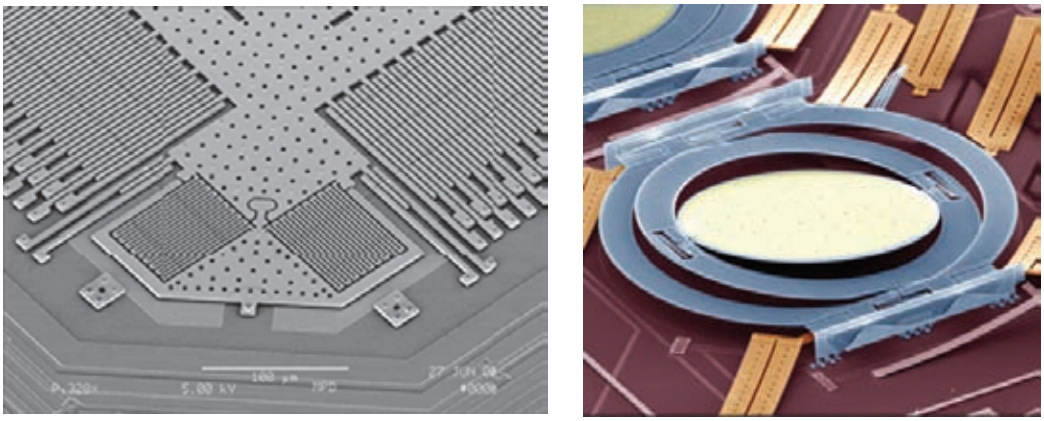

(a) (b)

Figure 1.1: (a) An SEM image of an accelerometer by Analog Devices, and (b) a microphotograph of a micro-mirror by Alcatel-Lucent.

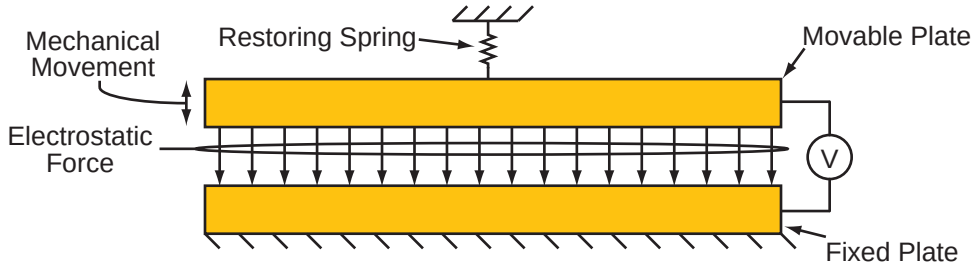

Figure 1.2: The electrostatic actuation mechanism.

open- or short-circuits in the case of switches, and to modulate a capacitance value in the case of varactors. This mechanical motion is achieved by means of electrostatic, magnetostatic, piezoelectric, or thermal actuation. Also, the motion can be either vertical (orthogonal to the substrate) or lateral (parallel to the substrate). While an RF MEMS switch or varactor can be implemented with any combination of actuation mechanism and direction of motion, vertically-actuated electrostatic designs are the most common due to their compact size, simplicity of construction, and near-zero power consumption (illustrated in Fig. 1.2). Fig. 1.3 shows some examples of RF MEMS switches and varactors.

From an electromagnetic perspective, RF MEMS switches come in two varieties: capacitive (Fig. 1.3a) and metal-contact (Fig. 1.3b); while RF MEMS varactors are always capacitive by definition. For this reason, capacitive RF MEMS switches and varactors are often grouped together as capacitive RF MEMS. Capacitive RF MEMS devices typically use a metal-to-dielectric contact, with some form of stand-off to decrease dielectric charging and improve reliability. If the ratio between the minimum and maximum capacitance (capacitance ratio) is large ($>$20), then the device is usually used as a switch. If the capacitance ratio is low ($<$10), then the device functions as a varactor (for devices with analog tuning) or a switched capacitor (for devices with discrete tuning). Due to the capacitive nature of the contact, DC and low-frequency signals are blocked and capacitive switches are usually used at X-band or higher frequencies. However, RF MEMS varactors and switched capacitors can also be used as tuning elements at 0.5-6 GHz. Capacitive RF MEMS devices have certain advantages over FET and PIN diode based switches and varactors in applications such as phase-shifters, tunable filters, and reconfigurable matching networks. These include higher isolation (or tuning range for varactors), linearity, Q, voltage handling (important for tuners), and power handling with lower power consumption and insertion loss. Furthermore, RF MEMS can operate at higher frequencies with better performance than FETs or PIN diodes. However, there are some disadvantages as well: higher costs, greater packaging requirements, larger sizes, slower speeds, and a shorter lifetime. Depending on the specific application, these may or may not be significant drawbacks.

Metal-contact (also called ohmic or direct-contact) RF MEMS switches employ

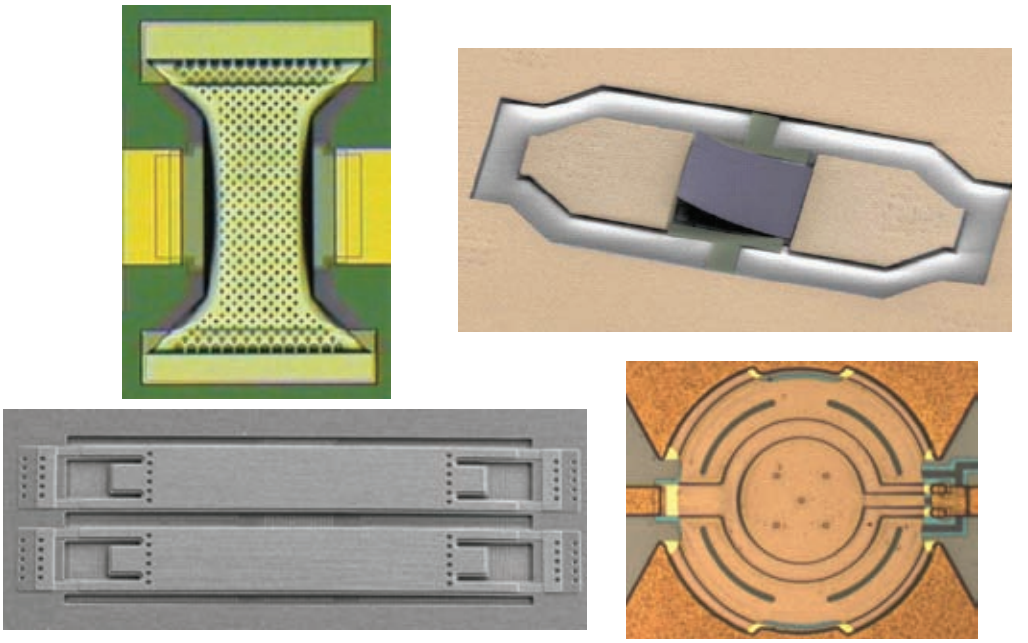

(a)

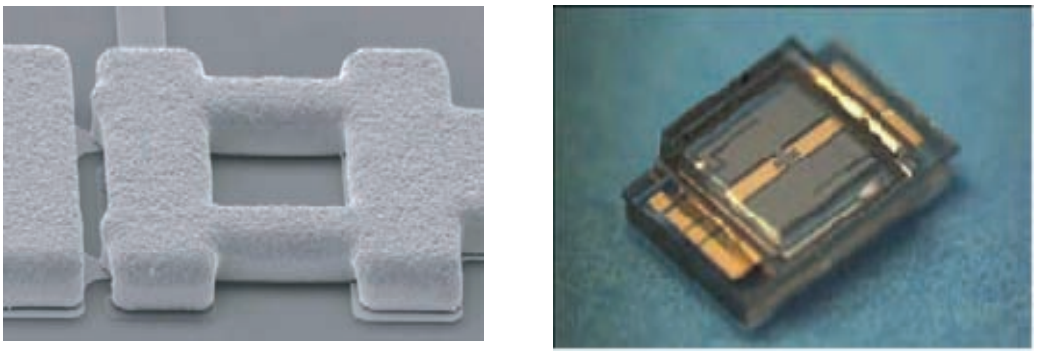

(b)

Figure 1.3: Examples of RF MEMS devices - (a) clock-wise from top left: Raytheon, MIT-LL, UCSD, and WiSpry capacitive devices; and (b) Radant (left) and Omron (right) metal-contact switches.

a metal-to-metal contact and fit the classical definition of a switch - pass broadband electromagnetic signals with low distortion or block them with high isolation as the switch is actuated. Compared to FET- and PIN diode-based switches, metal-contact RF MEMS switches exhibit many of the same advantages and disadvantages as capacitive RF MEMS switches. However, in addition to FETs and PIN diodes, metal-contact RF MEMS switches possess many advantages over conventional ”macroscopic” electromagnetic relays (macro-relays). These include:

1. *Size:* Typical RF MEMS metal-contact switches have dimensions of $\sim$100-200 μm compared to macro-relays which have dimensions of several mm or larger.

2. *Power Consumption:* Electrostatic RF-MEMS designs employ a voltage across a gap to generate a mechanical force with no quiescent current flow, while typical macro-relays use magnetostatic actuation with current flowing through a coil.

3. *Reliability:* Typical macro-relays measure lifetimes on the order of 1-10 million cycles. RF MEMS metal-contact switches have achieved lifetimes measured in billions or even hundreds-of-billions.

4. *Cost:* Even with hermetic packaging requirements more stringent than with macro-relays, the use of semiconductor processing techniques enables low-cost volume production. Packaging can also be performed at the wafer-scale and may result in drastic cost reductions with increasing volumes. Macro-relays are simply unable to take advantage of volume production to this extent.

5. *Performance:* Due to their smaller size, RF MEMS metal-contact switches have less parasitic inductance and better performance at high frequencies. They also have faster switching speeds - on the order of μs instead of ms, as with macro-relays.

Of course, RF MEMS metal-contact switches certainly possess some disadvantages compared to macro-relays:

1. *Insertion Loss:* Macro-relays typically employ contact and release forces of 10 - 100 mN or higher, resulting in very low contact resistances ($<$100 mΩ) even

with refractory-metal contacts. Contact and release forces for RF MEMS metal-contact switches typically range from 100 μN - 1 mN, resulting in typical contact resistances of $>0.5\ \Omega$ for refractory metal contacts such as ruthenium.

2. *Isolation:* Due to the larger size of macro-relays, there is a larger separation between the contacts in the *open*-state, resulting in greater isolation - even at high frequencies.

3. *Power Handling:* Macro-relays have higher power handling than RF MEMS metal-contact switches because of the larger contact and release forces, and because of the lower on-resistance. Furthermore, the contacts of macro-relays are constructed with thicker metal layers. This is especially important for hot-switching applications, where the power is applied during switching events, since the contact is better able to withstand arcing and material transfer.

4. *Sensitivity to Environment:* Since the contact and release forces of RF MEMS metal-contact switches are mN-level or less and the dimensions are micro-scale, certain effects such as humidity and temperature will influence the switch performance. While some effects can be mitigated with good packaging and careful selection of ambient atmosphere (Nitrogen, Argon, etc), others must be solved through device design.

Fig. 1.4 shows a typical set of macro-relays used in defence, aerospace, and satellite systems compared with a commercially available RF MEMS metal-contact switch. Table 1.1 presents a performance summary of solid-state (PIN and FET), RF MEMS, and macro-relay switch technology for comparison.

1.2 Applications of Metal-Contact RF MEMS Switches

There are many applications where the advantages outweigh the disadvantages, and where RF MEMS metal-contact switches can have a significant impact because neither solid-state technology nor macro-relays can meet the requirements. These areas include (Fig. 1.5):

Figure 1.4: Typical electromagnetic relays used in NxM switch matrices (left) compared with a packaged Radant MEMS switch (right).

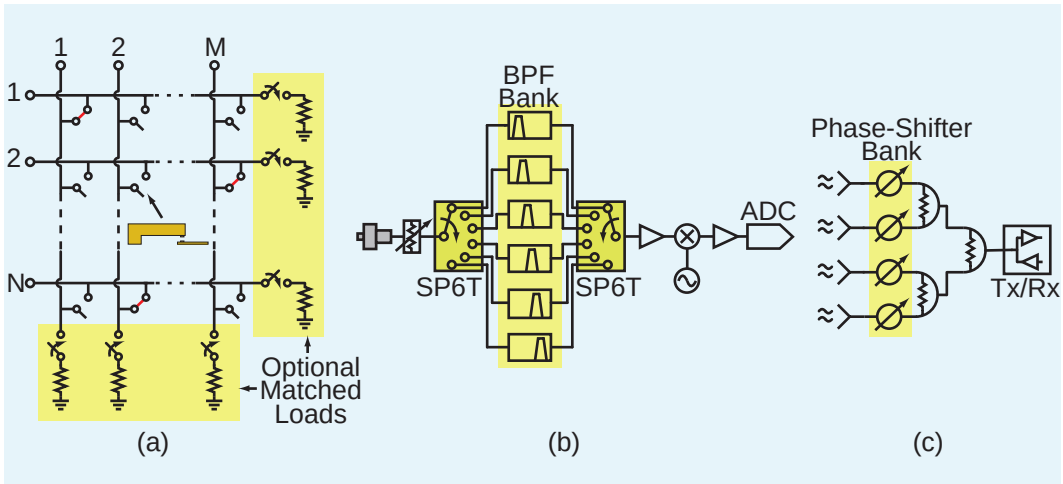

Figure 1.5: (a) Switching matrices, as switching elements; (b) wideband front-end receivers, as high linearity tunable attenuator and SPNT switching networks; and (c) passive base-station antennas, as low loss and high linearity phase shifters.

Table 1.1: Performance characterization of switch technologies [1, 4]

Parameter	PIN	FET	RF MEMS	Macro-Relay
Voltage (V)	$\pm$3-5	3-5	20-100	3-50
Current (mA)	3-20	0	0	50-1000
Power Consumption[a] (mW)	5-100	0.05-1	0.05-1	>100-1000
Switching Time	1-100 ns	1-100 ns	1-300 μs	>1 ms
C_u (fF)	40-80	70-140	2-16	20-20000
R_s (Ω)	2-4	4-6	0.2-1	0.1-0.5
Isolation, 1-10 GHz	High	Medium	Very High	Medium
Isolation, 10-40 GHz	Medium	Low	Very High	n/a
Isolation, 60-100 GHz	Medium	None	High	n/a
Loss, 1-100 GHz (dB)	0.3-1.2	0.4-2.5	0.05-0.2	<0.5[b]
Power Handling, cold (W)	<10	<10	<10	>10-100
Power Handling, hot (W)	<10	<10	<0.1	>10
Lifetime (million cycles)[c]	>>1000	>>1000	1-100	1-10
IIP3 (dBm)	27-50	27-50	66-80+	66-80+
Size	Very Small	Very Small	Small	Large
Integrability	High	High	High	Low

[a]Includes voltage up-converter or drive circuitry.
[b]Loss over the operating frequency range only.
[c]Lifetime is dependent on power levels and whether hot- or cold-switching is used.

1. *Instrumentation:* Automatic Test Equipment (ATE) and wideband electronic instrumentation are ideally suited for RF MEMS metal-contact switches. ATE systems require both DC and RF to pass through switching networks with low loss and good isolation. Electronic instrumentation, such as spectrum and network analyzers, require ultra-wideband (can be as high as DC-67 GHz) switches to provide high port-to-port isolation and to implement high-linearity switched attenuators and switching networks. In these types of systems, RF MEMS is an ideal candidate to replace the low reliability macro-relays or lossy PIN diodes.

2. *Satellite Systems:* In satellite systems, the size and weight savings of metal-contact RF MEMS are very attractive. It currently costs about $20,000/kg to put a payload into space [5], and onboard switching matrices - used for beam forming, signal routing, and redundancy - can consume a considerable amount of weight. Currently, these systems are implemented with macro-relays, but RF MEMS can reduce the payload and improve the reliability to result in higher complexity satellite systems.

3. *Telecommunications Equipment:* Base-stations and microwave communications links can benefit from RF MEMS technology. RF MEMS metal-contact switches can be used to implement new antenna architectures with beam scanning and pattern nulling capabilities (again utilizing RF MEMS based switching networks and matrices). Also, frequency agile RF architectures can be adopted to reduce deployment and maintenance costs. Finally, high performance/high-reliability switching networks and switched filter and amplifier banks based on RF MEMS metal-contact switches can play a critical role in the holy-grail of the telecomm industry - the software defined radio.

4. *Defense Systems:* Defense systems typically prioritize performance and reliability over other factors. RF MEMS can find applications in wide-band transceivers and phased array systems. SPNT switching networks for switched filter banks and transmission lines built with RF MEMS metal-contact switches would exhibit lower loss and higher linearity over traditional solid-state designs.

This list is not exhaustive, and there are other application areas for RF MEMS metal-contact switches such as general low-power switching networks, switched capacitors in wide-tuning range voltage-controlled oscillators (VCOs), and switched inductors.

1.3 Considerations for Reliable Metal-Contact Switches

There are several components required to produce a reliable RF MEMS metal-contact switch (illustrated in fig. 1.6). Although the design of each component requires highly specialized knowledge, for the most part they can be solved separately.

1.3.1 The Contact

The performance of a metal-contact RF MEMS switch is determined primarily by the tribology of the contact area [6]. The size of the contact spot and integrity of the contact material determine most of the main parameters of interest - the switch resistance and insertion loss, power handling, and reliability. Fig. 1.7 depicts a close-up view of two contacting surfaces. It is clear that the real contact spot size is much smaller than the apparent contact spot size (the spot radius is 50-100 nm for typical RF MEMS switches). Increasing the contact force of the switch will increase the size of the contact spot and improve the performance of the switch in all of the aforementioned areas. This, however, can increase the transient impact force and reduce the integrity of the contact material as well as introduce contact bouncing. Furthermore, as metal contacts are closed, a metallic bond can form between the two sides resulting in an adhesion force proportional to the contact force. The opening action of the switch must overcome this adhesion force with its own restoring force. In electrostatic RF MEMS designs, restoring force is typically achieved passively through the mechanical structure of the actuator.

Under high-power conditions, the temperature of the contact can rise significantly due to joule heating and contact materials tend to have greater adhesion as their temperature increases [1, 6]. Harder metals, such as ruthenium, have higher softening temperatures and lower adhesion than softer metals, like gold. Also, harder metals are more robust and can better withstand the cumulative effects of repeated impacts (pitting and hardening) and arcing. On the other hand, softer metals will have larger contact

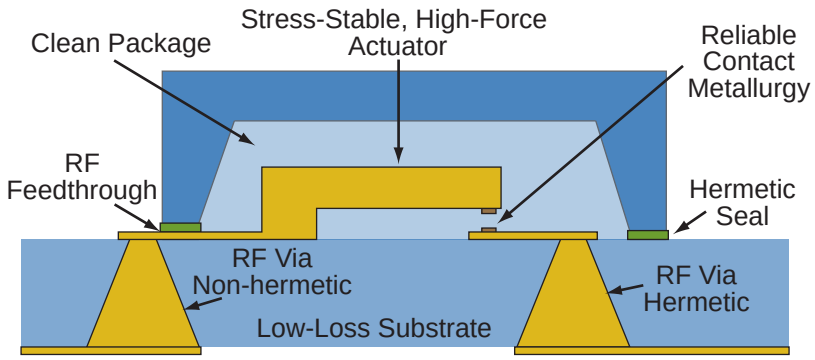

Figure 1.6: An illustrated example of the components required to achieve a reliable high-performance RF MEMS metal-contact switch.

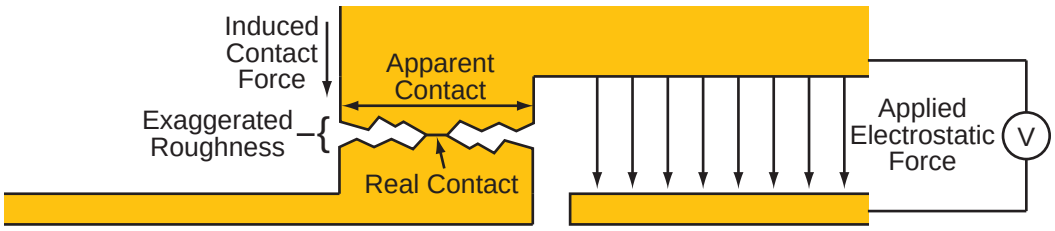

Figure 1.7: A close-up view of the contact.

spots for a given contact force, and will have lower resistance (and lower contact temperatures). There is a tradeoff between contact resistance and contact robustness, and there is no general rule favoring the use of harder or softer metals. Finally, the contact material should not react with the atmosphere or oxidize over the operating temperature range of the switch. Even thin oxide films result in poor resistance because the low contact forces of RF MEMS metal-contact switches are unable to break them. In practice, gold is inert and offers very good performance at low power levels ($<$1 W). However, gold contacts have a high adhesion force (can be higher than the contact force) and gold has a low softening point, making it a poor choice at higher power levels. Recent work has shown that gold contacts covered with a thin ruthenium film are able to achieve excellent contact resistances with little adhesion at mN-level contact forces, and is a good compromise [7]. Figure 1.8 presents a survey of contact resistance versus contact force measurements found in literature.

1.3.2 Actuator Design

In order to ensure reliable operation, actuators which provide mN-level contact forces require mN-level restoring forces. The resulting devices will have large lateral dimensions compared to the gap between the actuator and the pull-down electrode ($>100\times$) - because the electrostatic and contact forces are proportional to the actuator area and inversely proportional to the gap. Temperature and stress effects, such as stress gradients and biaxial stresses, can cause the contact to deflect out-of-plane by a significant fraction of the gap - which will completely change the characteristics of the switch. The actuator must be designed to tolerate all potential stress and temperature configurations. Furthermore, the gap cannot be reduced and the actuation voltage cannot be increased indiscriminately; field emission effects must also be considered. Research shows that for a 0.5 μm gap, the breakdown voltage of air is $\sim$175 V [8].

Under prolonged actuation, the actuator material can creep (a drifting of the material stiffness) due to the induced stresses. Over time, this will cause the switch properties to drift and can result in switch failure if the properties drift by too much. Therefore, the stresses induced by actuation must be minimized by design. Also, dielectrics should not be used in regions with high E-fields due to the dielectric charging

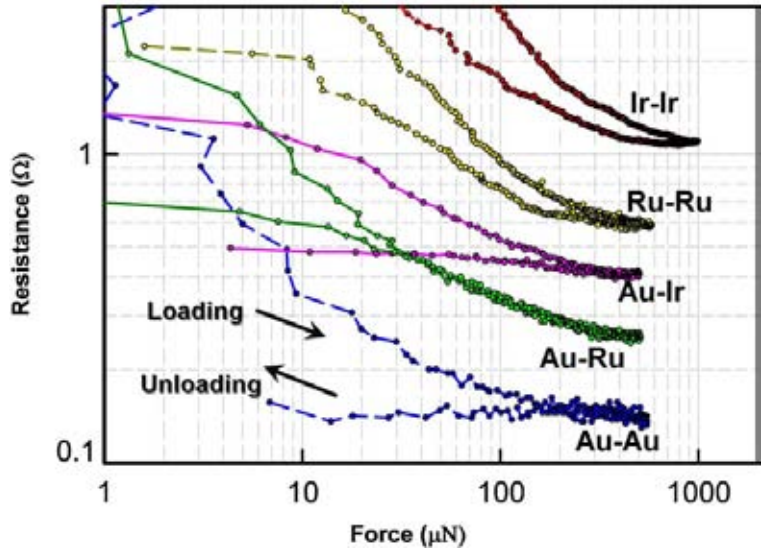

(a)

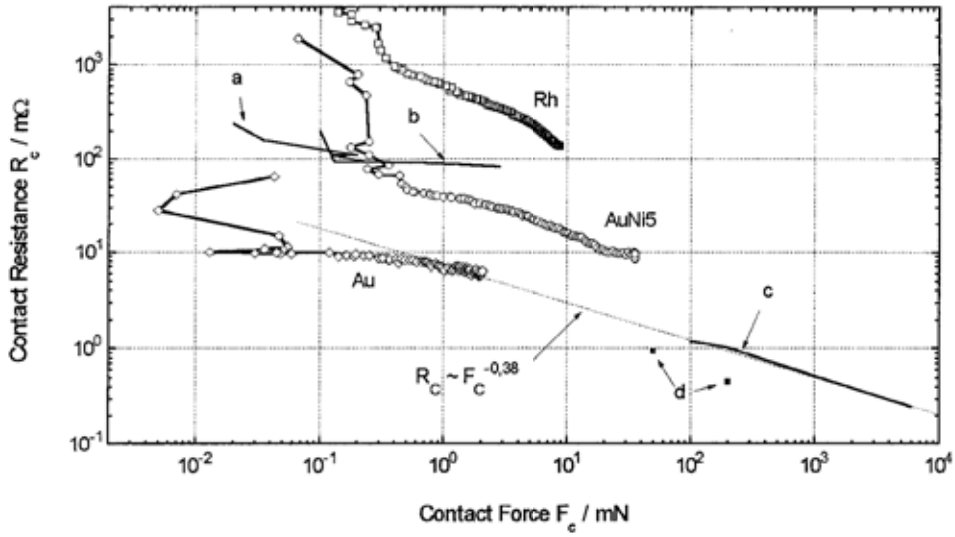

(b)

Figure 1.8: Contact resistance versus contact force - data from (a) [7] and (b) [8].

effect - which will inject a residual charge (and voltage) into a dielectric under high E-fields for prolonged periods of time and result in reduced reliability.

1.3.3 Packaging

Clean hermetic packaging is critical to the development of high-performance metal-contact switches. There are many packaging techniques available for RF MEMS metal-contact switches and they include gold-to-gold thermo-compression, Au eutectic, glass-frit bonding, and wafer-level encapsulation. Prior to sealing the package, the atmosphere is typically flushed and replaced with an inert gas such as nitrogen or argon. Materials known as *getters* are sometimes packaged with the switch to absorb any residual contaminants. Packaging is performed on released structures (actuators) at high temperatures [9–12] so the actuator must not exhibit any permanent deformation or softening.

1.3.4 Electromagnetic Performance

Finally, since RF MEMS metal-contact switches are to be used as electromagnetic relays, the electromagnetic/RF performance of the device must be considered. The capacitance of the switch when the contacts are separated should be minimized. Series inductance and shunt capacitances should be minimized when the contacts are closed. Furthermore, vias and transitions routing signals into and out of the package need to be well matched and have low loss.

1.4 Status of the Technology and Dissertation Scope

There are several examples of reliable RF MEMS metal-contact switches: Omron [13, 14], Radant MEMS [9, 15], Teravicta [16], RFMD [17], Hitachi/Michigan [18, 19], Rockwell Scientific [20, 21], Motorola [22], NEC [23], and many more from various companies and universities [24–31]. To date, there are only two successful commercial examples - the Omron switch, and the Radant switch. This is due to a lack of robust actuator designs (high contact and release forces, insensitivity to stress and

temperature effects, reduced creep effects, etc.) that can be fabricated with an inexpensive process (e.g., surface micromachining). However, with few exceptions, RF MEMS metal-contact switches are limited to medium power applications ($\leq$5 W) - this is primarily due to low actuator forces (contact and release) and the use of gold-gold contacts which are prone to stiction. Current actuator designs are highly susceptible to stress effects and temperature limiting the designs to smaller low-force implementations and to low loss gold contact metallurgies. On the other hand, clean hermetic packaging is a mature technology (with the exception of wafer-level packages) and commonly used by industry; in fact, research has shown that packaging can easily improve the lifetime of an RF MEMS metal-contact switch by 10$\times$ or more [9, 11, 32].

This dissertation is devoted to the development of high-force RF MEMS metal-contact switches which are insensitive to stress effects and temperature, fabricated with a simple surface micromachining process, and use hard-metal contacts. The motivation is to produce high-reliability, high-linearity, high-power handling RF MEMS metal-contact switches and compact switching networks which are compatible with conventional packaging techniques. Two topologies are considered - a tethered cantilever topology and an inverted crab topology. The switches and switching networks are all unpackaged and tested in standard laboratory environments.

Chapter 2 presents a robust mN-force actuator based on a tethered-cantilever topology. The switch is insensitive to the effects of stress gradient, biaxial stress, and temperature. The device, which is fabricated with a surface micromachining technology, achieves low contact resistances with hard-metal contacts (Au-Ru hybrid).

Chapter 3 presents an improved tethered-cantilever switch. The design of the improved switch reduces the switch sensitivity to stress effects and temperature, while simultaneously improving the contact and restoring force.

Chapter 4 presents a compact tethered-cantilever based switch capable of achieving approximately 0.5 mN contact and release forces. The design and analysis examines the effect of contact force on power handling. Compact high-performance switching networks are implemented and demonstrated. The small size and high performance of the switch make it an excellent candidate for mobile applications. Again, the actuator is insensitive to stress effects and temperature.

Chapter 5 presents a robust mN-force actuator based on an inverted crab topology. The switch is insensitive to stress effects and temperature, and can be operated for prolonged periods of time under high-power operation with no degradation in performance. High power handling, linearity, reliability, and robustness of the switch are demonstrated. Finally, high-performance switching newtorks are also demonstrated.

Chapter 2

Stress- and Temperature-Insensitive mN-Force-Level Metal-Contact Switches Based on a Tethered Cantilever Topology

2.1 Introduction

Metal-contact RF MEMS switches are an emerging technology with the potential to replace conventional electromagnetic relays due to their smaller size, higher reliability, and, for electrostatic actuation, lower power consumption [1,21,33,34]. Recently, the Radant MEMS switch was tested to >100 billion cycles at 0.1-10 W of RF power under cold switching conditions [9,15], while the Omron switch was tested to >1 billion cycles [14, 35, 36]. There are several other examples of high performance RF MEMS relays [16–31] but these are still not commercially available. Traditional macro-relays still have an advantage over RF MEMS switches in power handling under cold and hot switching conditions, which is due primarily to the high contact and restoring forces achieved with the macro designs.

It is well known that the power handling capabilities of metal contact RF MEMS switches is limited by the contact material [1]. Refractory metals (such as Ru) can

improve the power handling since they can handle large contact temperatures before softening, but the use of these metals results in larger switch resistances (5-10 Ω for contact forces of 50-200 μN). With mN-level contact forces, however, the contact resistances can drop to <1 Ω with refractory metals [8]. However, a robust mN-level contact force switch must also achieve large restoring forces in order to combat contact adhesion [1, 8]. Furthermore, since the device areas required to generate such forces are large, the device must be insensitive to process variations such as stress gradients and residual biaxial stresses, as well as temperature. The Omron switch is an excellent example of a large contact and restoring force switch that has very low sensitivity to stress effects but is based on a large (1600x1600 μm^2) single-crystal silicon membrane and a wafer transfer process [35].

This chapter presents a novel design capable of achieving mN-level contact and restoring forces based on a thick metal process and reinforcing tethers at the free end of a cantilever [33, 37]. The design results in low sensitivity to stress effects and is capable of achieving low resistances with a Au/Ru contact. The use of tethers has been demonstrated previously with atomic-force microscope probe tips and resulted in cantilevers with increased stiffness and reduced unwanted out-of-plane deflections [38]. The tethered switch achieves the Omron switch design goals (low process sensitivity, high forces) but with the use of a simplified surface micromachining process, such as the Radant MEMS switch.

2.2 Device Structure

The RF MEMS switch is based on an 8 μm thick cantilever beam that is fixed at one end and supported by tethers at the other (Fig. 2.1). The tethers are oriented parallel to the main cantilever to reduce the sensitivity of the device to biaxial stress and temperature, while still allowing a relatively large actuation area (tethers perpendicular to the cantilever result in high sensitivity to biaxial stress and temperature, and should not be used) [40]. This, in turn, results in a large electrostatic force and high contact and restoring forces. Two 0.3 μm thick dimples are used to form the metal-to-metal contact. A set of electrostatically isolated stopper dimples are also formed over the actuation

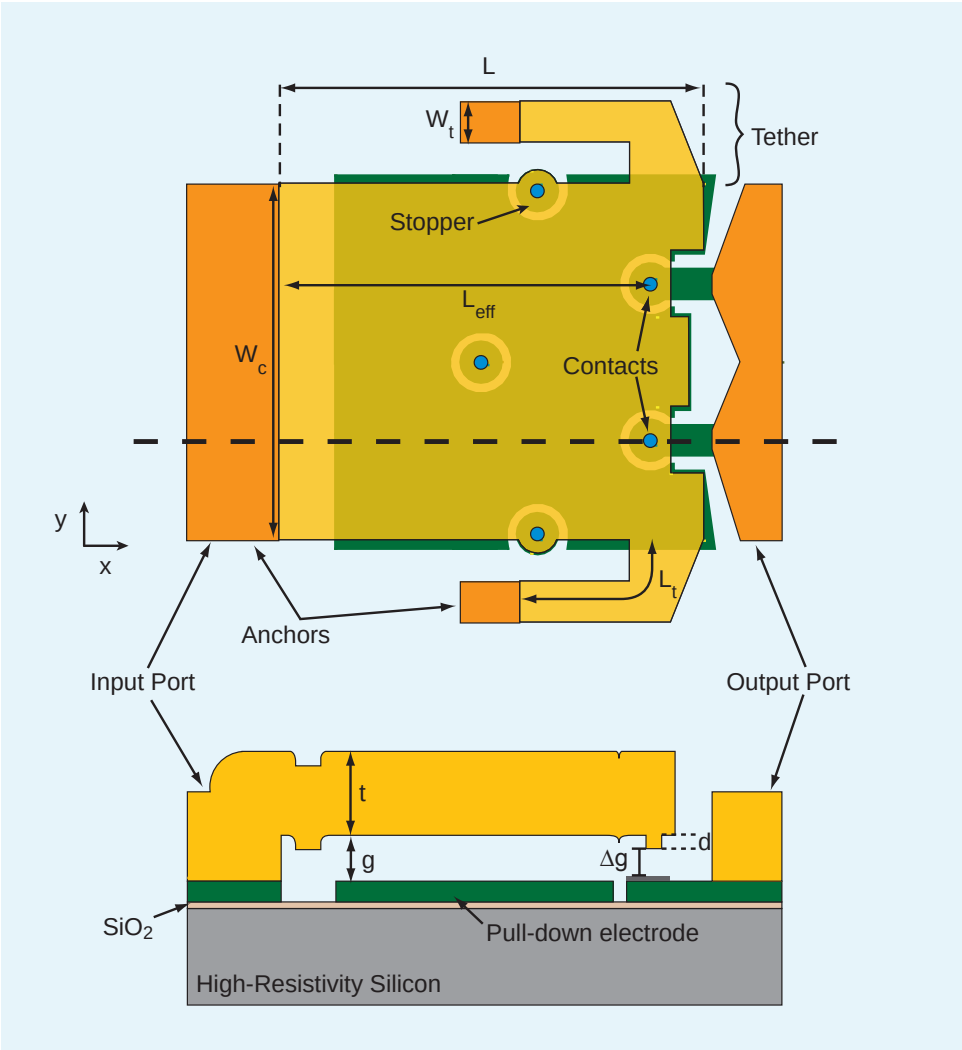

Figure 2.1: Top view and cross section of the direct contact switch (z-axis expanded).

Table 2.1: Simulated[a] parameters of the tethered switch and a free cantilever switch

	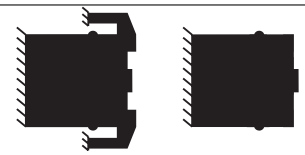	
Length, L (μm)	155	145
Effective Length, L_{eff} (μm)	135	135
Cantilever Width, W_c (μm)	130	130
Tether Length, L_t (μm)	65	-
Tether Width, W_t (μm)	15	-
Thickness, t (μm)	8	12
Gap, g (μm)	0.85	0.85
Dimple Thickness, d (μm)	0.3	0.3
Actuation stiffness, k_a (N/m)	2152	1993
Release stiffness, k_r (N/m)	914	895
Natural stiffness, k_n (N/m)	2341	2094
Resonant frequency, f_r (kHz)	160	130
Mechanical Q	0.65	0.78
Pull-in voltage, V_p (V)	61	64
Release voltage, V_r (V)	53	58
Contact force[b] at 90 V (mN)	1.2	0.8
Restoring force[b] (mN)	0.50	0.49

[a]FEM simulations done with CoventorWare [39].

[b] Contact and restoring forces are listed as total forces. The force per contact is calculated by dividing the total force by two.

area to prevent the beam from touching at high voltages (>100 V). Due to the stopper dimples, a dielectric layer is not needed over the actuation area and the switch can be operated for extended periods of time without suffering from dielectric charging.

Table 2.1 lists the nominal physical and mechanical properties of the fabricated device. The properties are compared to those of a free cantilever designed with similar performance characteristics as well as similar lateral dimensions, gaps, and actuation areas. While the nominal performance of the two devices is similar, it will be shown in Section 2.3 that the tethered cantilever design has significant advantages versus process parameters such as stress gradients and biaxial stresses as well as better temperature performance. This results in higher yields and better process insensitivity.

2.3 Design and Analysis

2.3.1 Basic Theory and Device Operation

Fig. 2.2 shows a simplified 1-D mechanical model of the device under a load (as actuated) and under an adhesion force (as released). It is a free cantilever that is fixed at the base and supported by a spring at its tip. Since the actuation electrode occupies the majority of the area under the beam, the force can be approximated as uniform across the beam for simplicity. For deflections at the tip, the actuation spring constant, k_a, can be calculated using $k_a = k_{c-a} + k_{t-a}$ where k_{c-a} is the spring constant of a cantilever under uniform load and k_{t-a} is the spring constant of the tether for a uniform load on the cantilever. The release spring constant, k_r, is calculated in a similar fashion, but with the spring constants referenced to the tip, rather than uniform loads ($k_r = k_{c-r} + k_{t-r}$). This is the relevant definition under release conditions because the effects of adhesion occur at the contacts (on the tip), for metal contacts. The elastic curve of the system for the actuation and release cases can be obtained by solving (2.1) and (2.2) respectively,

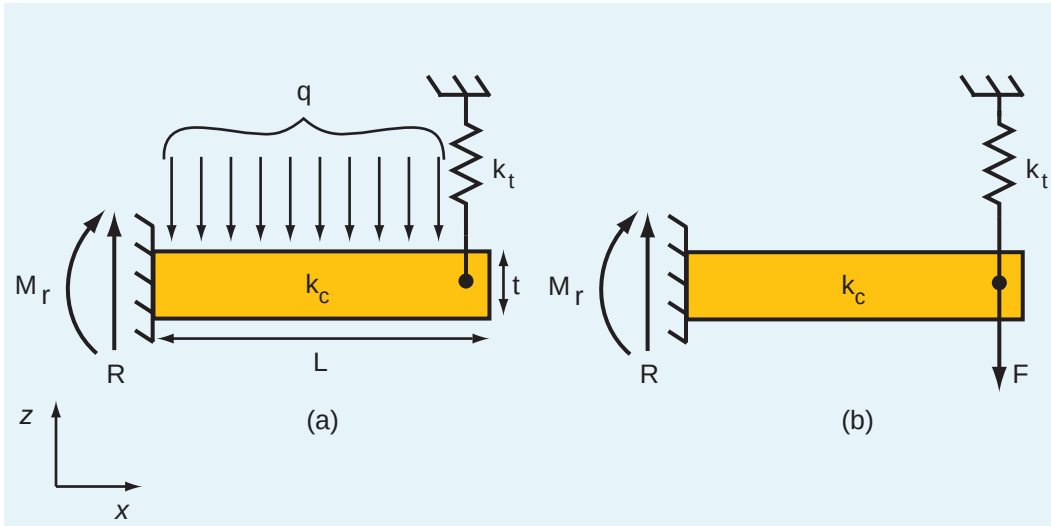

Figure 2.2: Simplified mechanical model of the tethered contact switch under (a) actuation and (b) release.

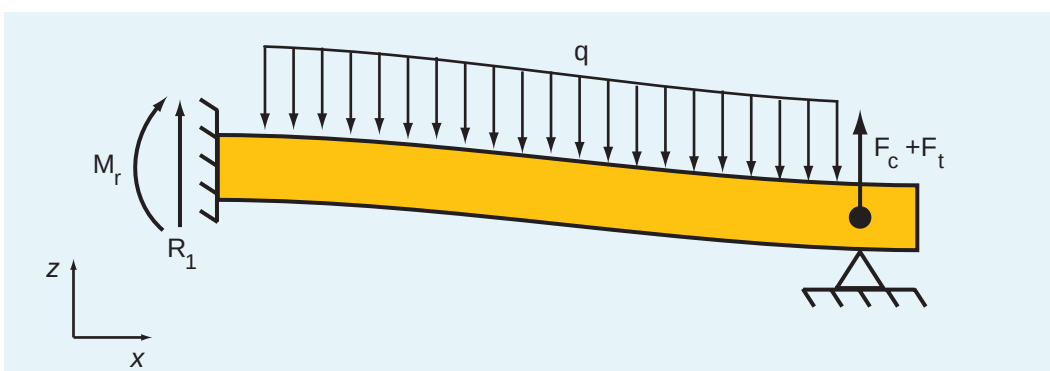

Figure 2.3: Simplified model for the down-state position and contact force calculations.

under the boundary conditions given in (2.3)-(2.6) [41]

$$E_pI\frac{d^2z}{dx^2} = qL(1-\frac{k_{t-a}}{k_a})x - q\frac{x^2}{2} + M_r \tag{2.1}$$

$$E_pI\frac{d^2z}{dx^2} = F(1-\frac{k_{t-r}}{k_r})x + M_r \tag{2.2}$$

$$\frac{dz}{dx}(0) = 0 \tag{2.3}$$

$$z(0) = 0 \tag{2.4}$$

$$z(L) = \frac{qL}{k_a} \qquad (actuation) \tag{2.5}$$

$$z(L) = \frac{F}{k_r} \qquad (release) \tag{2.6}$$

$$k_{c-a} = \frac{2}{3}E_pW_c(\frac{t}{L_c})^3 \tag{2.7}$$

$$k_{t-a} = 2\times\frac{2}{3}EW_t(\frac{t}{L_t})^3 \tag{2.8}$$

$$k_{c-r} = \frac{E_pW_c}{4}(\frac{t}{L_{eff}})^3 \tag{2.9}$$

$$k_{t-r} = 2\times\frac{EW_t}{4}(\frac{t}{L_t})^3 \tag{2.10}$$

$$I = \frac{1}{12}W_ct^3 \tag{2.11}$$

$$E_p = \frac{E}{1-\nu^2} \tag{2.12}$$

where q is the applied distributed force under actuation (Fig. 2.2a) and F is the adhesion force under release (Fig. 2.2b), I is the moment of inertia, E is Young's modulus (taken to be 35 GPa), and ν is Poisson's ratio (taken to be 0.44). M_r is the reaction moment at the base of the cantilever, which must also be solved due to the fact that the system is statically indeterminate. The first term in both (2.1) and (2.2) is the reaction force at the anchor, R. The second term in (2.1) is due to the distributed load. The force is assumed to be evenly distributed under actuation and a point load under release. The stiffness of the main beam and tether are (2.7) and (2.8) under actuation and (2.9) and (2.10) under release, where W_c, L_c and W_t, L_t are the width and length of the cantilever and tether, respectively. Note that $E_p = E/(1-\nu^2)$ is used in (2.1) and (2.2) for the cantilever in accordance to the wide-beam assumption ($L \approx W_c >> t$), while for the tether, E is used since it is narrow compared to its length.

While the 1-D model is a simple representation of the device, it is still useful

for predicting the device operation. It can be seen from (2.1) and (2.2) that the tethers decrease the deflection of the cantilever, thereby increasing the restoring force. For a cantilever beam with dimensions of 155 x 130 μm, (2.7) and (2.9) result in an actuation and release stiffness of k_{c-a} = 520 N/m and k_{c-r} = 290 N/m, respectively. In calculating the release stiffness, the effective length, L_{eff} = 135 μm is used (base-to-contact dimension). For the tether, (2.8) and (2.10) result in k_{t-a} = 1300 N/m and k_{t-r} = 490 N/m for the actuation and release cases, respectively, using an effective tether length of L_t = 65 μm. This results in total spring constants of k_a = 1820 N/m (actuation) and k_r = 780 N/m (release).

The restoring force is calculated using $F_r = k_r \Delta z$. For a clearance of 0.55 μm (a gap of 0.85 μm and contact dimple of 0.3 μm), this results in a restoring force of ~0.4 mN. The pull-in voltage can be calculated using the standard equations for an electrostatic force per unit length,

$$q = \frac{1}{2L} \int_0^L \frac{C(x)V^2}{g(x)}\, dx \tag{2.13}$$

together with (2.1)-(2.6) and iteratively solving the equations until the position of the beam converges or diverges (pull-in condition). For k_a = 1820 N/m, the pull-in voltage is 65 V. The classical equation ($V_p = \sqrt{(8k_a g^3)/(27\epsilon_0 A_a)}$) yields a pull-in voltage of 46 V, where A_a is the actuation area (135 x 130 μm^2).

To calculate the electrostatic and contact forces in the down-state position, the system is simplified to a fixed-simply supported beam (Fig. 2.3). The simple support models the contact plane as well as the force absorbed by the tether. The elastic curve of the new system is given by [41]

$$E_p I \frac{d^2 z}{dx^2} = -\frac{1}{2} q x^2 + R_1 x + M_r \tag{2.14}$$

$$\frac{dz}{dx}(0) = 0 \tag{2.15}$$

$$z(0) = 0 \tag{2.16}$$

$$z(L) = -\Delta g \tag{2.17}$$

where R_1 and M_r are the reaction force and moment at the fixed anchor, respectively. The clearance, Δg, is 0.55 μm. Fig. 2.4 shows the shape of the deformed beam for

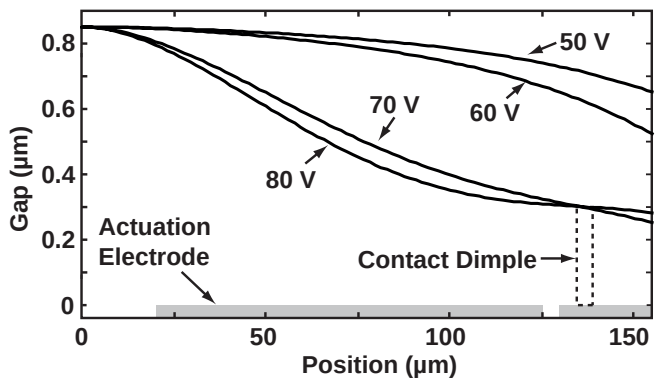

Figure 2.4: Estimated shape of the deformed beam under actuation voltages of 50-80 V. The z-direction is greatly exaggerated compared to the length.

actuation voltages from 50-80 V. The contact force is computed by,

$$F_c = (\frac{qL}{k_a} - \Delta g) \times k_r \tag{2.18}$$

For applied voltages of 70-80 V, the electrostatic force on the beam is 2.5-3.5 mN and the total contact force is 0.6-1.1 mN. The equations also predict that the beam will collapse above applied voltages of 88 V necessitating the use of stoppers to prevent a short circuit between the actuation electrode and the beam. Note that the 1-D model and equations (2.1)-(2.6) make use of several simplifying assumptions and serve only to determine a starting point for precise 3-D FEM simulations.

Finite-element method (FEM) simulations performed using CoventorWare [39] result in a pull-in voltage of 61$\pm$6 V for gaps of 0.85$\pm$0.05 μm. The actuation and release stiffnesses are simulated to be k_a = 2152 N/m and k_r = 914 N/m, respectively. For actuation voltages between 70-80 V, the simulated contact force is 0.5-0.8 mN, and at an actuation voltage of 90 V, it is 1.2 mN. The restoring force is simulated to be 0.5 mN. The stopper dimples, however, do not make contact until the actuation voltages are higher than 100 V, according to the FEM simulations. This is due to the fact that the tethers also have a torsional component that was not modeled, but acts to stiffen the main cantilever and resist collapse. The stopper dimples are still included in the final design in order to protect against failure due to variations in thickness and gap.

2.3.2 Effects of Stress Gradients, Biaxial Stress, and Temperature

The presence of a z-directed stress gradient causes a cantilever beam to curl upwards (for positive gradients) or downwards (for negative gradients). The tip deflection has a significant impact on the performance of the switch. It affects the pull-in and release voltages, the contact and restoring forces, and the usable voltage range of the device. Since stress gradients can vary considerably from run-to-run and process-to-process, a reduction in tip deflections due to stress gradients results in consistent device performance and higher yields.

The tip deflection of a free cantilever, Δz_f, caused by a linear stress gradient, $\nabla\sigma_z$, is given by [1]

$$\Delta z_f = \frac{\nabla\sigma_z L_{eff}^2}{2E_b} \tag{2.19}$$

$$E_b = \frac{E}{1-\nu} \tag{2.20}$$

where, for a two-layer stress model of the beam, $\nabla\sigma_z = (3/2)(\sigma_1 - \sigma_2)/t$. The factor of $3/2$ is needed in order for the two-layer beam model to act as a *linearized* stress gradient (Fig. 2.5a). In the case of the tethered design, the tethers serve to restrict the curling, thus reducing the overall deflection. The deflection of the tethered design can be estimated as

$$\Delta z_t = \frac{k_{c-r}}{k_r}\Delta z_f \tag{2.21}$$

Fig. 2.5b presents the tip deflection versus stress gradient for the devices presented in Table 2.1 calculated with (2.19)-(2.21) and using a full 3-D FEM solver.

Fig. 2.6 presents the FEM simulated device performance versus stress gradients for both the tethered and free cantilever designs. For stress gradients of $\pm$4 MPa/μm, the pull-in voltage is 61$\pm$11 V, and the restoring force is 0.5$\pm$0.15 mN. Furthermore, for actuation voltages of 80-90 V, the contact force is virtually constant at 0.8-1.2 mN versus stress gradients from -2 MPa/μm to +4 MPa/μm (the useable range of stress gradients for the device can be extended with the use of additional stopper dimples). On the other hand, the contact and restoring forces for the free cantilever design are highly dependent on the stress gradient, and the free cantilever is completely unusable for stress gradients $> \pm$2 MPa/μm.

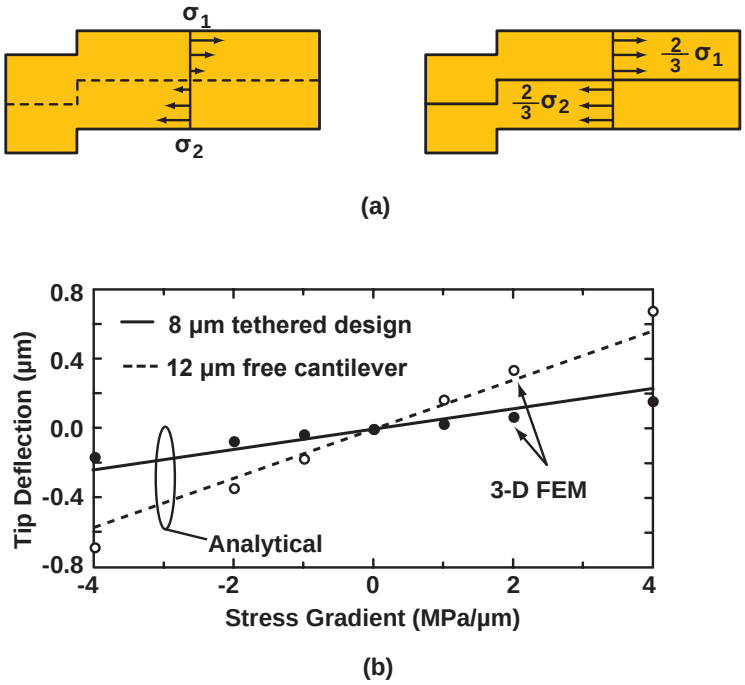

Figure 2.5: The effect of a z-directed stress gradient-(a) linear stress gradient versus a two layer model, and (b) calculated and simulated tip deflection versus stress gradient for the tethered design and a free cantilever.

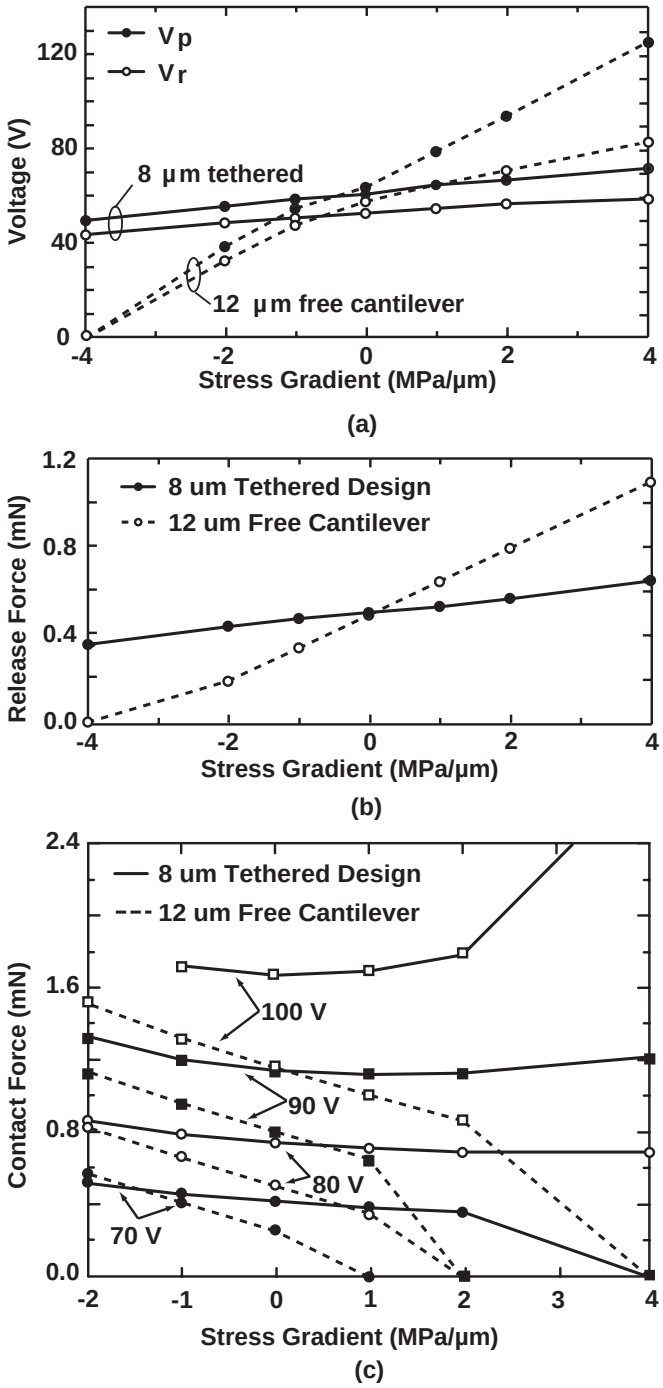

Figure 2.6: Switch properties versus stress gradient-(a) pull-in and release voltage, (b) restoring force, and (c) contact force.

Residual biaxial stresses or temperature changes cause both the substrate and the beam to expand or contract laterally. This results in a tip deflection which is due to material mismatch between the switch (usually gold) and the substrate (usually silicon or quartz), and is proportional to the length of the beam (Fig. 2.7a). The expansion or contraction of the anchors will be constrained by the substrate, giving rise to a launch-off angle (θ in Fig. 2.7a). While the tethers have the same launch-off angle as the main cantilever beam, they are shorter than the main cantilever and so they deflect less. This results in a smaller tip deflection for the tethered device as compared to the free cantilever design, and less sensitivity to deposition conditions and temperature (Fig. 2.7b and c). Note that the FEM simulations assume α_m = 14.1 μm/m·°C (gold) and α_s = 0 μm/m·°C for worst case performance.

The tethered design can be taken to 443°C before the tip touches the contact (0.55 μm deflection), while the free cantilever design can only withstand 266°C before making contact. These simulations are performed assuming a constant E versus temperature. This allows for greater flexibility in the selection of a hermetic packaging process, which can be at temperatures as high as 400°C [9].

2.3.3 Electromagnetic Analysis

A detailed view of the contact area is shown in Fig. 2.8. C_{S1} is the capacitance to the bottom contact while C_{S2} is the capacitance from the cantilever to port 2. The simulated switch capacitance, $C_u = C_{S1} + C_{S2}$ = 26.6-23 fF at D = 15-45 μm. However, D = 45 μm results in a degradation in the thermal properties of the switch [42] and therefore, D = 15 μm was chosen. The switch component, C_{S1}, is 14.9 fF and is composed of a 5.9 fF (C_{pp}) and 9.0 fF (other) component. The feed component, C_{S2}, is 11.7 fF yielding a total capacitance of 26.6 fF. The electromagnetic simulations were performed using Sonnet [43].

Fig. 2.9 presents the complete switch model. The bias network is connected with a high-resistivity line to the voltage source and has negligible impact on the isolation and insertion loss of the switch. The addition of the tethers also has negligible impact on the electromagnetic performance of the switch. The device is implemented in a 50 Ω coplanar waveguide (CPW) configuration with G/S/G = 55/70/55 μm. The CPW gap is

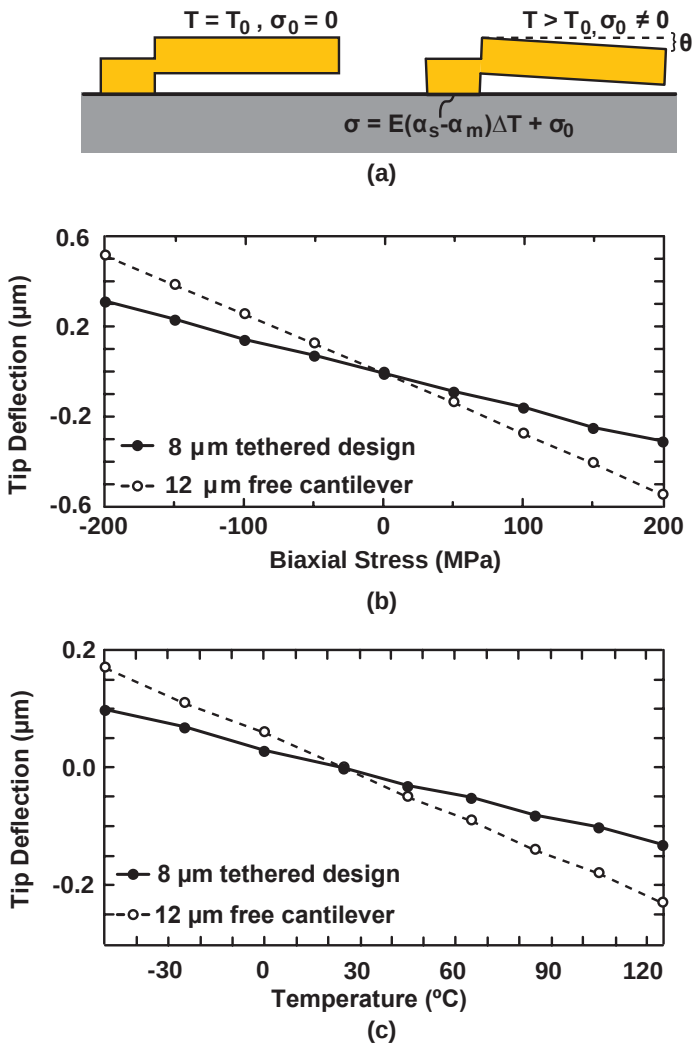

Figure 2.7: The effect of biaxial stress and temperature-(a) origin of stress and temperature dependent deflection (α_s and α_m are the coefficients of thermal expansion for the substrate and metal beam), (b) simulated tip deflection vs. stress and (c) vs. temperature.

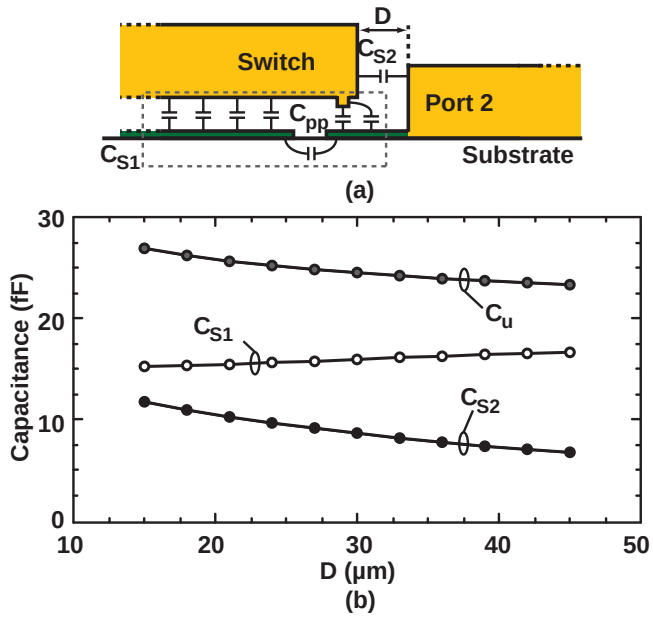

Figure 2.8: (a) Details of switch capacitance, and (b) capacitance components versus feed distance.

increased to 90 μm around the switch in order to maintain the 50 Ω transmission-line impedance over the length of the device.

2.4 Fabrication

The substrate is 2500 Ω-cm silicon with a 2500 $\AA$ thick thermally grown oxide layer (Fig. 2.10). First, the high-resistance bias lines are formed from a 120 $\AA$ thick layer of SiCr using a lift-off process (not shown in figure). Second, a bottom metal layer consisting of a Ti adhesion layer (200 $\AA$) and Au (5000 $\AA$) is sputtered and wet-etched to form the actuation electrode and the base of the anchor (Fig. 2.10a). Then the Ru contact metal (300 $\AA$) is sputtered and patterned with a lift-off process (Fig. 2.10b). A dielectric layer, which serves to protect the bias lines, of silicon nitride is then deposited with PECVD and etched using a reactive ion etching process (RIE, not shown in the figure). The sacrificial layer, composed of a 0.3 μm PMGI layer on top of a 0.55 μm PMMA layer, is spun and patterned (Fig. 2.10c). The dimples are formed by developing the top PMGI layer, while the anchors are formed using RIE to etch through

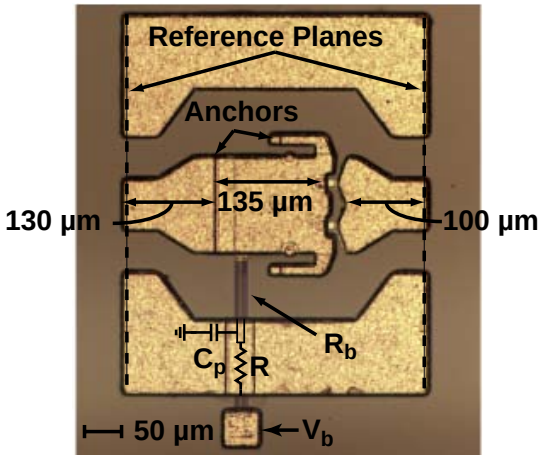

(a)

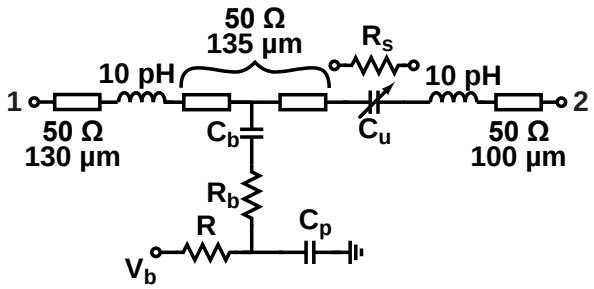

(b)

Figure 2.9: (a) Microphotograph and (b) lumped-element model of the switch.

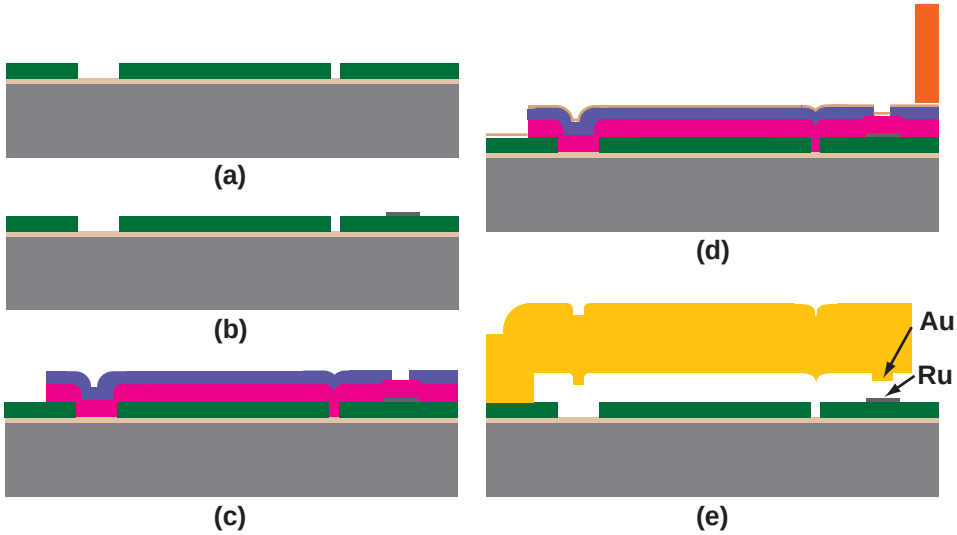

Figure 2.10: The fabrication process sequence-formation of (a) actuation electrodes, (b) hard metal contact, (c) anchors and dimples, (d) electroplating seed metal and mold, and (e) final device.

both layers. Then, an electroplating seed layer consisting of Ti/Au (300/3000 $\AA$) is sputtered (Fig. 2.10d) and selectively electroplated through a photoresist mold. Finally, the electroplating mold, the seed metal layer, and the sacrificial bilayer are removed and the sample is released in a CO_2 critical point dryer (Fig. 2.10e).

A WYKO measurement of the free cantilever test structures and a fabricated device is shown in Fig. 2.11a. The nominal beam thickness was 8.3 μm (8 μm goal) and the nominal gap was 0.82 μm (0.85 μm goal). The tip deflection was obtained using 2-D profiles (Fig. 2.11b). The z-directed stress gradient, $\nabla\sigma_z$, is fitted to the profiles and is +4 MPa/μm. This deflection of the fixed-free cantilevers is $\sim$0.7 μm, while the tethered design has a deflection of $\sim$0.1 μm over a 90 μm distance.

2.5 Measurements

Fig. 2.12 presents the measured and simulated S-parameters from 0.5-40 GHz. In the up-state position, the fitted capacitance is 24 fF with an isolation of 21 dB at 6 GHz. In the down-state, the measured switch resistance is 1.7 Ω (V = 95 V) including

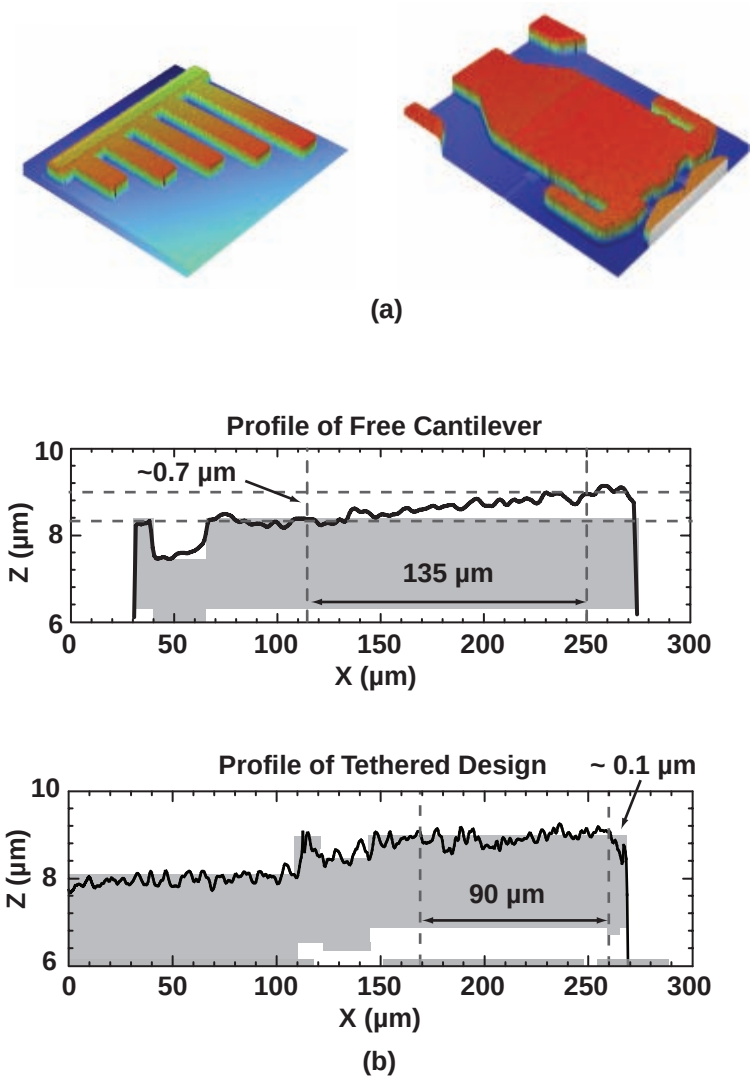

Figure 2.11: (a) Interferometry profiles of free cantilever test structures and tethered devices and (b) 2-D profiles of the devices.

the transmission-line sections ($R_{t-line} < 0.1\ \Omega$). Since the value of R_b is around 60 kΩ, the actuation network can be neglected, and the simplified models shown in Fig. 2.12b are used with good agreement to measured results.

Fig. 2.13a presents the tip deflection of the tethered cantilever versus temperature. The initial deflection at 25°C is due to the stress gradient (Fig. 2.11b). The tip of the device deflects ~55 nm in the z-direction when measured from one end of the actuation electrode to the other ($\Delta l = 90\ \mu m$). From this measurement, we can estimate that the total deflection is 83 nm, since the temperature induced deflection is linear with distance from the anchor. The measured pull-in and release voltages on 10 samples ranged from 58-66 V and 54-60 V, respectively. A representative switch measurement versus temperature is shown in Fig. 2.13b. The measured pull-in voltage is 61-54 V at 25 -105°C, while the measured release voltage is 58-53 V. The data shows that there is no significant hysteresis due to temperature cycling. The measurements are in good agreement with simulated results (not shown).

The mechanical properties of the switch were also tested and are summarized in Table 2.2. The actuation and release times (t_p and t_r, respectively) were calculated by

Table 2.2: Measured Mechanical Properties of the Tethered Design (75 V actuation)

	Simulated (Uniform Load)	Measured
t_p (μs)	5.3	6.4 (8.2 with bounce)
t_r (μs)	3.1	3.6
f_0 (kHz)	160	160
Q_m	0.65	-

solving the equation of motion, given by

$$m_e \frac{d^2 z}{dt^2} + b\frac{dz}{dt} + k_n z = F_e \tag{2.22}$$

where m_e is the effective mass of the switch (2.32 μg under uniform load), b is the damping factor (3.2 mN·s/m), k_n is the stiffness of the beam under uniform load (k_n = 2341 N/m), and F_e is the electrostatic force applied to the beam [1]. The mechanical Q is obtained by solving $Q_m = k_n/(\omega_0 b)$ with $\omega_0 = \sqrt{k_n/m_e}$. The effective mass of the switch was determined by small-signal FEM analysis under a uniform load.

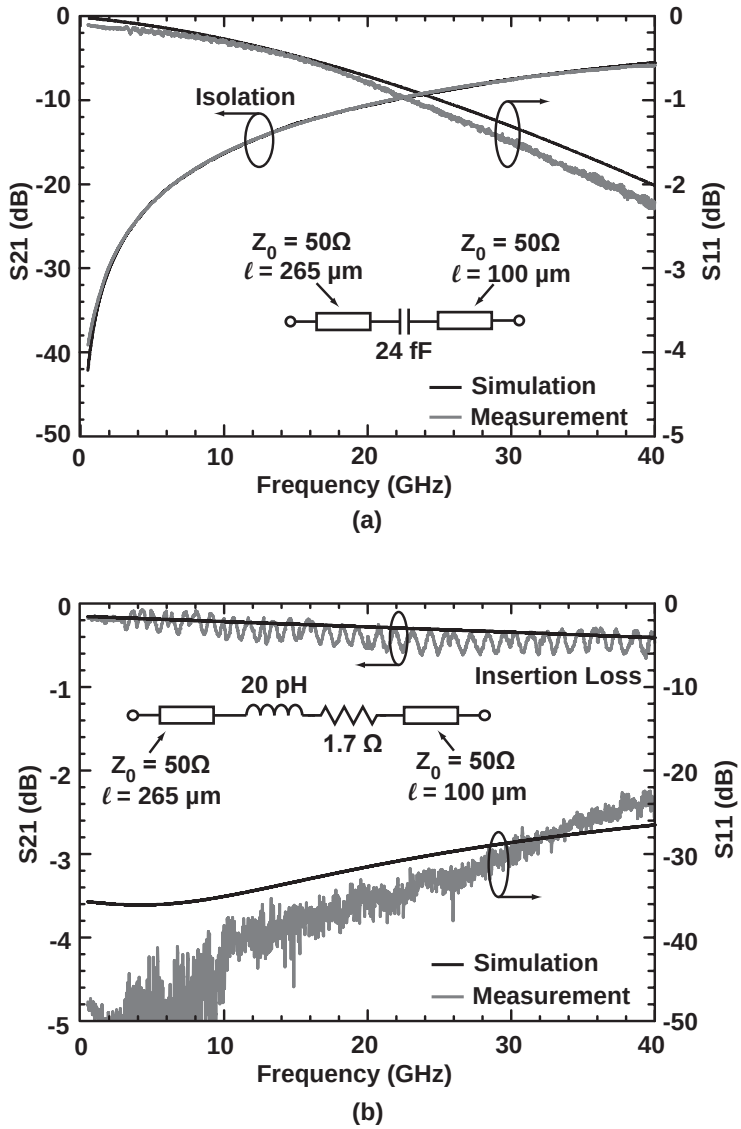

Figure 2.12: Measured and simulated S-parameters for (a) up- and (b) down-state positions.

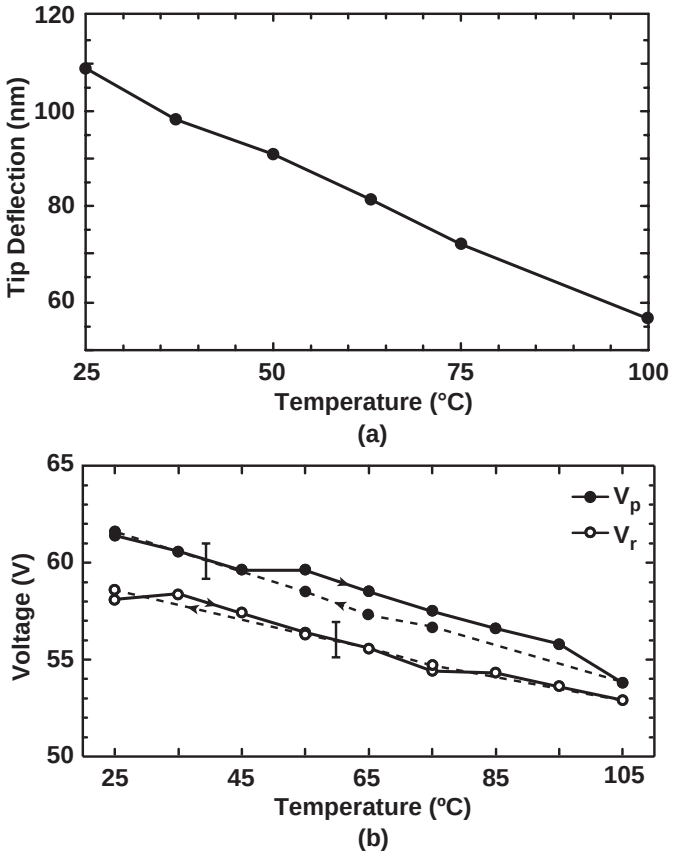

Figure 2.13: (a) Measured tip deflection versus temperature and (b) pull-in and release voltage versus temperature.

The switch resistance was also measured using a 4-wire setup in order to remove interconnect resistances and the test current was limited to 1 mA in order to avoid damaging the Au-Ru metal contacts (Fig. 2.14). The devices were unpackaged and testing was performed in a standard laboratory environment. A switch resistance of 2.4±1.4 Ω to 1.8±0.6 Ω at 90-100 V (1.2-1.8 mN of simulated contact force) was obtained from several samples. The resistance measurements are dominated by the presence of surface contaminants which can be prevented in the future through the use of hermetic packaging.

In order to test the robustness of the switches, the devices were actuated in the down-state position continuously for over 24 hours and were still functional when released (<1 mW RF power test condition). Fig. 2.15 presents the measured pull-in voltage versus time for the high-force switch under prolonged actuation. For this experiment, a pull-in measurement lasting 30 seconds was taken every 10 minutes. In the *stress* state of the measurements, the device was actuated at 90 V for the remainder of the time. In the *relax* state of the measurements, the device was un-actuated (0 V). The measurements show a drift in the pull-in voltage over time due to the prolonged actuation causing creep in the actuator material, while there is a slight recovery when the switch is unstressed with an actuation voltage.

Throughout the course of testing, over 100 devices were tested over a variety of tests with no failures due to contact stiction (even with prolonged continuous actuation). This is due to the use of a Ru contact with a low adhesion coefficient, and the large restoring force of the switch. No high power measurements were done on this device.

2.6 Conclusion

This chapter presents an RF MEMS contact switch capable of achieving mN-level contact and restoring forces. The design does not make use of dielectrics in high field regions and does not suffer from dielectric charging. The use of the tethers enables the device to be insensitive to process variations such as stress gradients and biaxial stresses as well as temperature. Due to the high contact forces, a Au/Ru contact is employed-improving the robustness of the device while still achieving a low switch

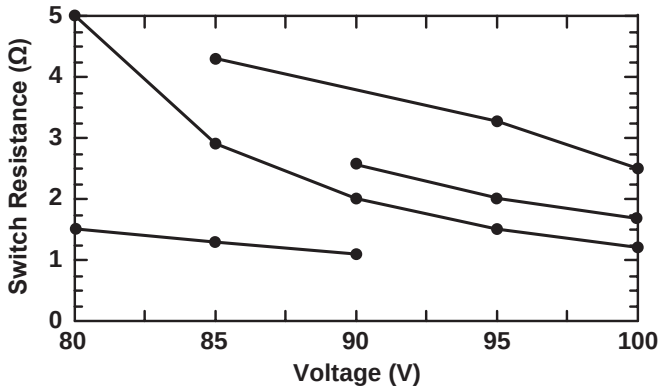

Figure 2.14: Switch resistance versus voltage on several samples. The resistance is as low as 1.2 Ω with a Au/Ru contact for an unpackaged switch in a standard laboratory environment.

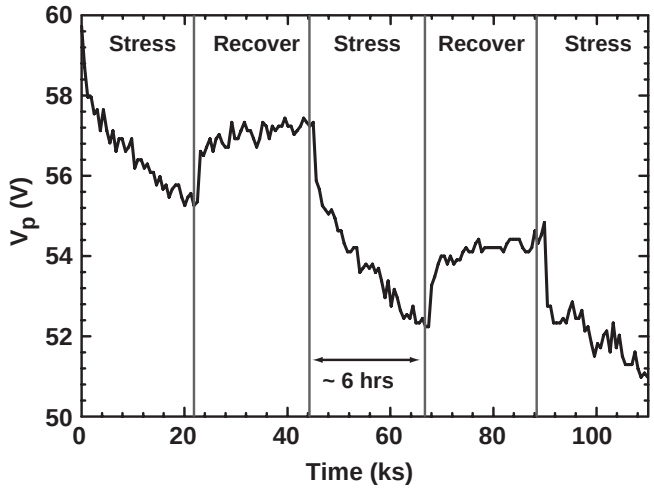

Figure 2.15: Pull-in voltage versus time under prolonged actuation conditions.

resistance in open laboratory settings. Devices were actuated in the down-state continuously for over 24 hours without any failures due to stiction.

This chapter is largely a reprint of material published in *IEEE Transactions on Microwave Theory and Techniques*, 2011; C. D. Patel and G. M. Rebeiz. The chapter also includes some material from *IEEE MTT-S International Microwave Symposium Digest*, 2010; C. D. Patel and G. M. Rebeiz. In both cases, the dissertation author is the primary author of the source material.

Chapter 3

An Improved Cantilever-Based RF MEMS Switch for High-Power Applications

3.1 Introduction

In this chapter, we present the design, fabrication, and measurement results of a second-generation RF MEMS metal contact switch with mN-level contact and restoring forces and high power handling (>5 W) . As in chapter 2, the switch makes use of a tethered cantilever topology [33]. Furthermore, force-enhancing stoppers and orthogonal anchors [44] are employed to achieve higher forces and improved stability versus stress effects and temperature.

3.2 Design

3.2.1 Switch Overview

Fig. 3.1 shows the top view and cross section of the high-force metal-contact switch. The design is based on a tethered cantilever [33], but with its base anchored orthogonally to the plane of bending. This greatly reduces the beam deflection resulting from residual biaxial stresses and temperature [44]. Fig. 3.2 shows the effect of the

anchor geometry on beam deflection due to temperature (the behavior versus biaxial stress is qualitatively similar) - the reduction in deflection is achieved by redirecting the deflection so that it is orthogonal to the direction of the beam and absorbing it into another anchor a short distance away. In order to further reduce the sensitivity of the device to the effects of an out-of-plane stress gradient, the tethers are designed to be stiffer than the main cantilever [33]. The metal contact is formed using a pair of 0.3 μm dimples underneath the cantilever. A set of five isolated 0.3 μm stopper dimples are employed to prevent the beam from shorting with the actuation electrode. No dielectric layer is used over the actuation electrode since the beam, even if collapsed, does not touch the actuation electrode for $V_{act} \leq 125$ V.

3.2.2 Effect of Stopper Dimples

Unlike the switch in [33], the three stopper dimples on the main beam are designed to make contact on isolated islands during normal operation. This creates a much smaller gap between the beam the actuation electrode (0.25 - 0.3 μm) in the area near the contacts and results in a much larger electrostatic force. This translates into a larger overall contact force even if some of this electrostatic force is absorbed by the stopper dimple. Conversely, the two stopper dimples on the tether are not designed to make contact during normal operation and serve to protect the switch in case of severe process variation or stress effects. Fig. 3.3 compares the force versus stress gradient for this design and [33]. The dimensions of the cantilever are the same in both design, but the design presented in this chapter achieves a higher contact force at the same voltage due to allowing the beam to collapse and the use of stopper dimples.

3.2.3 Mechanical Design

Electromechanical simulations were performed using CoventorWare [39]. The simulated actuation spring constant (referenced to displacement at the contact and a uniform load over the actuation area) is 2740 N/m and the simulated release spring constant (referenced to displacement at the contact due to a point load at the contact) is 1140 N/m. The pull-in voltage is simulated to be 68 V. For actuation voltages of 80-90 V,

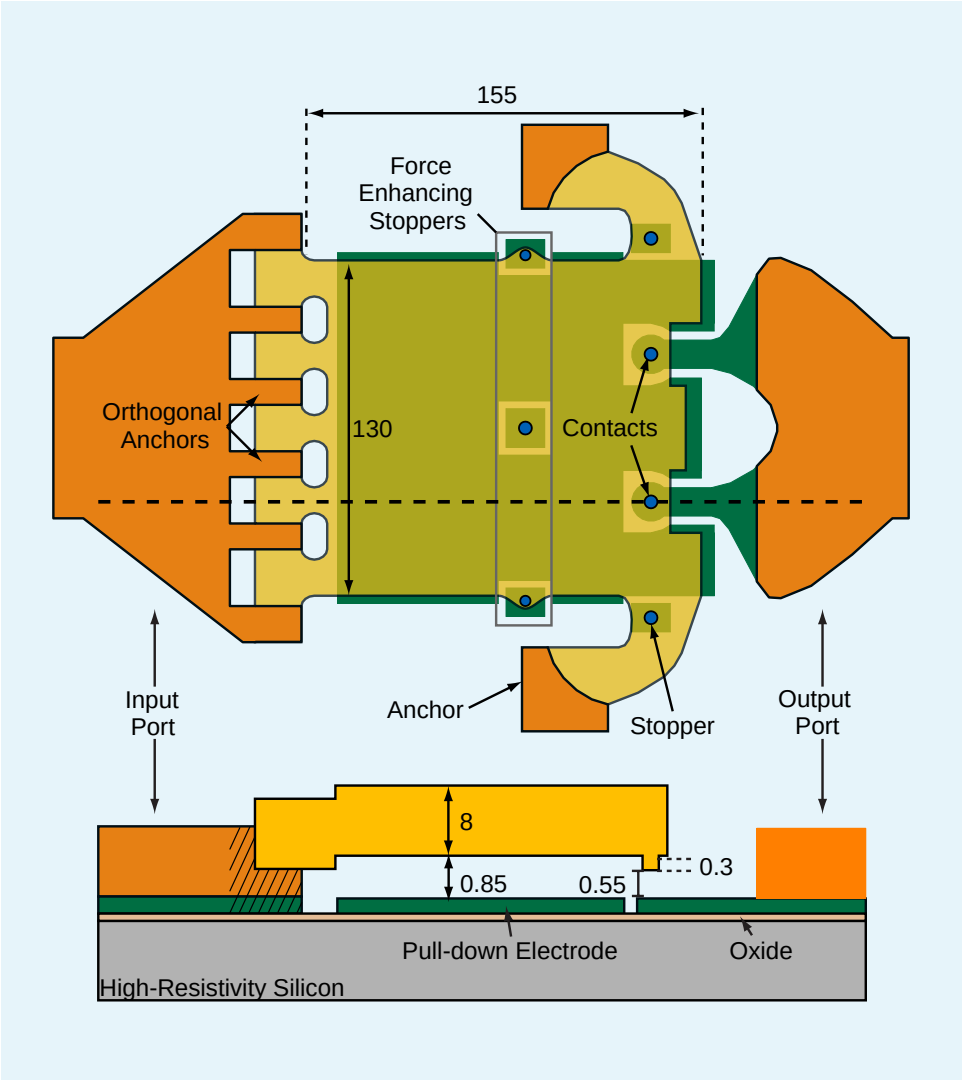

Figure 3.1: Top view and cross section of the direct contact switch (z-axis expanded). All dimensions in μm.

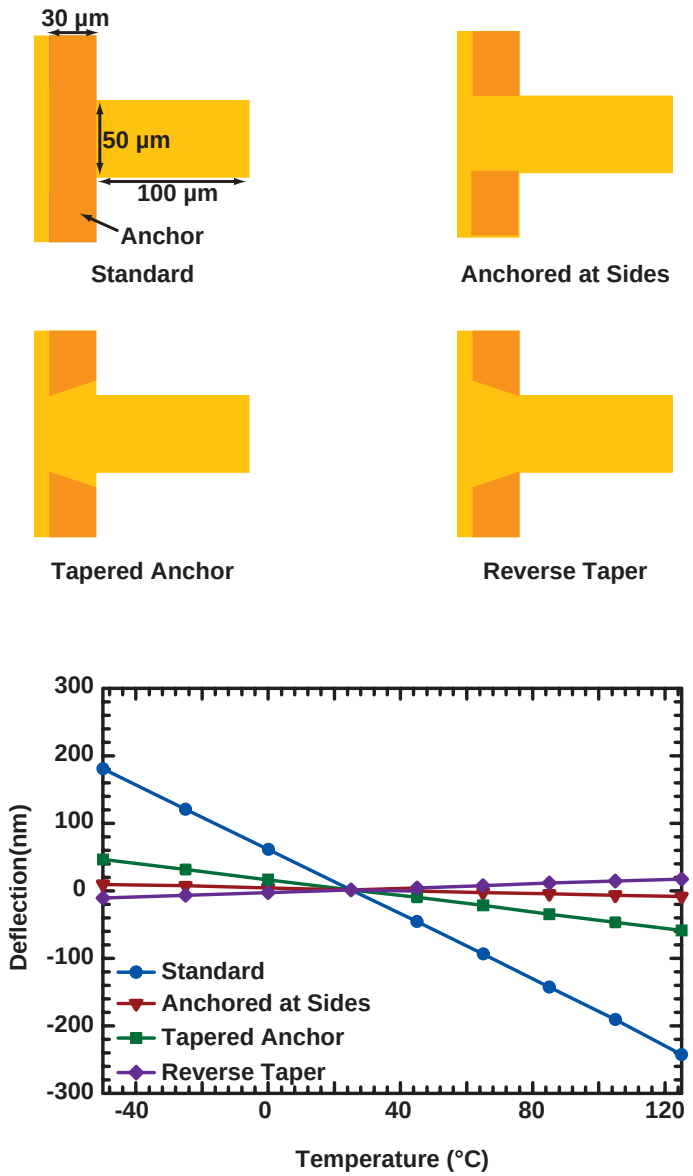

Figure 3.2: A comparison of anchor geometry on beam deflection due to temperature.

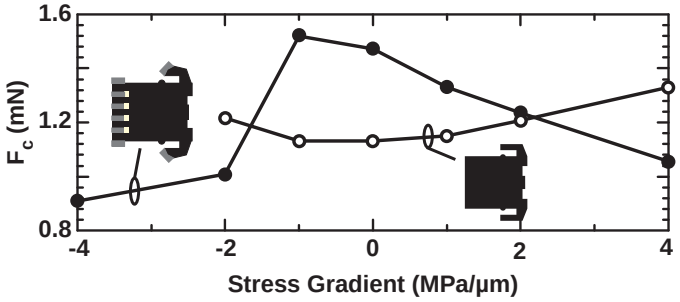

Figure 3.3: The effect of beam collapse and stoppers on the contact force at V_{act} = 90 V.

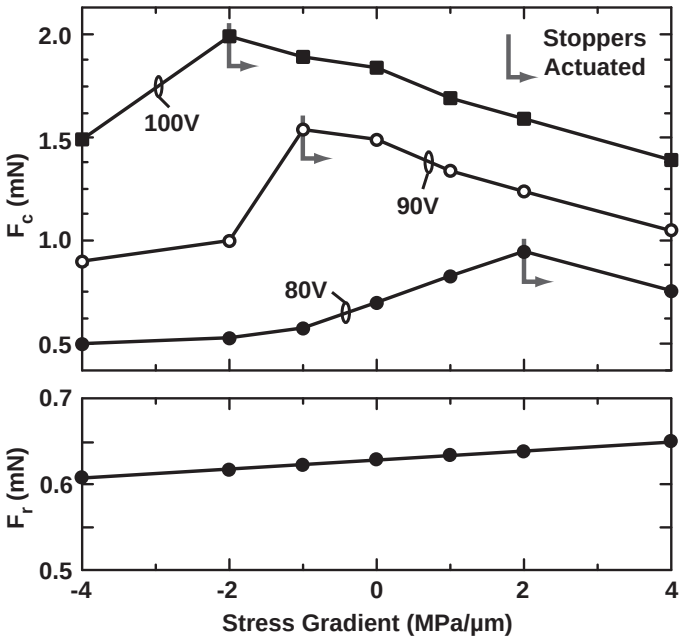

Figure 3.4: Simulated total contact (top) and release force (bottom) versus stress gradient.

the simulated total contact and release force is 0.7 - 1.5 mN and 0.63 mN, respectively, and the simulated mechanical resonant frequency is 160 kHz, the mechanical Q is 0.5, and the switching time is $\sim$5 μs for an actuation voltage of 90 V.

3.2.4 Stress and Temperature Effects

The deflection at the contact due to stress gradients is simulated to be $\pm$18 nm for stress gradients of $\pm$4 MPa/μm. The tethers prevent the contact area from deflecting significantly and instead transfer the maximum deflection point to the center of the beam (where it is $\pm$107 nm for gradients of $\mp$4 MPa/μm). Fig. 3.4 shows the simulated contact and release force for various actuation voltages versus stress gradient. At 90 V actuation, the contact force varies from 0.9 - 1.1 mN for stress gradients of $\mp$4 MPa/μm with the maximum force of 1.4 - 1.5 mN occurring between stress gradients of $\pm$1 MPa/μm. The contact force versus stress gradient is not monotonic due to the effect of the stoppers. The restoring force varies from 0.61 - 0.65 mN.

The deflection of the contact due to residual biaxial stresses and temperature is negligible. For σ=200 MPa, the deflection is +11 nm at the contacts. For a temperature change of 100 ^{o}C, the deflection is -2 nm at the contacts. In both cases, the maximum deflection is at the tip (instead of the center of the cantilever as with the deflection due to stress gradients), so this small deflection results in μN-level changes in the contact force at 80 - 100 V actuation. Similarly, the restoring force is essentially constant, changing by only +13 μN and -2 μN for the 200 MPa case and 100 ^{o}C case, respectively. Table 3.1 presents a comparison between the proposed temperature stable high-force switch, the switch presented in [33], and a high-force design based on a fixed-free cantilever. It is seen that this work achieves much lower sensitivity to stress gradients and temperature.

3.2.5 Contact Temperature Simulations

At high RF powers, the power handling of metal-contact RF MEMS switches is primarily determined by the temperature and localized heating effects at the contact spot. The heat is generated in a small (constriction) region at the metal-metal interface,

Table 3.1: Comparison of Switch Properties

Length (μm)	155	155	145
Width (μm)	235	190	130
Thickness (μm)	8	8	12
Release stiffness (N/m)	1140	914	895
Resonant frequency (kHz)	160	160	130
Mechanical Q	0.5	0.65	0.78
Pull-in voltage, V_p (V)	68	61	64
Contact force[a] at 90 V (mN)	**1.5**	1.2	0.8
Restoring force[a] (mN)	**0.63**	0.50	0.49
Deflection (ΔT=100°C) (nm)	**-2**	-130	-230
Deflection ($\nabla\sigma$=4MPa/μm) (nm)	**18**	160	680

[a] Contact and restoring forces are listed as total forces, simulated with FEM analysis [39].

and the temperature is given by [6],

$$T = \sqrt{\frac{V^2}{4L} + T_o^2} \tag{3.1}$$

where T is the contact temperature, V is the voltage drop across the contact, T_o is the ambient temperature, and L is the Lorenz number (2.44 x 10^{-8} (V/K)^2). T_o is the ambient temperature. Fig. 3.5a presents the peak contact temperature calculated using (3.1) for various RF power levels in a 50 Ω system and a contact resistance of 0.5 - 1 Ω/contact. The temperature distribution of the switch is shown in Fig. 3.5b. The heat is dissipated mostly through the switch and not the substrate due to the oxide layer (Fig. 3.1), which is a thermal insulator and reduces the heat dissipation through the substrate.

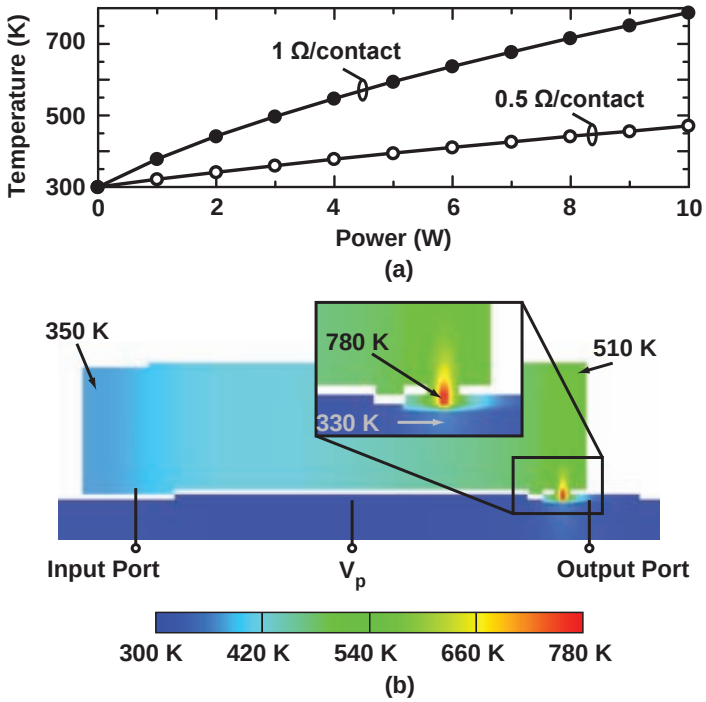

Figure 3.5: The simulated thermal behavior of the switch - (a) peak contact temperature versus RF power and (b) temperature distribution (10 W of RF power, 1 Ω/contact).

3.3 Fabrication

The fabrication procedure follows the process of [33]. Fig. 3.6 presents an optical image of a fabricated device. From fixed-free cantilever test structures, the stress gradient was found to range from -0.3 to +3.3 MPa/μm around the wafer, with the majority of the profile measurements resulting in stress gradients $\sim$2 MPa/μm (a deflection of $\sim$0.23 μm for a 115 μm beam length). The metal contact switch, however, shows a measured deflection of $<$50 nm over a 125 μm beam length (Fig. 3.7a).

3.4 Measurements

The metal contact switches were tested unpackaged in a standard laboratory environment without atmospheric control, but with flowing nitrogen gas to reduce the effects of humidity. The pull-in voltage at room temperature was measured to be 68 V $\pm$ 3 V on several devices. The switching time was measured to be 4.9 - 3.5 μs for actuation voltages of 75 - 100 V and the release time was measured to be 2.3 μs.

3.4.1 Temperature Measurements

The switches exhibited very little deflection versus temperature (Fig. 3.7a) and the pull-in and release voltages are 69 - 65 V and 69 - 62 V, respectively, over a 100 ^{o}C temperature change (Fig. 3.7b). Since the measured profiles show no significant deflection due to temperature, the change in the pull-in voltage must be due to softening of the gold at high temperatures (thus reducing k) or dielectric charging in the oxide layer underneath the actuation electrode.

3.4.2 Electrical Measurements

Electromagnetically, the device is almost identical to [33] and is simulated using Sonnet[1]. Fig. 3.8 shows the measured and simulated S-parameters from 0.1 to 40 GHz with C_u = 24 fF and R_s = 0.4-1.7 Ω. In this simplified model, the transmission line formed by the cantilever is lumped together with the input feed.

[1] Sonnet version 12.02, Sonnet Software Inc.

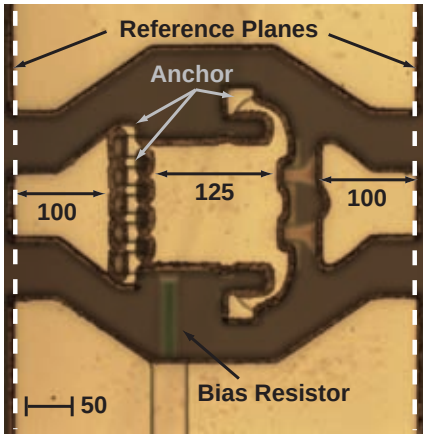

Figure 3.6: Picture of a fabricated device. All dimensions are μm.

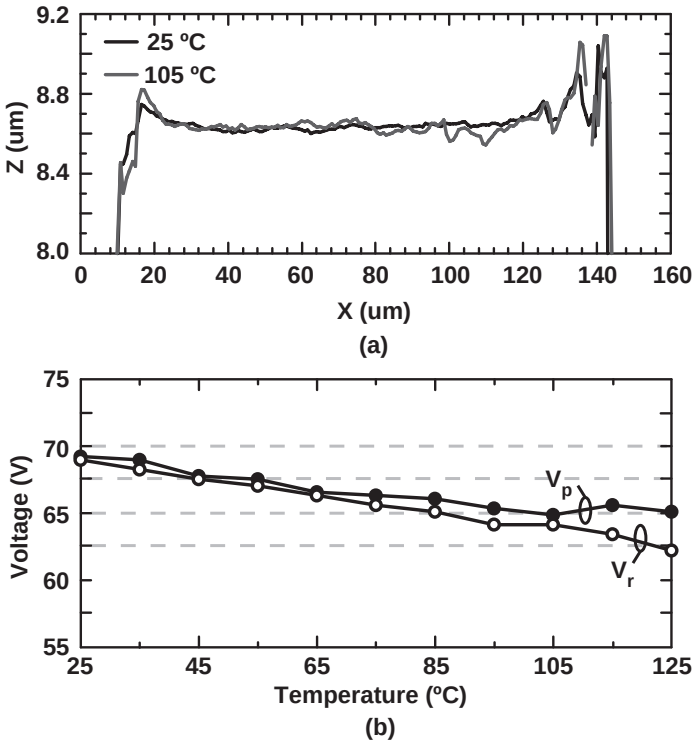

Figure 3.7: Behavior of the switch versus temperature: (a) measured profile of the switch and (b) measured pull-in and release voltages versus temperature.

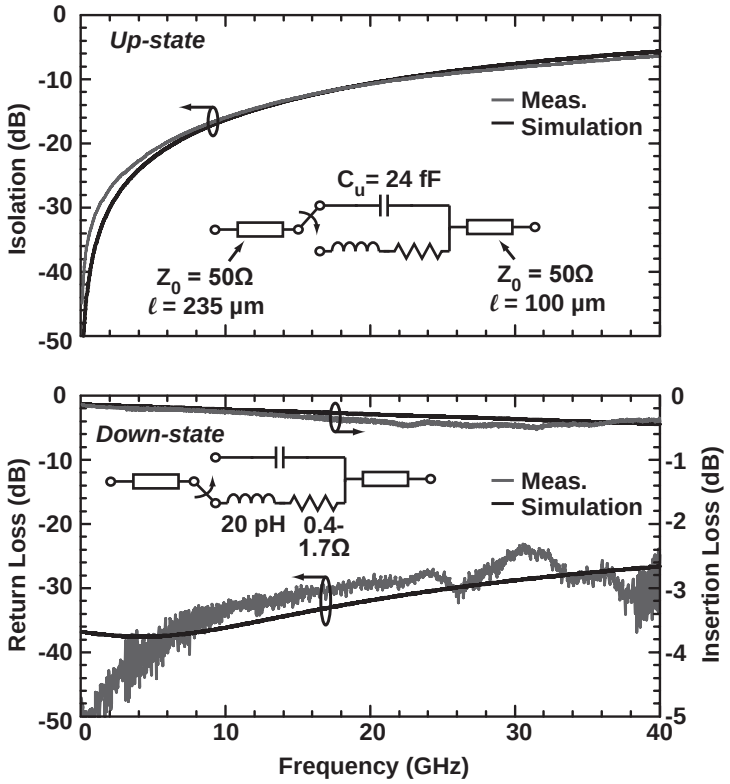

Figure 3.8: Measured S-parameters: (top) isolation; (bottom) return loss and insertion loss for V_{act}=90 V.

The switch resistance was also measured using a 4-wire setup, resulting in resistances from 1.7 - 0.4 Ω for actuation voltages of 75 - 100 V over several devices with a Au-Ru contact (Fig. 3.9). The spread in resistance is due to the open-air test conditions.

3.4.3 Reliability and Power Measurements

The reliability of the switch was tested under cold-switching conditions with an RF power of 2 W at 10 GHz (Fig. 3.10). The test was performed with a switching frequency of both 5 kHz and 10 kHz, and 50% duty cycle, with no significant difference in the reliability outcome. The switches demonstrated a reliability of $>$ 100 million cycles and failures were due to contamination (failed as open circuit).

The power handling of the switch was tested using a prolonged hold-down test (Fig. 3.11). In this test, the device was actuated and held down for several hours with 2 - 5 W of RF power passing through the switch. The evolution of the switch resistance versus time as the switch is continuously actuated for 32 hours under 2 W of RF power at 10 GHz is shown in Fig. 3.11a. Fig. 3.11b presents the measured S-parameters of another switch after 24 hours of continuous actuation with 5 W of RF power at 10 GHz. In this case, the evolution of the switch resistance could not be measured due to the power limitations of the bias networks in the test setup. In both cases, the tests were terminated due to time constraints and not device failure.

3.5 Conclusion

A high power (>5 W) RF MEMS metal contact switch has been demonstrated. The switch uses orthogonal anchors at the base of its cantilever to reduce sensitivity to residual in-plane stress and temperature. It uses tethers at the cantilever tip to reduce the sensitivity to stress gradients and stoppers to enhance the contact force. The design achieves mN-force levels at 90 V. The switch is mechanically robust up to 125 ^{o}C and was shown to be reliable under prolonged high-power test conditions.

This chapter is largely a reprint of material published in *IEEE MTT-S International Microwave Symposium Digest*, 2011; C. D. Patel and G. M. Rebeiz. The dissertation author is the primary author of the source material.

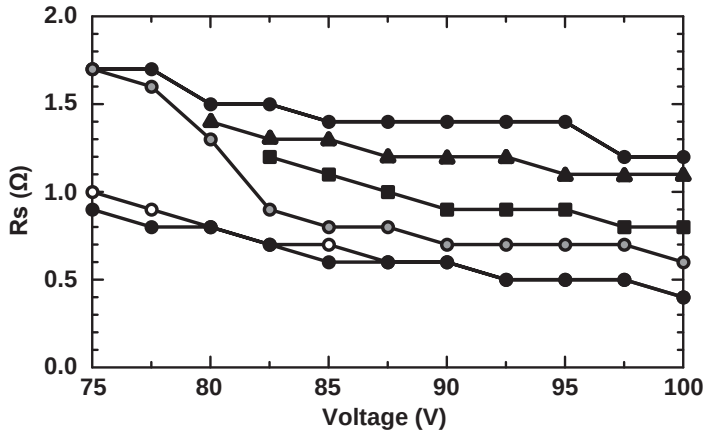

Figure 3.9: Measured switch resistance versus actuation voltage for several switches (resistance measured using a 4-wire setup).

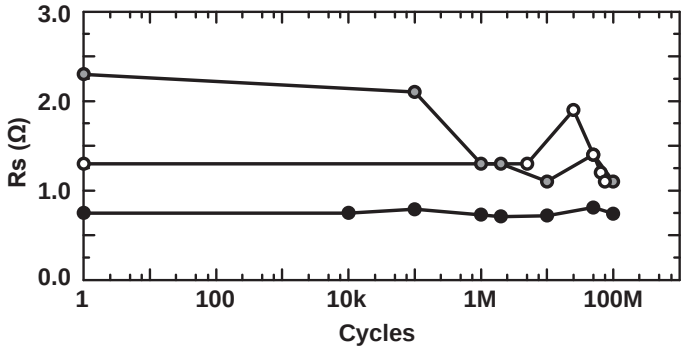

Figure 3.10: Reliability of several metal contact switches under 2 W of cold-switched RF power and 90 V actuation. The resistance was measured using a 4-wire setup.

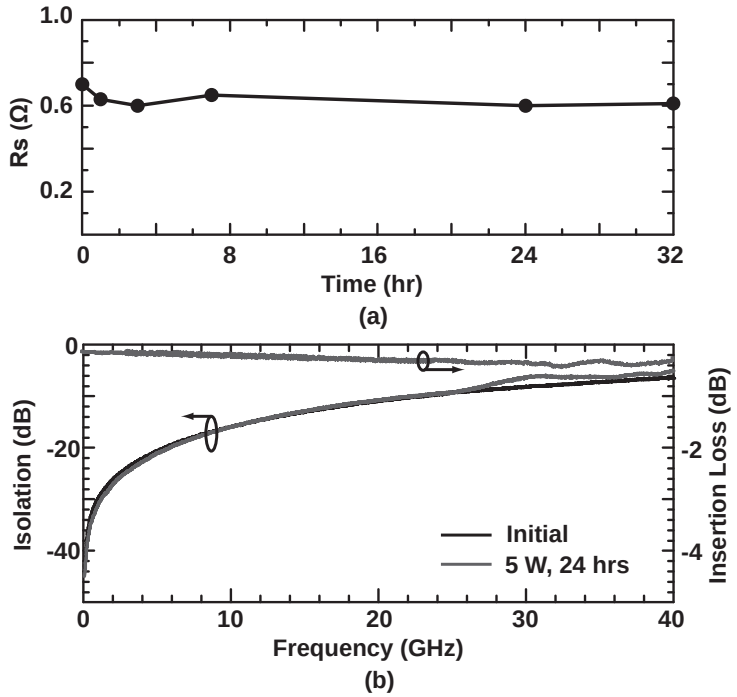

Figure 3.11: Measured power handling of switch - (a) switch resistance versus time under 2 W of continuous RF power and (b) measured S-parameters before and after 24 hours of continuous actuation under 5 W of RF power.

Chapter 4

A Compact Cantilever-Based RF MEMS Switch and Switching Networks

RF-MEMS metal-contact switches occupy a niche between electromagnetic relays and solid-state switches, making them ideally suited for a variety of applications: automated test equipment, satellite systems, defense, and electronic instrumentation among others [1]. For these systems, RF MEMS based switching networks offer lower losses and higher linearity than solid state switches; and they offer better reliability, faster operation, and smaller size than electromagnetic relays. Some examples of RF MEMS metal-contact switches used to implement switching networks are given in [**?**, **?**, 14, 45–47].

In previous work, a mN-force actuator with stress- and temperature insensitivity was achieved with the use of a large-area tethered cantilever (180×235 μm) [48]. In this work, we present the design and measurement of a compact RF MEMS metal-contact switch. Compared to the previous design, this switch has a smaller size, faster operation, and roughly the same restoring force, but with a lower contact force. Also, the restoring force is greater relative to the contact force compared to previous work ($\sim$1:1 vs $\sim$1:2) - which reduces contact adhesion and improves reliability [1]. The switch is designed to be insensitive to stress-effects and temperature, and is fabricated using a simple surface micromachining process. Furthermore, due to its size, miniature series/shunt, SP4T, and

SP6T switching networks are demonstrated using this switch.

4.1 Switch Design

The metal-contact RF MEMS switch is based on a tethered cantilever topology with orthogonal anchors and an 8-μm thick gold cantilever [48]. The top view and cross section are shown in Fig. 4.1. The switch is 120$\times$160 μm^2 and contact is made with a pair of 0.3 μm thick dimples. The cantilever is stable until the actuation voltage (across the pull-down electrode and the cantilever) is $>$ 110 V, so no stopper dimples or dielectrics are used to protect the beam from the electrode.

The simulated pull-in voltage is 74 V and the simulated release voltage is 70 V. The actuation and release stiffnesses, k_a and k_r, are 1060 and 830 N/m, respectively. The simulated contact force varies from 0.38-0.72 mN for actuation voltages of 90-100 V, and the release force is 0.46 mN (Fig. 4.2). The use of tethers and orthogonal anchors results in a design which is very insensitive to stress effects and temperature [**?**]. For a temperature change of ΔT=100°C and a biaxial stress of σ=$\pm$100 MPa, the contact is simulated to deflect by only -18 nm and +25 nm, respectively. Similarly, for a stress gradient of $\nabla\sigma$=$\pm$4 MPa/μm, the simulated contact deflection is $\pm$8 nm. This results in a nearly constant restoring force. For biaxial stress and temperature variations, the maximum deflection is at the contact, so the contact force is also nearly constant. However, for stress gradients, the maximum deflection is in the center of the beam (simulated to be $\mp$89 nm for $\nabla\sigma$=$\pm$4 MPa/μm) - and this affects the contact force (Fig. 4.2).

Modal analysis results in a mechanical resonance mode at 205 kHz and the mechanical Q is estimated to be 1.8. The switching time is simulated to be 2.4-2.1 μs for actuation voltages of 90-100 V, respectively. The simulated up-state capacitance is 16 fF.

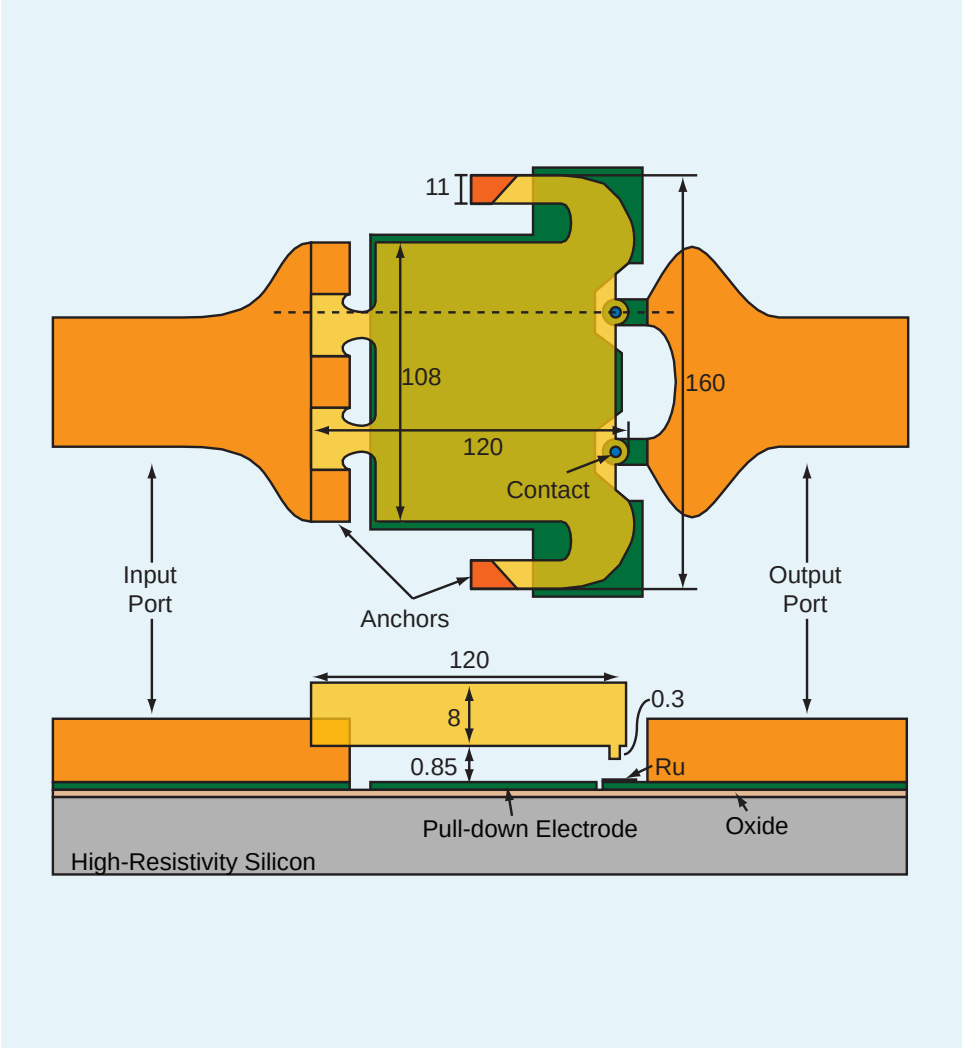

Figure 4.1: Top view and cross section of the RF MEMS metal-contact switch. All dimensions are in μm.

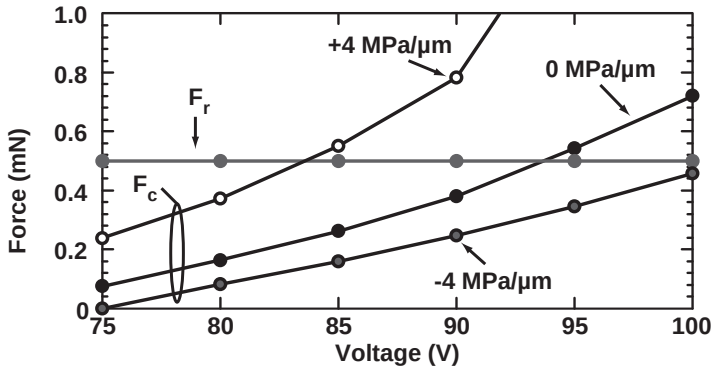

Figure 4.2: Simulated (total) contact and release force, F_c and F_r, versus actuation voltage.

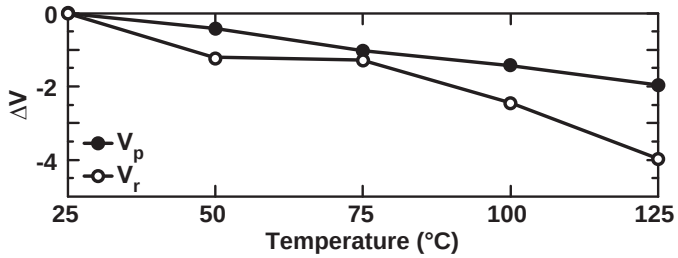

Figure 4.3: Measured average change in pull-in and release voltage versus temperature. The switches showed negligible hysteresis with temperature.

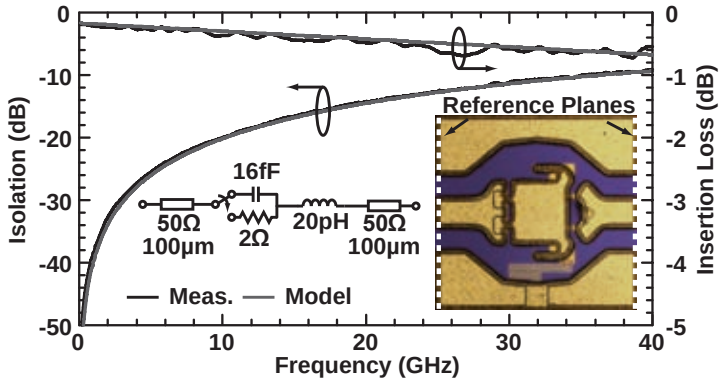

Figure 4.4: Measured and modeled S-parameters of the RF MEMS metal-contact switch. The actuation voltage is 90 V (F_c=380 μN).

4.2 Fabrication and SPST Measurements

The switches were fabricated using the UCSD metal-contact switch process [37]. All measurements were performed on unpackaged switches in a standard laboratory environment with flowing N2. The pull-in and release voltages were measured to be 75-80 V and 70-75 V, respectively, over several devices. Fig. 4.3 presents the measured drift in pull-in and release voltage versus temperature (averaged over 4 devices). The pull-in voltage drops by 2 V over ΔT=100°C, resulting in a slope of -20 mV/^{o}C. For actuation voltages of 90-100 V, the switching time was measured to be 3.2-2.8 μs (first bounce), respectively, and the release time was measured to be 1.4 μs.

Fig. 4.4 presents the measured and modeled S-parameters from 0.1 to 40 GHz. The equivalent up-state capacitance, C_u is 16 fF, while the down-state resistance and inductance are 1-2 Ω and 20 pH, respectively - in good agreement with simulation. The switch was tested to 5 W continuous (over several minutes) and cycling tests showed a reliability $>$10M cycles under cold-switching conditions with 1 W of incident RF power. Extended reliability tests were not performed.

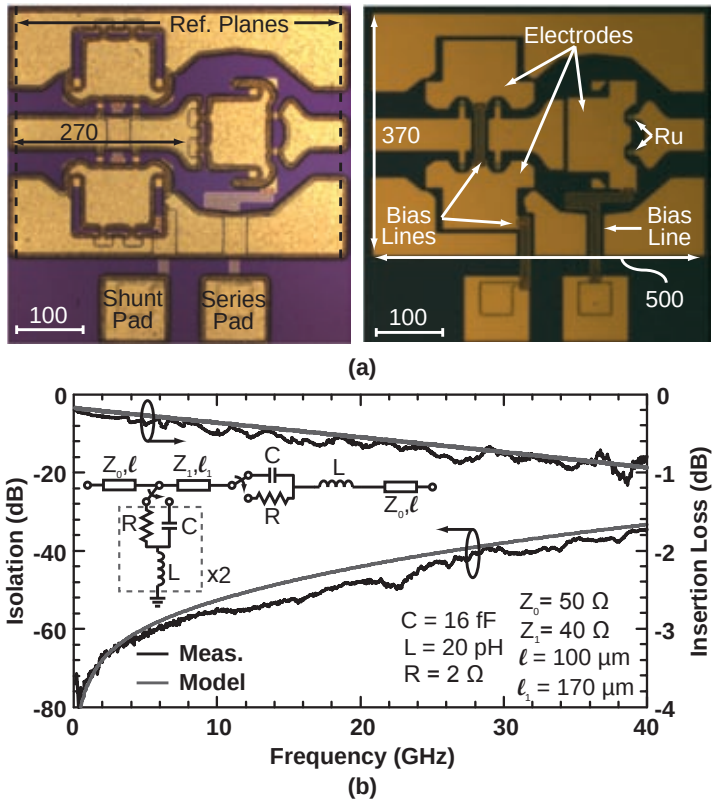

Figure 4.5: (a) Microphotograph of the RF MEMS metal-contact switch and bottom metallization in series/shunt configuration, and (b) measured and modeled S-parameters. All dimensions are in μm.

4.3 Switching Networks

4.3.1 Series/Shunt Design and Measurement

A microphotograph of the switch in a series/shunt configuration is shown in Fig. 4.5a. The design is implemented with one series and two shunt switches to maintain symmetry, maximize isolation, and minimize losses. Since the up-state capacitance is low, the additional capacitance from the extra shunt switch does not contribute to the insertion loss. However, the additional shunt path to ground significantly improves the isolation. The measured and modeled S-parameters are shown in Fig. 4.5b and are in good agreement. The series/shunt device achieves an insertion loss < 1 dB (equivalent to 2 Ω at DC) and an isolation $>$30 dB at 40 GHz.

4.3.2 SP4T Design and Measurement

Fig. 4.6a presents a microphotograph of the miniature switch in an SP4T configuration. The device is symmetric about port 1. The active area of the SP4T is 560×530 μm^2 (0.3 mm^2); the entire area, including the CPW ground metallization and actuation pads, is 850×650 μm^2. The bias lines are all high-resistivity (∼5 kΩ/□), and are routed under other signal lines using crossovers with negligible effect on the circuit. Since the device is symmetric, the performance of P2 and P3, and P4 and P5 are identical.

The measured S-parameters are shown in Fig. 4.6b from 0.1-6 GHz. The device is well matched, with S_{11} <-30 dB up to 6 GHz (S_{nn} is nearly identical when the n-th port is actuated). The equivalent DC resistance is 0.6-1.4 Ω (insertion loss <0.2 dB to 3 GHz), with the variation caused by contact contamination (the switches are unpackaged). The SP4T provides >30 dB isolation at 3 GHz. Only two probes were used in the S-parameter measurement, with the other ports left unterminated. The isolation improves by 6 dB at 6 GHz with all ports terminated with 50 Ω, if one of the ports is actuated.

4.3.3 SP6T Design and Measurement

A microphotograph of the tethered metal-contact switch in an SP6T configuration is shown in Fig. 4.7a. The active area of the switch is 560×730 μm^2 (0.41 mm^2); the entire area of the switch is 850×855 μm^2. Due to symmetry, the port pairs (P2,P3), (P4,P5), and (P6,P7) exhibit identical performance. As with the SP4T, high resistivity bias lines are used and they are all routed together to the top of the circuit to facilitate easy probing and packaging. Fig. 4.7b presents the measured S-parameters of the SP6T. The measured return loss is <-25 dB up to 6 GHz (S_{11} is nearly identical to S_{nn} when the n-th port is actuated). The equivalent DC resistance is 1.3-1.8 Ω, and the measured insertion loss is <0.3 dB from DC to 3 GHz. The measured isolation is >26 dB at 3 GHz. The isolation improves by 6.5 dB at 6 GHz with all ports terminated with 50 Ω, if one of the ports is actuated.

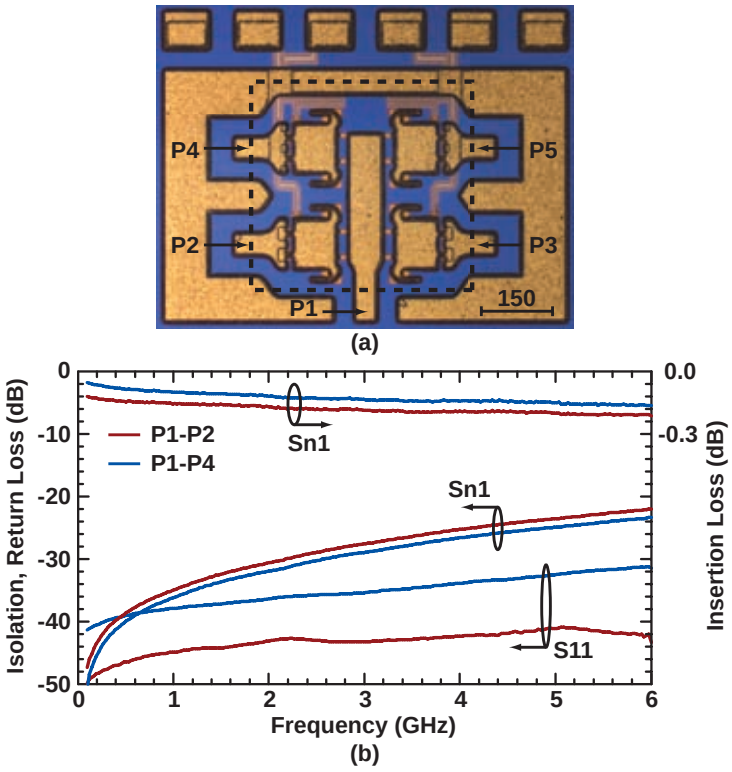

Figure 4.6: (a) Microphotograph of the RF MEMS metal-contact switch in an SP4T configuration, and (b) measured S-parameters of the metal-contact SP4T switching network. All dimensions are in μm. The isolation performance improves by $\sim$6 dB with all ports terminated with 50 Ω.

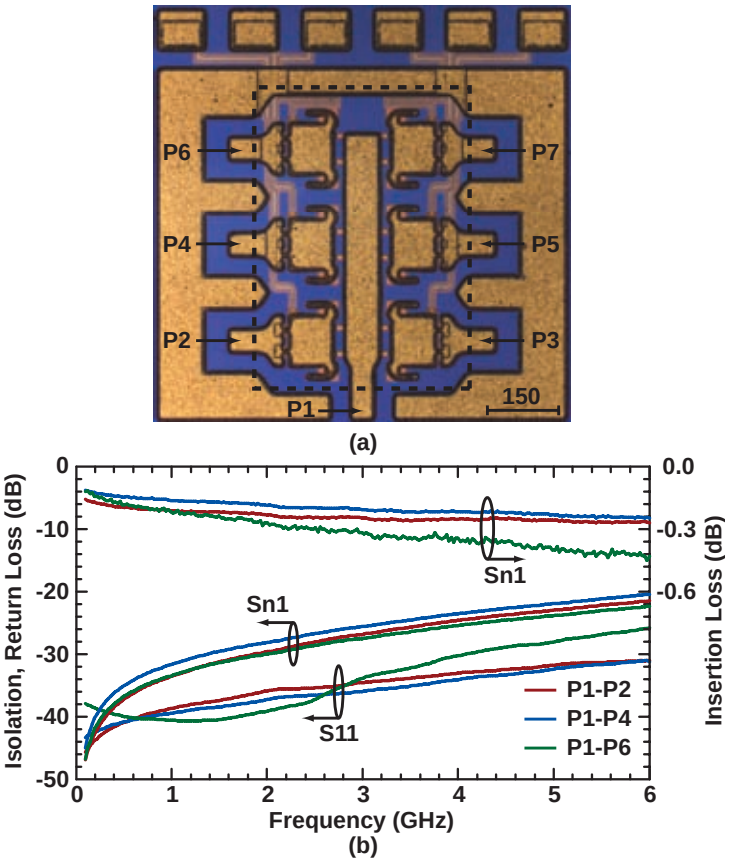

Figure 4.7: (a) Microphotograph of the RF MEMS metal-contact switch in an SP6T configuration, and (b) measured S-parameters of the metal-contact SP6T switching network. All dimensions are in μm. The isolation performance improves by $\sim$6 dB with all ports terminated with 50 Ω.

4.4 Conclusion

This paper has presented the design and measurement of a compact stress- and temperature-insensitive metal-contact RF MEMS switch using a tethered cantilever topology and orthogonal anchors. The switch, implemented with an Au/Ru contact, achieves 1-2 Ω switch resistance and 16 fF of up-state capacitance in a small size. A series/shunt configuration demonstrated >30 dB isolation up to 40 GHz. Furthermore, compact SP4T and SP6T switching networks were implemented and measured using the metal-contact switch, and showed low insertion loss (<0.5 dB) and good isolation (>20dB) from DC to 6 GHz. Due to the fact that the devices are insensitive to stress effects and temperature, the devices readily lend themselves to conventional RF MEMS packaging techniques. Thus, with packaging, this switch is a good candidate for compact, low-loss, and high-linearity switching networks.

This chapter is largely a reprint of material submitted to *IEEE Microwave and Wireless Components Letters*, 2012; C. D. Patel and G. M. Rebeiz. The dissertation author is the primary author of the source material.

Chapter 5

A High-Performance RF MEMS Metal-Contact Switch and Switching Networks

5.1 Introduction

RF MEMS metal-contact switches are an emerging class of relays which are receiving increased attention for defence and industrial applications such as wideband switching matrices, electronic test equipment, medical devices, and satellite systems [1, 13, 15, 34, 49–51]. These devices possess many advantages over conventional electromagnetic relays such as size, power consumption, and, most importantly, reliability.

The performance of a metal-contact RF MEMS switch is primarily determined by the tribology of the contact area. The size of the contact spot and integrity of the contact material determine most of the main parameters of interest - the switch resistance and insertion loss, power handling, and reliability [1, 6]. Increasing the static contact force to mN-levels results in a larger contact spot size and improves the performance of the switch in all of these areas. However, increasing the transient impact force of the switch (and thus, the impact energy) reduces the integrity of the contact material and can adversely affect the switch performance. Furthermore, the increase in adhesion between the metal contacts due to the mN-level contact force requires a mN-level restoring force

to break the contact. The resulting devices have large lateral dimensions compared to the electrode gap ($>100\times$) [35, 37], rendering them susceptible to out-of-plane deflections due to stress effects and temperature. A well-designed device must balance all of these requirements satisfactorily. There are several examples of low and high contact force designs in literature [17, 18, 26, 28, 48, 52], as well as two which are commercially available [36, 47].

In this chapter, we present the design, analysis, fabrication, and measurement of an RF MEMS metal contact switch with high reliability, linearity, and power handing capable of DC-40 GHz operation [49]. The device, which is fabricated using an all-metal surface micromachining process, is stable versus stress effects and temperature, and exhibits robust performance under prolonged operation. High-performance switching networks are also demonstrated.

5.2 Design and Analysis

5.2.1 Device Design and Operation

The design of the metal contact switch is based on an inverted crab topology - a 10-μm -thick gold plate (E = 35 GPa, ν = 0.44) supported by four curved springs (Fig. 5.1). The plate is 150x150 μm^2, while the entire switch occupies an area of $\sim$250x250 μm^2. The actuator is electrostatically driven. The pull-down electrode occupies the entire area underneath the plate including the springs, so as to maximize the actuation force. No dielectric layer is used to separate the plate from the pull-down electrode. Instead, stopper dimples are employed to prevent the plate and pull-down electrode from touching.

The topology was chosen due to the fact that mass-spring designs tend to exhibit less sensitivity to temperature and biaxial stress than fixed-fixed designs, and less sensitivity to stress gradients than free cantilever designs. In this work, the springs are short and very stiff in order to provide the necessary release force. This allows them to be folded inward towards each other to minimize area and to further minimize sensitivity to biaxial stress and temperature (since the springs do not oppose each other or the plate).

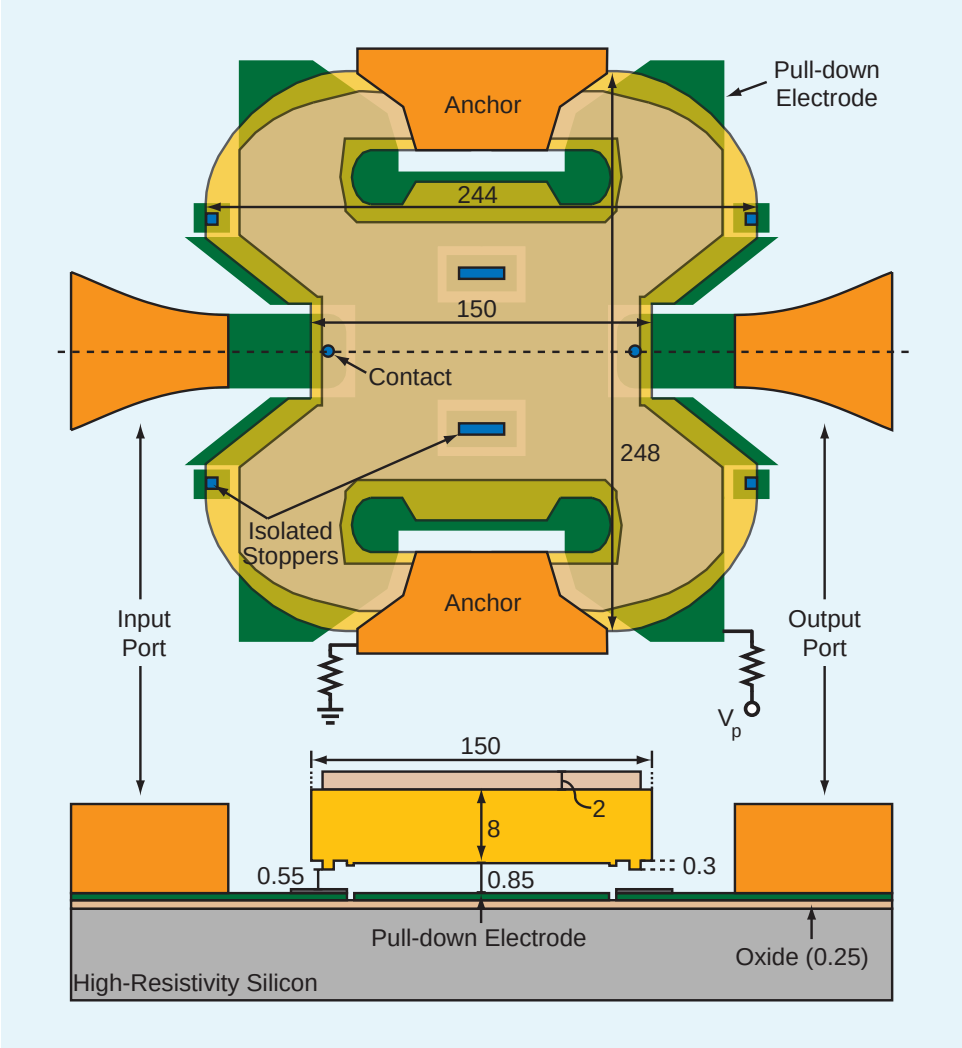

Figure 5.1: Top view and cross section of the metal-contact switch (z-axis not to scale). All dimensions are in μm.

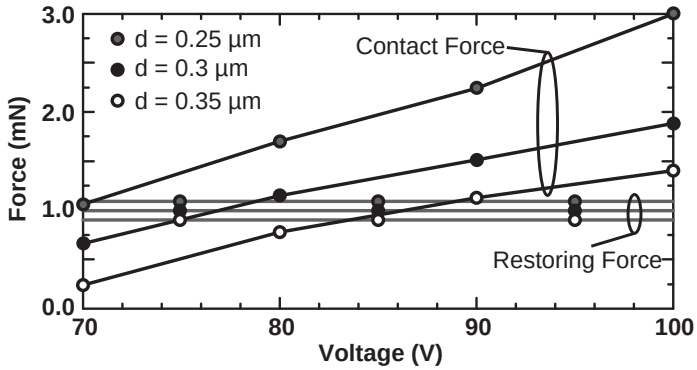

Figure 5.2: Simulated contact and restoring force per contact versus actuation voltage for dimple height, d = 0.25 - 0.35 μm.

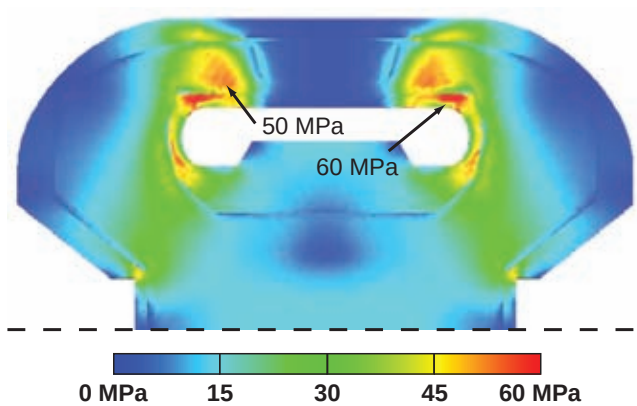

Figure 5.3: Von Mises stress induced at anchors due to a contact force of 1.5 mN (90 V actuation voltage).

The contact metallurgy was chosen to be layered Ru on Au for the bottom contact and pure Au for the top contact. This was chosen to maintain a low contact resistance and high reliability (when clean), while reducing contact adhesion and wear at mN-level contact forces [7].

Finite-element (FEM) simulations [39] show that at least 68 V is required across the plate and pull-down electrode to form a contact. The actuation and release spring constants are simulated to be $k_a = 6020$ N/m and $k_r = 1820$ N/m, respectively. The simulated contact and restoring force versus voltage is shown in Fig. 5.2 for a $\pm$50 nm variation of the dimple height, d (0.3 μm nominal). At actuation voltages of 80-90 V, the contact force is 1.2-1.5 mN per contact and the restoring force is simulated to be 1.0 mN per contact. For d = 0.25-0.35 μm and 90 V actuation, the contact force varies from 1.1-2.2 mN per contact and the restoring force varies from 0.9-1.1 mN. A dimple height of d = 0.3 μm was chosen to balance the contact force and switch robustness.

Nominally, the RF contact will be formed before the isolated stopper dimples touch their landing pads - however, it will be shown in Section 5.2.2 that for some stress conditions the stoppers do touch the isolated landing pads before RF contact is formed. In this case, the restoring force is increased with only a slight decrease in contact force due to a corresponding increase in actuation force from the profile of the bending of the plate. Simulations also show that the device does not fail until the actuation voltage is larger than 120 V. Furthermore, uneven heights of $\pm$50 nm in the stopper dimples and contact dimples at the two RF ports can be tolerated with the worst-case contact having a contact force of 1.0 mN for an actuation voltage of 90 V.

The anchor design has a significant effect on the induced stress on the beam during actuation. This, in turn, affects the reliability of the device under prolonged actuation conditions since material properties will drift over time under excessive levels of stress due to viscoelasticity and creep [53, 54]. The curvature of the anchor was designed (using numerical FEM techniques) to minimize the induced stress during device operation. Fig. 5.3 shows the simulated Von Mises stress for an actuation voltage of 90 V (1.5 mN of contact force). The maximum stress is 60 MPa located a short distance away from the anchor, where the springs undergo torsion as well as bending effects.

5.2.2 Stress and Temperature Effects

Stress gradients, residual biaxial stresses, and temperature can significantly affect the performance of RF MEMS switches - particularly at dimensions greater than 100 μm [37]. The deflection of the contact due to a stress gradient of $\nabla\sigma_z$ = $\pm$4 MPa/μm is $\mp$20 nm [49]. In addition, the center of the switch deflects $\mp$150 nm and the tip of the switch deflects $\pm$230 nm. Fig. 5.4 presents the simulated pull-in and release voltage versus stress gradient. The pull-in voltage varies from 64-80 V and the release voltage varies from 55-74 V over a range of $\nabla\sigma_z$ = $\pm$4 MPa/μm, with a nominal pull-in voltage of 68 V and a nominal release voltage of 60 V. Note that the release voltage simulations were performed assuming no adhesion force on the contacts. Fig. 5.5 presents the FEM simulated contact and restoring force versus stress gradient for actuation voltages from 80-100 V. For $\nabla\sigma_z < 0$, the stopper dimples at the peak edge touch the landing pads before the RF contact is formed. As seen in the figure, this increases the restoring force and slightly reduces the contact force. For $\nabla\sigma_z > 0$, the stopper dimples at the plate center touch the landing pads before the RF contact is formed and therefore absorb more of the contact force - however, the restoring force is not increased since the stoppers still lift-off first when the device is released. For any stress gradient in the range $\nabla\sigma_z$ = $\pm$4 MPa/μm, the minimum contact and restoring force is $\sim$1 mN for an actuation voltage of 90 V.

Fig. 5.6 presents the contact and restoring force per contact versus the dimple height, d, for $\nabla\sigma_z$ = $\pm$2 MPa/μm for 90 V actuation. A dimple height of d = 0.3 μm provides the least variation in performance versus stress gradient. Still, the switch is robust for all stress gradients between $\pm$2 MPa/μm for d = 0.25-0.35 μm. For $\nabla\sigma_z > 0$, there is very little variation in restoring force, however there is a jump in restoring force for $\nabla\sigma_z < 0$, due to the stoppers at the peak edge landing before the RF contacts.

The device exhibits virtually no deflection versus residual biaxial stress and temperature due to the choice of topology and anchor design. For a residual biaxial stress, σ_0, of 200 MPa, the contact deflects -43 nm; for a temperature increase, ΔT, of 100 ^oC, the contact deflects +26 nm [49]. Table 5.1 presents a comparison between anchors designed with and without curvature. In addition to reducing the induced Von Mises stress upon actuation, the curved anchors improve the deflection of the contact due to

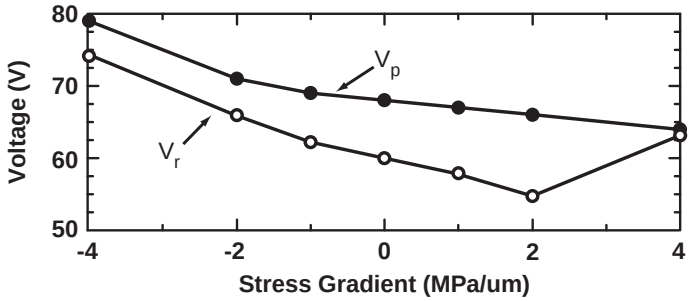

Figure 5.4: Pull-in and release voltage versus stress gradient.

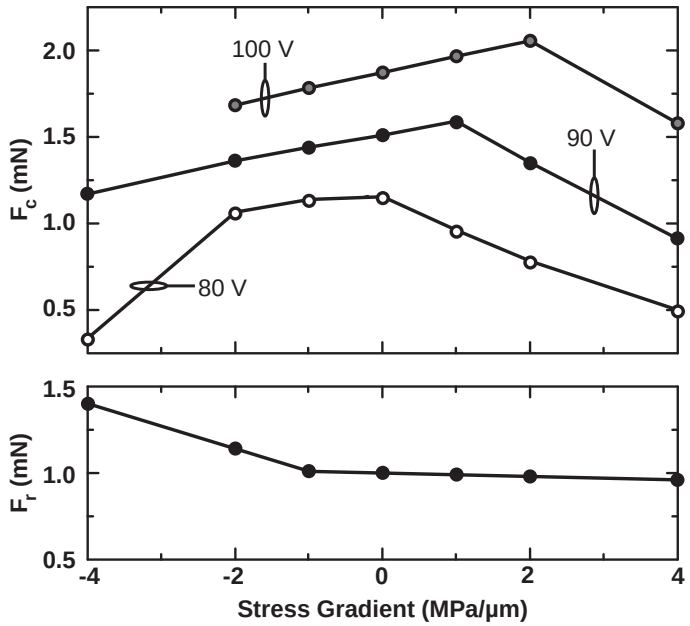

Figure 5.5: Simulated contact and restoring force per contact versus stress gradient.

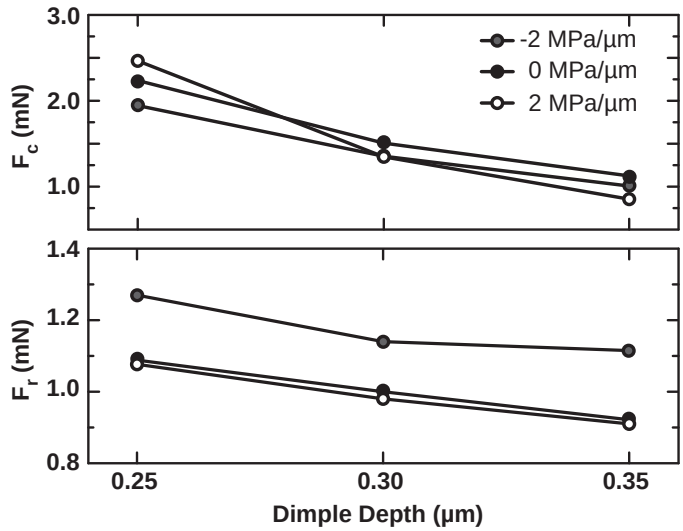

Figure 5.6: Simulated contact and restoring force per contact versus dimple dimension for various stress gradients (90 V actuation).

stress and temperature effects. Fig. 5.7 presents the simulated contact and restoring force versus biaxial stress. For a biaxial stress of $\pm$200 MPa, the contact force changes by $\sim$250 μN (90 V actuation). The restoring force changes by less than 100 μN.

Fig. 5.8 shows the contact and restoring force per contact versus dimple height for σ_0 = $\pm$100 MPa (90 V actuation). Regardless of the dimple height, the contact and restoring force does not vary considerably due to biaxial stress.

Fig. 5.9 shows the simulated contact and restoring force versus temperature. For a 100 ^oC temperature change, the contact force changes by only 0.1 mN (90 V actuation)

Table 5.1: Effect of Anchor Design on Switch Performance

Contact Force (mN)	1.5	1.5
Restoring Force (mN)	1.0	1.0
Deflection, ΔT=100 ^{o}C (nm)	26	-73
Deflection, σ_0=200 MPa (nm)	-43	147
Deflection, $\nabla\sigma_z$=4 MPa/μm (nm)	-20	-33

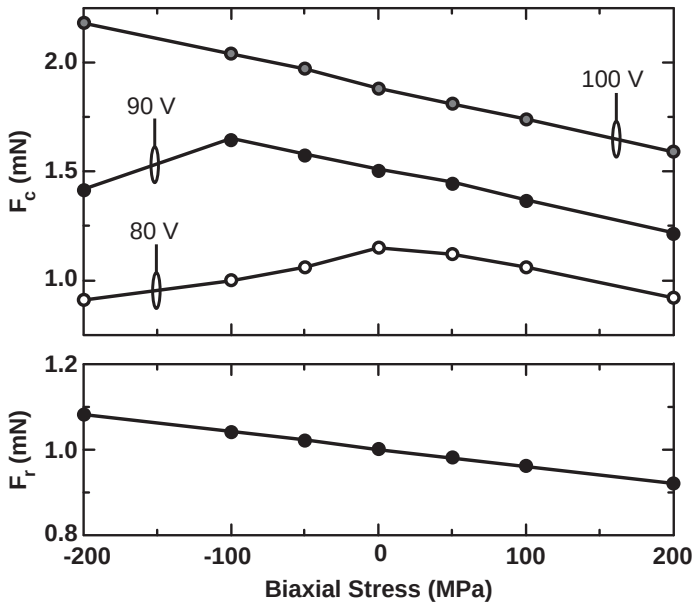

Figure 5.7: Simulated contact and restoring force per contact versus biaxial stress.

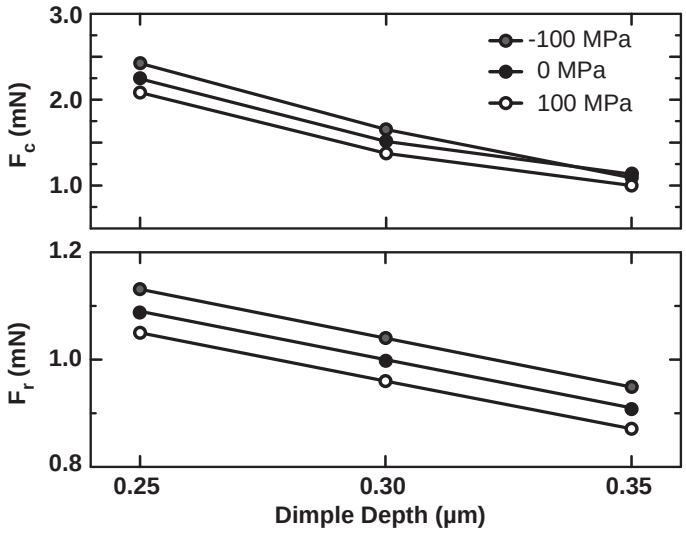

Figure 5.8: Simulated contact and restoring force per contact versus dimple dimension for various biaxial stresses (90 V actuation).

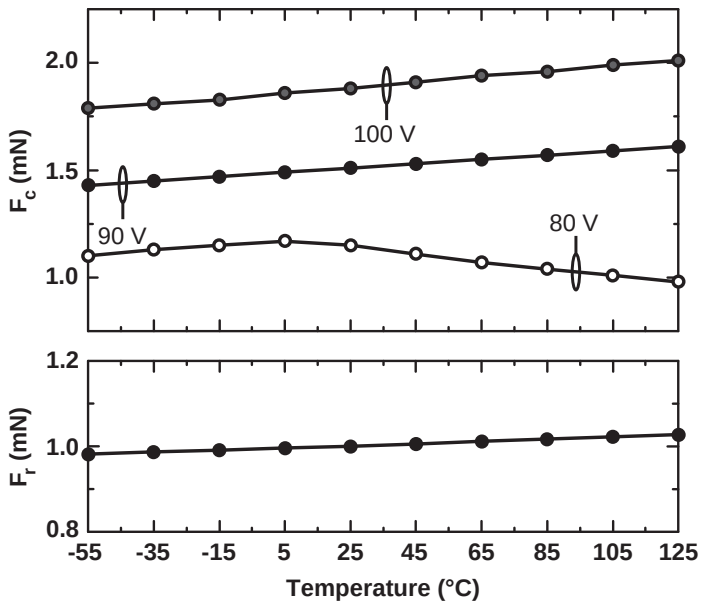

Figure 5.9: Simulated contact and restoring force per contact versus temperature. The coefficient of thermal expansion of the substrate is assumed to be zero for worst case behavior.

and the restoring force changes by only 50 μN. Over this range, the simulated pull-in voltage changes by only 1 V. For temperatures greater than 25°C, no portion of the actuator has a negative deflection (the entire actuator deflects away from the actuation electrode and RF contacts). This makes the switch ideal for conventional hermetic packaging techniques for RF MEMS - since these processes can expose the released MEMS structure to temperatures as high as 500°C and there is no risk of contact between the MEMS plate and the actuation electrode of RF contact.

5.2.3 RF Power Handling Analysis

For metal-contact RF MEMS switches, the RF power handling is typically limited by a localized temperature rise in the contact spot. The increase in temperature is caused by joule heating due to the contact resistance. The contact resistance can be expressed sufficiently accurately as [6],

$$R_c = \frac{\rho}{2a} + R_r \tag{5.1}$$

$$a = \sqrt{\frac{F_c}{\pi H}} \tag{5.2}$$

where ρ is the resistivity of the contact material, R_r is an additional resistance due to resistive contamination, a is the radius of the contact spot, H is the Meyer indentation hardness of the contact material (10.1 GPa for Ru, 1.6 GPa for Au [55, 56]), and F_c is the total contact force per contact. It is assumed that the thickness of any resistive films is sufficiently thin so as not to significantly affect the size of the contact spot. Additional resistances such as Maxwell spreading resistance and Sharvin resistance do not qualitatively affect the analysis [56]. The presented switch employs a hybrid contact consisting of gold for the top contact and a thin film of ruthenium (100 nm) on top of gold on the bottom contact. For a conservative analysis, the contacts are assumed to be pure ruthenium for hardness and resistance in the calculations. For clean metal contacts, the temperature of the contact is given by [6],

$$T_m = \sqrt{\frac{V_c^2}{4L} + T_o^2} \tag{5.3}$$

where V_c is the voltage across the contact, T_0 is the ambient temperature, and L is the Lorenz number (L=2.44$\times$10^{-8} (V/K)^2). An expression relating the temperature rise to

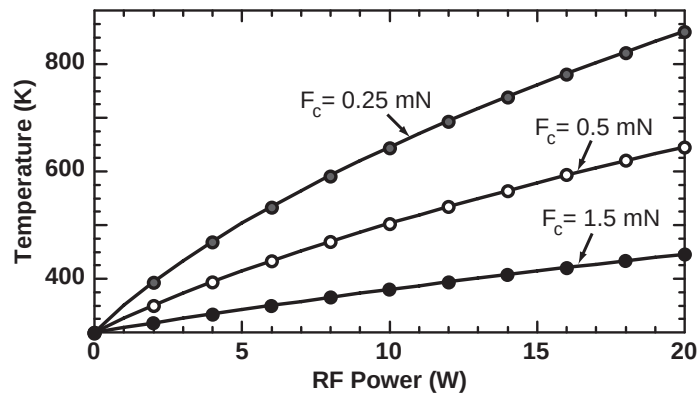

Figure 5.10: Contact temperature versus RF power for clean metal contacts (Ru) with various contact forces.

the incident RF power can be derived by combining (5.3) with microwave circuit theory resulting in (for $R_c << Z_o$),

$$P_{inc} = I^2 Z_0, \quad V_c = IR_c \tag{5.4}$$

$$T_m = \sqrt{\frac{R_c^2}{4L}\frac{P_{inc}}{Z_o} + T_o^2} \tag{5.5}$$

where P_{inc} is the incident RF power, I is the RMS value of the RF current, and Z_o is the transmission line impedance (50 Ω). Fig. 5.10 presents the contact temperature calculated using (5.1)-(5.5) versus RF power for several different contact forces. For a contact force of 1.5 mN and RF powers up to 10 W, the contact temperature remains below 400 K, the softening point of gold (gold is placed under the Ru contact).

The expressions given by (5.3) and (5.5) are only valid for clean metal contacts because they rely on the assumption that the electric and thermal currents follow the same paths [6]. The presence of a resistive film breaks this assumption and a solution may be obtained by assuming the joule heat is fully liberated at the contact interface. The peak contact temperature for a circular contact area, generating heat uniformly over the contact interface is given by [57],

$$T_m = \frac{q_c a}{2K} + T_0 \tag{5.6}$$

$$q_c = \frac{I^2 R_c}{\pi a^2} = \frac{R_c}{\pi a^2}\frac{P_o}{Z_o} \tag{5.7}$$

where q_c (W/m^2) is the heat generation in the contact and K is the thermal conductivity of the contacts - which in this case is taken to be the thermal conductivity of gold (318 W/(m·K)) since the ruthenium is very thin and does not contribute significantly to the overall thermal resistance. The equation assumes the heat is dissipated evenly between the top and bottom contact which are approximated as semi-infinite surfaces. For this analysis, ρ and K are assumed to be independent of temperature. Fig. 5.11 presents the contact temperature versus RF power calculated using (5.6) and simulated with an FEM solver for several contact forces, assuming a contact resistance of 0.5 Ω in each case, and assuming a silicon substrate. For the presented switch, at a contact force of 1.5 mN and a contact resistance of 0.5 Ω due to a resistive film (1 Ω total), the switch could handle ∼4-5 W, at which point the softening temperature of gold would be reached.

A condition for stiction of metal contacts is that the softening temperature of the hardest contact material must be reached [6], which in this case is Ru (with a softening temperature of 700 K [55]). The contact temperature is below 700 K for up to 14-15 W of RF power for a contact resistance of 0.5 Ω. Repeating the exercise assuming pure gold contacts reveals that. Fig. 5.12 shows the resulting simulated temperature distribution for a 1.5 mN contact under 10 W of RF power for a contact resistance of 0.5 Ω/contact due to a resistive film. The simulation shows that the temperature increase is highly localized at the contact and also that the 0.25 μm thermal oxide significantly inhibits the dissipation of the contact heat. The temperature rise in the gold MEMS plate is 60-70 K, while the temperature rise in the substrate, just under the contact, is only 15 K.

The thermal time constant of the contact area can be estimated by [1],

$$\tau = \frac{\rho_c C_p a^2}{K} \tag{5.8}$$

where ρ_c and C_p are the density and the specific heat capacity of the contact material, respectively. From (5.8), the localized temperature increase happens on the order of nanoseconds. This is due to the small thermal mass of the contact.

Fig. 5.13 presents the simulated contact temperature for 10 W of RF power and for contact resistances of 0.25-1 Ω per contact versus the thermal conductivity of the substrate. The contact temperatures are significantly higher for switches on quartz substrates, but are very similar for GaAs, Si, and AlN substrates. Fig. 5.14 presents the simulated contact temperature versus the thickness of the thermal oxide that separates

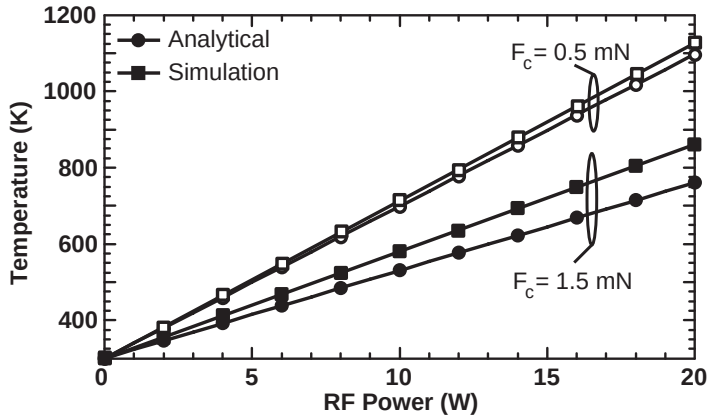

Figure 5.11: Contact temperature versus RF power for metal contacts contaminated with a resistive film resulting in a contact resistance of R_c = 0.5 Ω/contact. For R_c = 1 Ω/contact, the temperature increase above T_0 is doubled per (5.7).

the MEMS device from the substrate. The simulations are performed assuming a silicon substrate and 10 W of RF power with R_c = 0.5 Ω per contact. There is an increase of about 50 K in the contact temperature (∼20% increase) when comparing a device fabricated with no separating oxide and a separating oxide of 350 nm.

5.2.4 Contact Dynamics

The dynamic behavior of the switch is useful for determining the switching characteristics of the device. The mechanical response of the switch with area, A, and initial gap, g_0, due to an applied voltage, $V(t)$, and modeled as a single-degree-of-freedom system is given by [1],

$$m_e \frac{d^2 z}{dt^2} + b(z)\frac{dz}{dt} + kz = -\frac{1}{2}\frac{\epsilon_0 A V(t)^2}{(g_0 - z)^2} \tag{5.9}$$

$$b(z) = \frac{3}{2\pi}\frac{\mu A^2}{(g_0 - z)^3} \tag{5.10}$$

where k is the spring constant under actuation conditions (6000 N/m) and m_e is the effective switching mass (6.25 μg), determined using the principle of equivalence of kinetic energy [58]. The damping, $b(z)$, as a function of beam deflection is given by (5.10), where μ is the viscosity of air (μ = 1.076×10^{-5} Pa·s). Fig. 5.15 presents the contact position ($g_0 - z$) and velocity versus time calculated using (5.9)-(5.10) due to an

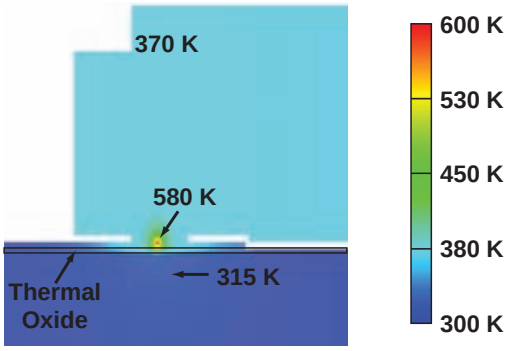

Figure 5.12: Temperature distribution due to 10 W of RF power passing through the switch with a contact resistance of 0.5 Ω/contact and 1.5 mN of contact force. The oxide is 0.25 μm thick.

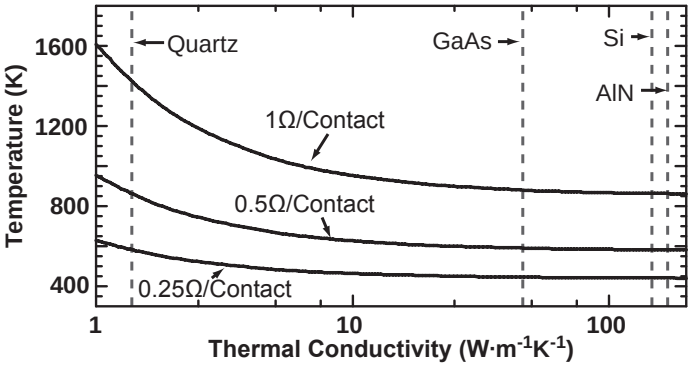

Figure 5.13: Contact temperature versus the thermal conductivity of the substrate for 10 W of RF power and 1.5 mN of contact force. Assumes 0.25 μm of separating oxide.

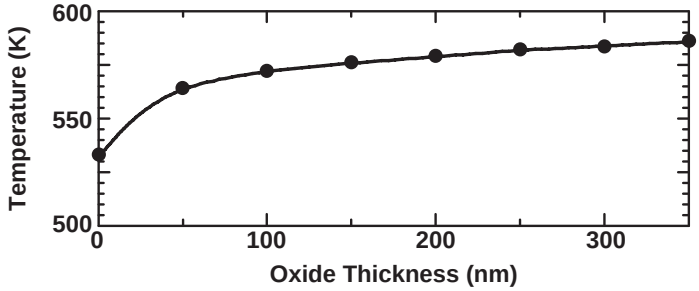

Figure 5.14: Contact temperature versus the separating oxide thickness (on a silicon substrate) for 10 W of RF power, a contact resistance of 0.5 Ω per contact, and 1.5 mN of contact force.

applied actuation step with a rise time of 1 ns (much faster than the actuator dynamics). The switch makes contact when the contact position is 0.3 μm, which is equivalent to the height of the contact dimple (d). For actuation voltages of 80, 90, and 100 V, the switching time is calculated to be 13.2, 7.7, and 5.5 μs.

While the contact force can be increased by reducing the contact and stopper dimple dimensions, it can be seen that the switch velocity greatly increases when the contact position is <0.3 μm, leading to increased contact bounce which can affect the switch reliability [59]. The contact bounce characteristics were calculated (to a first order) by solving (5.9) with the initial conditions $dz/dt = -cv_i$ and $z = g_0 - d$ at time $t = 0$, where v_i is the impact velocity. The rebound coefficient, c, is 1 for the worst-case behavior of a purely elastic contact. Furthermore, for the bounce analysis, $b(z) = 0$ when $dz/dt < 0$, and (5.10) was used otherwise. Fig. 5.16 presents the calculated rebound versus time for contact dimple dimensions of d = 0.25 and 0.30 μm, and a purely elastic contacts. Due to the low velocity at impact with d = 0.3 μm, there is very little rebound. However, with d = 0.25 μm, the rebound is significantly higher due to the sudden increase in impact velocity. After the first bounce, subsequent bouncing is minimal due to the reduced contact velocity arising from the increase in damping. Any plastic deformation at the contact will reduce the rebound coefficient and, thus, the rebound height [6], but this is not considered here. Furthermore, this analysis only considers the effect of the impact characteristics on the contact bounce behavior - a thorough analysis can be found in [59].

The impact force is another transient factor which is of concern in the switch reliability due to the induced hardening and dislocations in the crystalline structure of the metal contact [1, 6]. The impact force is given by,

$$F_i = m_e \frac{v_i}{t_i} \tag{5.11}$$

where v_i is the impact velocity at the contact, and t_i is the impact time - that is, the time over which the velocity of the contact goes from v_i to 0 m/s. The worst case behavior occurs for the case of a purely elastic contact (when the impact time is the shortest) and

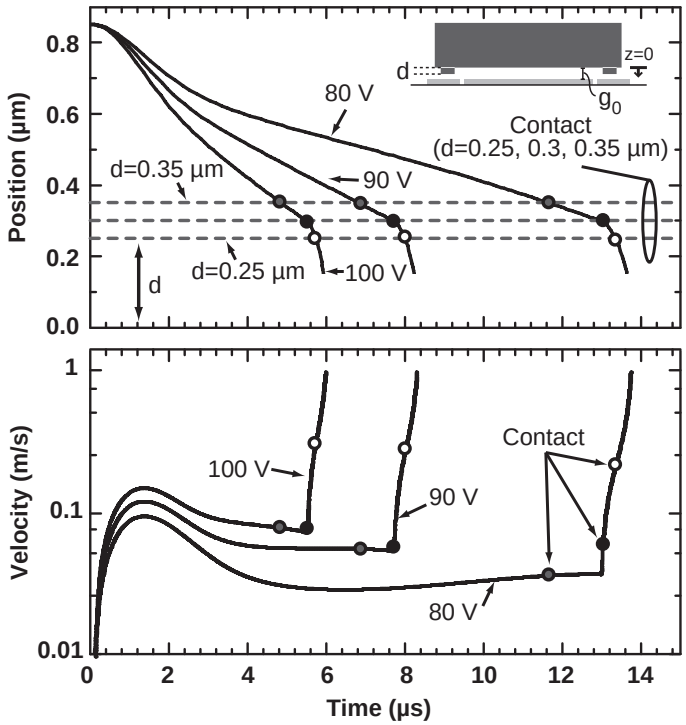

Figure 5.15: Calculated contact position (top) and velocity (bottom) versus time under pull-down conditions for various bias voltages.

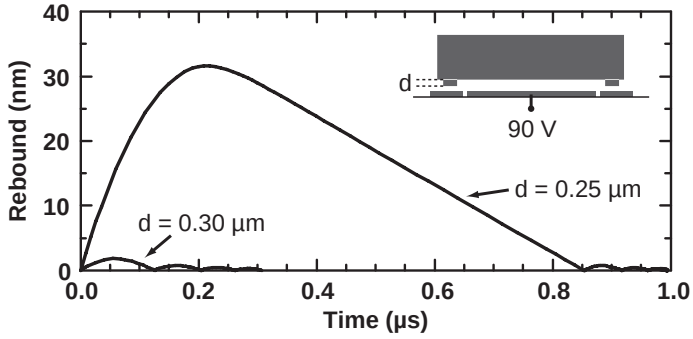

Figure 5.16: Calculated bounce characteristics for 90 V actuation assuming a purely elastic contact and no adhesion (worst-case behavior). Initial contact is at time = 0 μs.

is given by [6],

$$t_i = \frac{3}{2}\left(\frac{m_e^2}{v_i r}\right)^{\frac{1}{5}}\left(\frac{2}{E}\right)^{\frac{2}{5}} \tag{5.12}$$

$$r = \frac{2}{3}\frac{a^3}{F_c}\frac{E}{1-\nu^2} \tag{5.13}$$

where r is the radius of curvature of a sphere which makes a contact spot of radius, a, under a contact force, F_c. E and ν are the Young's modulus and Poisson's ratio of the contact material, respectively. Fig. 5.17 presents the impact force versus applied bias voltage for a switch implemented with pure ruthenium (E=447 GPa, ν=0.3) and pure gold (E=79 GPa, ν=0.44) contacts and assuming a purely elastic contact. The results show that for a contact dimple dimension of d=0.3 μm, the impact force is less than 1 mN. However, for a contact dimple dimension of 0.25 μm, the impact force is 2-4 mN (90 V actuation). Again, this is due to the sudden increase in the velocity of the contact.

The release behavior can be calculated using (5.9) and k = 1800 N/m (release conditions), $V(t) = 0$, and initial conditions $dz/dt = 0$ and $z = 0.55$ μm at $t = 0$. The contact position and capacitance response of the switch versus time is shown in Fig. 5.18 and the release time is estimated to be 3 μs. Modal analysis shows that the first two vibration modes of the switch are at 162 and 183 kHz [49]. The mechanical Q of the modes, given by $Q_n = m_n\omega_n/b_n$, are 1.11 and 1.21 respectively, where m_n, ω_n, and b_n are the effective mass, angular resonant frequency, and damping of the nth mode.

5.2.5 Multi-Contact Power Handling Analysis

Often, metal-contact switches are designed with two or more contacts in parallel. In addition to the effects on the switch mechanics, the use of multiple independent contacts has a significant effect on power handling and contact resistance of the switch. If the total contact force, F, is *spread evenly over* n *independent contacts* (which greatly depends on the switch design), then (5.2) becomes,

$$a = \sqrt{\frac{F}{n\pi H}} \tag{5.14}$$

Referring to (5.1), each contact has a resistance, $R_c \propto \sqrt{n}$, while the entire n-tuple contact resistance, $R_n \propto \sqrt{n}/n$ - resulting a reduced switch resistance. *Assuming the*

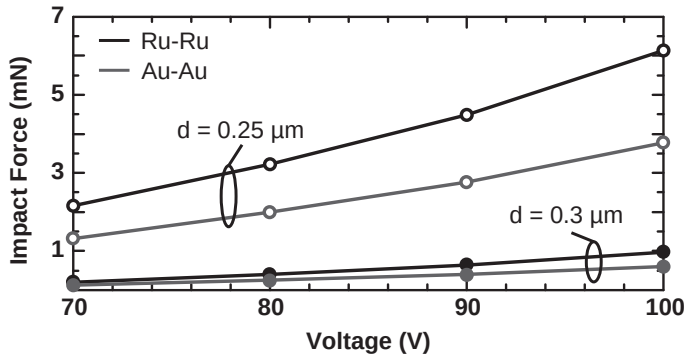

Figure 5.17: Calculated impact force versus actuation voltage assuming a purely elastic contact for Ru-Ru and Au-Au contacts.

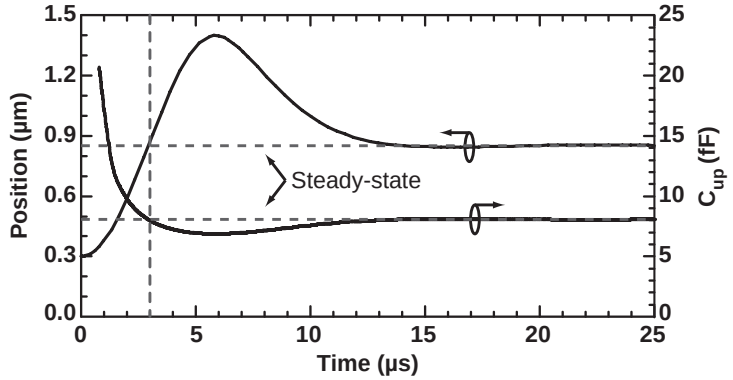

Figure 5.18: Calculated contact position and capacitance versus time under release conditions.

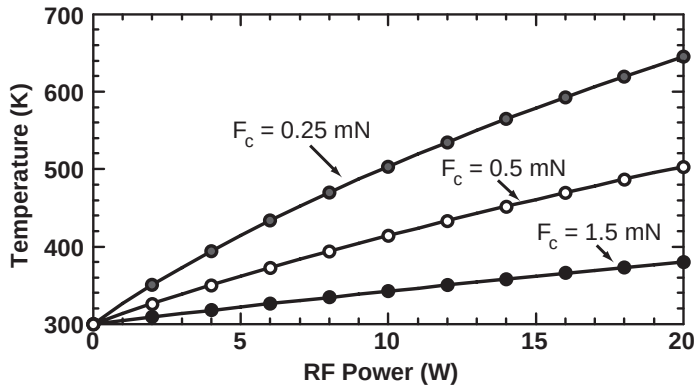

Figure 5.19: Contact temperature versus RF power for clean metal contacts with various contact forces, and current divided evenly into two contacts.

current is evenly split between the n independent contacts, each contact will dissipate less power and generate less heat due to the reduced current per contact. Thus, (5.5) becomes,

$$T_m = \sqrt{\frac{R_c}{n^2 4L}\frac{P_0}{Z_0} + T_0} \tag{5.15}$$

for clean contacts. For contacts contaminated with resistive films, (5.7) becomes,

$$q_c = \frac{R_c}{n^2 \pi a^2}\frac{P_0}{Z_0} \tag{5.16}$$

where R_c is calculated using (5.1). It is important to note that each contact may heat the others if they are physically close to each other, and this will increase the ambient temperature, T_0. For clean metal contacts, $T_m \propto 1/\sqrt{n}$, while for contaminated contacts where the resistance is not primarily determined by the size of the contact spot, $T_m \propto 1/(n\sqrt{n})$. Fig. 5.19 presents the contact temperature vs RF power using (5.15) for an even division of contact force and RF current between two contacts. Fig. 5.20 presents the contact temperature versus RF power, calculating using (5.6) and (5.16), and simulated with FEM for an even division of contact force and RF current between two contacts. The total contact force is 1.5 mN (0.75 mN per contact) and the contact resistance is assumed to be 0.5 Ω per contact (R_s = 0.5 Ω as well for this design).

Compared to the results in Sec. 5.2.3, it is readily apparent that increasing the number of contacts is very effective in reducing the contact temperature even with a lower contact force per contact. However, it is still a challenge to maintain even force and current distribution across many contacts versus process variation and frequency -

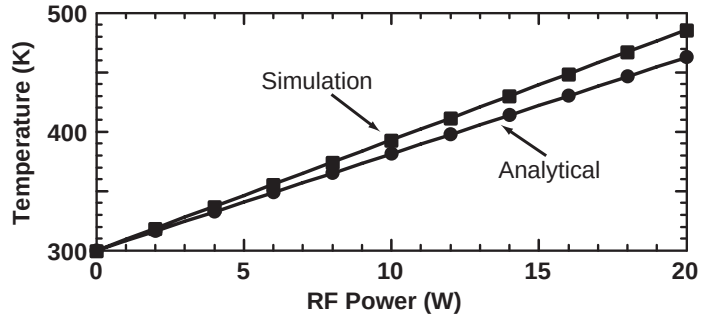

Figure 5.20: Contact temperature versus RF power for metal contacts contaminated with a resistive film resulting in a contact resistance of R_c = 0.5 Ω/contact, with current spit evenly between two contacts.

especially for $n > 2$. For uneven force and current distribution per contact, the benefit of the additional contacts is reduced, but they can still introduce additional points of failure. Therefore, the use of multiple contacts should only be implemented for designs which can mechanically guarantee an equal contact force per contact and electrically guarantee even current splitting per contact.

5.2.6 Electromagnetic Analysis

Fig. 5.21 presents the physical structures comprising the switch from an electromagnetic perspective, and the equivalent circuit model. The lumped-element values are presented in table 5.2 for both high-resistivity silicon and quartz substrates. The elements C_{br} and L_s arise from the transmission line formed by the MEMS actuator, and C_b, R_b, and R_g arise from the actuation electrode and bias network. Since R_b and R_g are large, the bias network has a negligible effect on the RF performance of the switch [1]. The series capacitance between the signal line and the MEMS actuator, C_s, is composed of a parallel plate component, C_{pp}, and a coupled component, C_c. C_{pp} is the parallel plate capacitance formed between the signal feed and the MEMS plate (5 fF). The coupled component (C_c) is the capacitance from the signal feed to the MEMS plate that is coupled through the substrate and C_b, the capacitance between the MEMS plate and the actuation electrode. C_c varies depending on the substrate permittivity. For silicon (ϵ_r = 11.9), C_c is 19 fF. For quartz (ϵ_r = 3.78), C_c is 7 fF.

The devices are implemented in a co-planar waveguide (CPW) configuration (Z_0 = 50 Ω, ℓ = 140 μm). Fig. 5.22 compares the isolation and insertion loss of the switches when implemented on 2500 Ω-cm silicon and quartz substrates and assuming a contact resistance of 0.5 Ω per contact (R_s = 1 Ω) [43]. The equivalent up-state capacitance, C_u, is 8 fF and 3 fF on silicon and quartz, respectively. As expected, the switches exhibit lower insertion loss on quartz as well. Thus, for low power applications, quartz is a superior substrate material.

Table 5.2: Lumped Element Model Parameters

	High-R Silicon	Quartz
R_c (Ω)	1	1
C_s (fF)	24	12
L_s (pH)	22	15
C_b (fF)	400	400
R_b (kΩ)	200	200
R_g (kΩ)	200	200
C_{br} (fF)	17	9
C_u (fF)	8	3

5.3 Fabrication

The metal-contact switch was fabricated on 400 μm thick, 2500 Ω-cm high-resistivity silicon substrate with 2500 $\AA$ thick layer of thermally grown oxide using a variation of the UCSD metal contact switch process [37]. First, a 0.15 μm thick layer of SiCr is deposited and patterned to form the bias resistors. Next, a 0.3 μm thick layer of gold is deposited and patterned to define the actuation electrode, signal feed, and CPW ground planes (Fig. 5.23a). Then, the ruthenium contact (100 nm) is deposited and patterned to define the bottom contact pads (Fig. 5.23b). Silicon Nitride is then deposited patterned to serve as protection for the bias lines. Next, the sacrificial bilayer is deposited and patterned to define the anchors. The sacrificial bilayer is composed of a 0.55 μm thick layer of PMMA underneath a 0.3 μm thick layer of PMGI. The

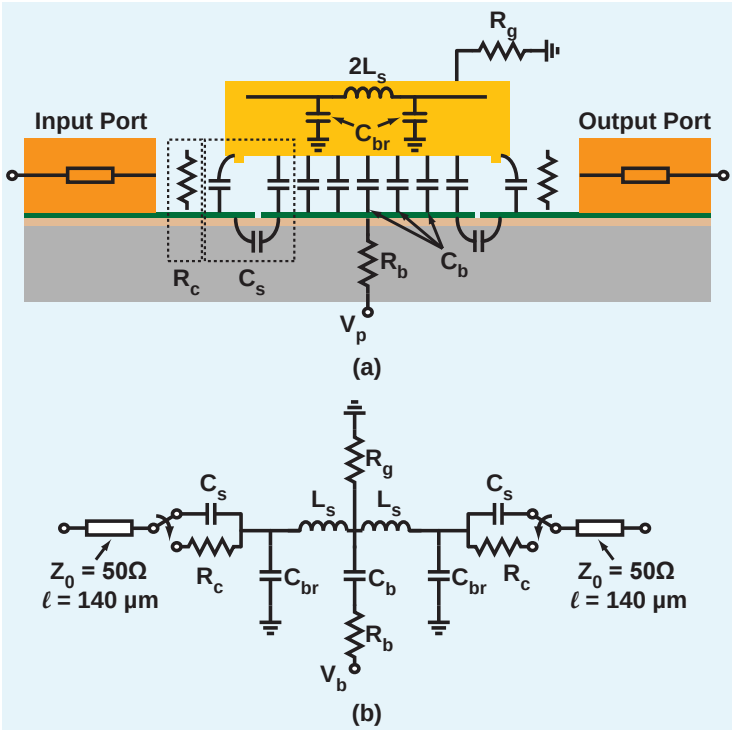

Figure 5.21: (a) Origin of lumped element components and (b) the lumped-element model of the RF MEMS contact switch.

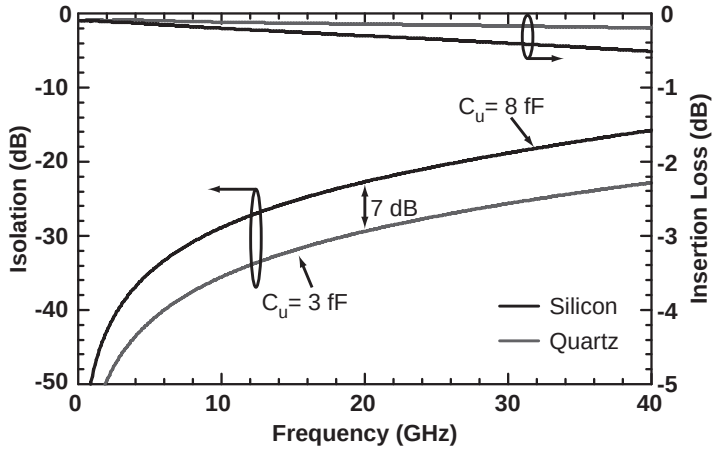

Figure 5.22: Simulated S-parameters on high-resistivity silicon and quartz. Switch resistance, R_s, taken to be 1 Ω total (0.5 Ω/contact).

contact and stopper dimples are then formed in the layer of PMGI (Fig. 5.23c). Next, a gold seed layer is deposited and a 10 μm thick electroplating mold is formed out of photoresist (Fig. 5.23d). The wafer is then electroplated with 8 μm of gold to form the CPW lines and the MEMS actuator. Then, the mold is removed and another 4 μm thick mold is formed out of photoresist (Fig. 5.23e). The last 2 μm of gold are electroplated, and the mold, seed, and sacrificial layers are removed and the device is released in a critical point dryer (Fig. 5.23f). The device is plated in two steps in order to simplify the process to form the electroplating mold and to facilitate cofabrication with designs of different thicknesses. Fig. 5.24 shows a microphotograph of a fabricated device both with and without the electroplating steps, and Fig. 5.25 shows an SEM image of the device.

Deflections of fixed-free cantilever test structures, measured with a white light interferometer before and after release, revealed that the z-directed stress gradient, $\nabla\sigma_z$, varied from 0-3 MPa/μm across the wafer [49]. This corresponds to upward deflections of up to 1.5 μm, for cantilevers that are 250 μm in length. The RF MEMS metal contact switches exhibited no measurable deflection (Fig. 5.26).

5.4 Measurements

All measurements were performed on a probe station in a standard laboratory environment without atmosphere or pressure control. However, there was a low pressure nitrogen flow to reduce the effects of humidity. At room temperature, the pull-in and release voltages varied from 67-74 V and 65-73 V respectively, for tens of devices. This variation is due to the non-uniformity in the electroplating thickness across the wafer.

5.4.1 Temperature Measurements

The metal contact RF MEMS switch exhibits no measurable deflection from 25 ^{o}C to 105 ^{o}C (Fig. 5.26). This results in a robust device versus temperature, as well as relaxed packaging requirements. On the other hand, a 150 μm long fixed-free cantilever deflects $\sim$250 nm over the same temperature range - demonstrating the effect of the device topology on the thermo-mechanical behavior.

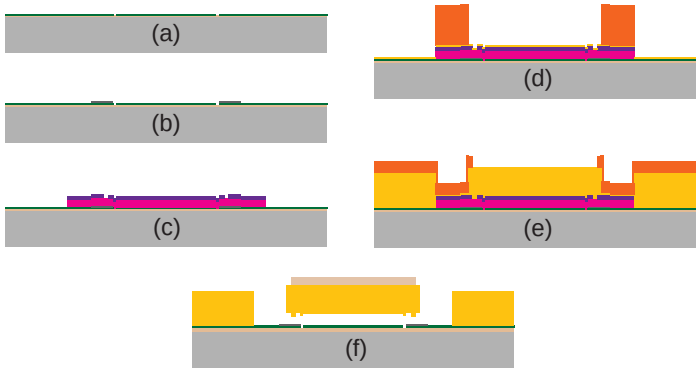

Figure 5.23: Fabrication sequence of the RF MEMS metal contact switch.

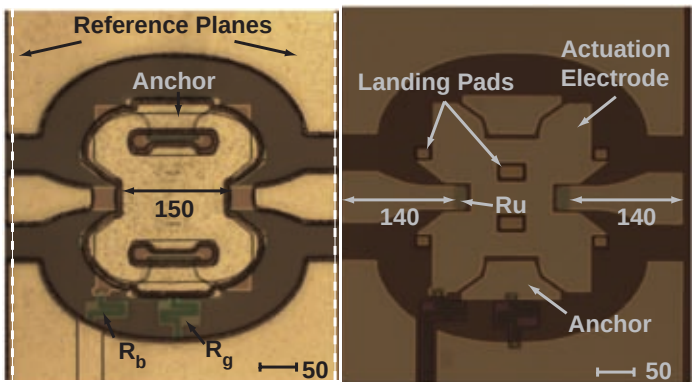

Figure 5.24: Microphotograph of fabricated device and bottom electrode. All dimensions are in μm.

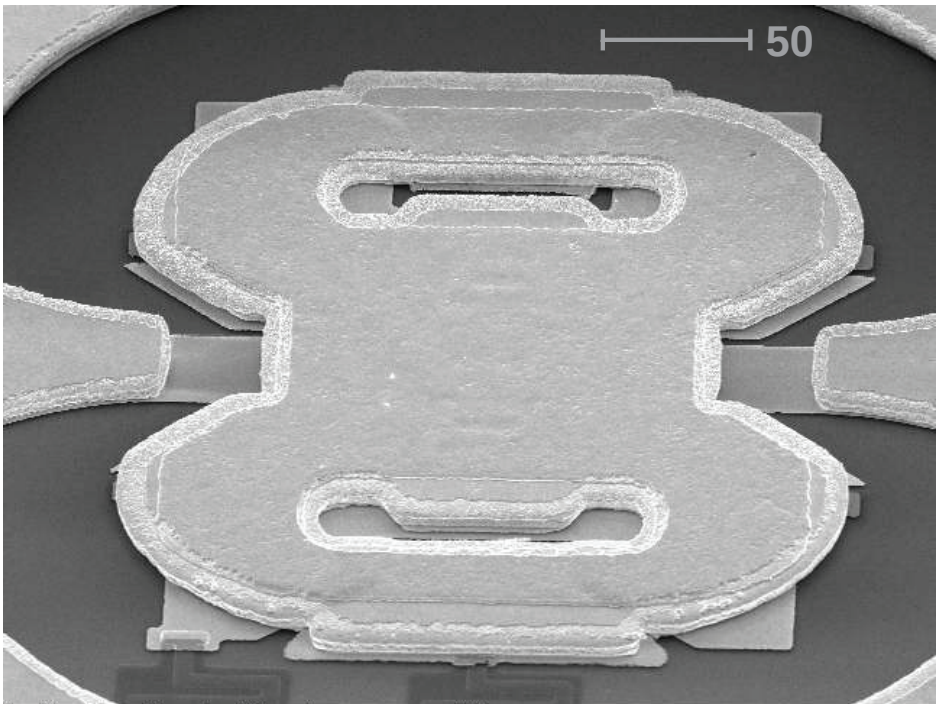

Figure 5.25: SEM image of fabricated device. All dimensions are in μm.

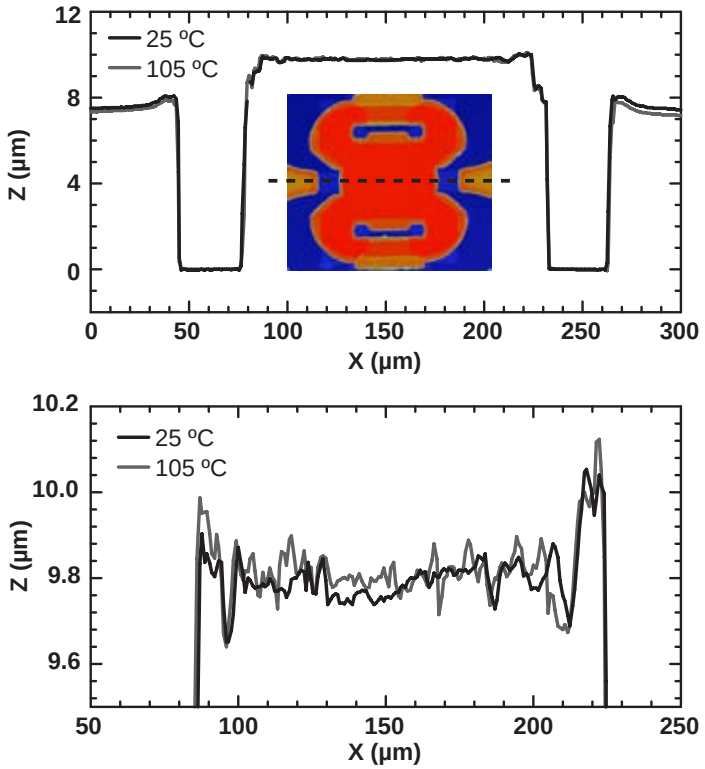

Figure 5.26: Measured profile of the device at 25 and 105C (top), and close-up view of plate (bottom).

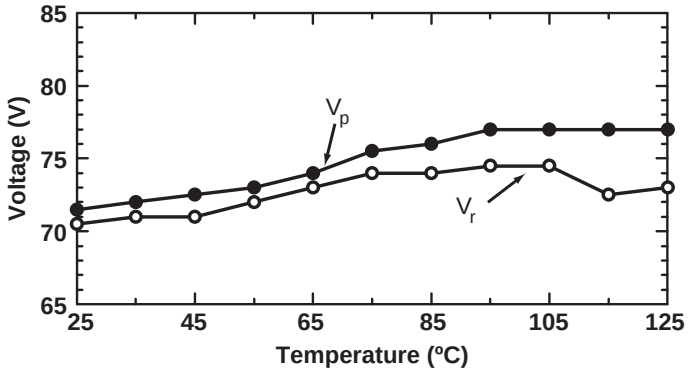

Figure 5.27: Measured pull-in and release voltages versus temperature.

Fig. 5.27 shows a typical pull-in and release voltage measurement versus temperature. For temperatures from 25-125 ^oC, the measured pull-in voltage is 71-77 V (unipolar voltage) [49]. The release voltage is 71 V at 25 ^oC and increases to 75 V at 105 ^oC before decreasing at higher temperatures. This may be due to the increased adhesion of the gold contact as the temperatures rise past the softening point of gold. FEM simulations predict no significant change in the pull-in voltage and the profile measurements show no significant deformations due to temperature, so the increase in pull-in voltage is likely due to temperature dependent substrate charging.

5.4.2 DC Measurements

The switch resistance versus voltage was measured using a 4-wire method. Typical resistances are shown in Fig. 5.28 for several devices. The switch resistance varied from 2.5-0.8 Ω for voltages of 75-100 V, with a typical resistance of 1-2 Ω at 90 V actuation voltage. However, several switches exhibited switch resistances as low as 0.7 Ω. It is seen that the switch resistance is entirely dominated by contaminants. Furthermore, the DC current handling capability of the device was measured to be >1 A (Fig. 5.29). The resistance changes versus DC current because the temperature rise in the contact affects both the resistivity of the material and the size of the contact asperity.

Field emission currents between the actuation electrode and MEMS plate were measured with a Keithley 2400-C source-meter. The device was actuated continuously for one hour (at 25°C and 85°C) and the actuation current was measured ∼20 times per second (Fig. 5.30). It is hypothesized that the current spikes are microplasma driven discharges which erode sharp asperities on the electrode and the underside of the MEMS plate [60]. At higher temperatures, the current spikes are more significant (up to 50 nA) and correspond to an increase in emission behavior. Still, this current is intermittent and has no effect on the switch performance.

5.4.3 RF Measurements

Fig. 5.31 presents the measured S-parameters of the switch along with the response predicted by the simplified circuit models shown in the figure for both the *open-*

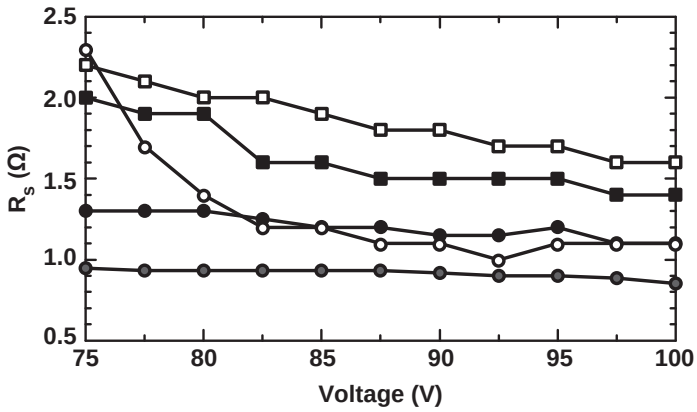

Figure 5.28: Measured switch resistance versus voltage for several devices.

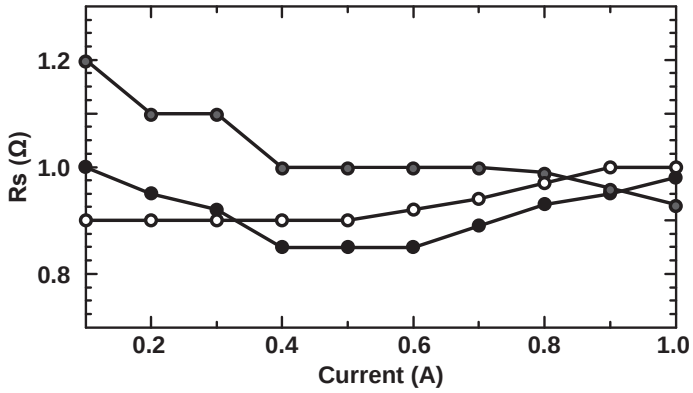

Figure 5.29: Measured switch resistance versus DC current. The switches were fully operational after passing 1 A of DC current.

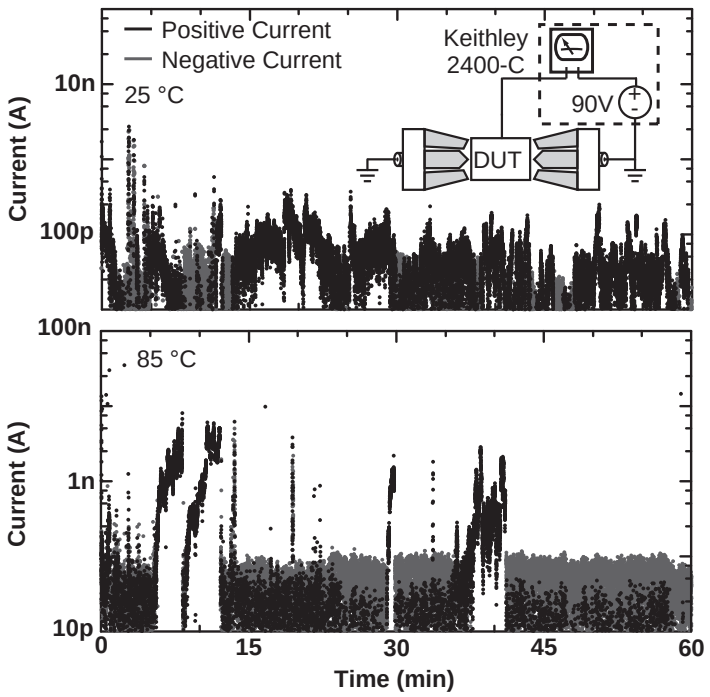

Figure 5.30: Emission current for 90 V actuation at 25°C and 85°C. The atmosphere was a standard lab environment with flowing nitrogen.

and *closed*-state [49]. The measurements were taken from 0.1-40 GHz, and are in good agreement with the simulations from Section 5.2.6 and the simplified models shown in the figure. In the open-state, the measured isolation is equivalent to an 8 fF capacitance, resulting in >20 dB of isolation at 20 GHz. In the closed-state (with an actuation voltage of 90 V), the fitted switch resistance for this measurement is 1.6 Ω, and the switch is very well matched to 40 GHz (S_{11} <-25 dB).

The linearity characteristics of the devices were measured at a center frequency of 1.96 GHz. Fig. 5.32a presents the test setup for a two-tone IIP2 and IIP3 measurement. The two tones were 25 MHz offset from the center frequency (50 MHz apart), and the isolators were well matched up to the third harmonic. It was found that the IIP3 of the device is >69 dBm and the IIP2 is >110 dBm (Fig. 5.32b) and is limited by the passive intermodulation that arises from the interface between the probe tips and CPW metallization and the substrate (for which the IIP3 and IIP2 were measured to be 70 and 115 dBm, respectively, on a thru-line). The measurements were taken at several input power levels from 17 to 25 dBm. Fig. 5.33a presents the test setup for measuring the harmonic power of the 2nd and 3rd harmonics and the measured results. In order to demonstrate the high-linearity nature of the metal-contact switch, a 2 W WCDMA signal was passed through the switch and a thru-line. The output of the two were compared and showed no difference whatsoever (Fig. 5.33b).

5.4.4 Mechanical Measurements

The switching time was measured to be 10.6-5.1 μs for actuation voltages of 75-100 V, and the release time was measured to be 5.0 μs. The mechanical frequency response was also measured. Respectively, the actuation signal and electrostatic force for this test are,

$$V_{act} = V_{DC} + V_{AC}\sin(\omega t) \tag{5.17}$$

$$\begin{aligned} F_e &= \frac{1}{2}C_b V_{act}^2 \\ &\approx \frac{1}{2}C_b(V_{DC}^2 + \frac{V_{AC}^2}{2} + 2V_{DC}V_{AC}\sin(\omega t)) \end{aligned} \tag{5.18}$$

V_{DC} is the DC bias voltage around which there is an AC swing, V_{AC}, at angular frequency, ω. C_b is the bias capacitance from Sec. 5.2.6. Furthermore, a low power RF

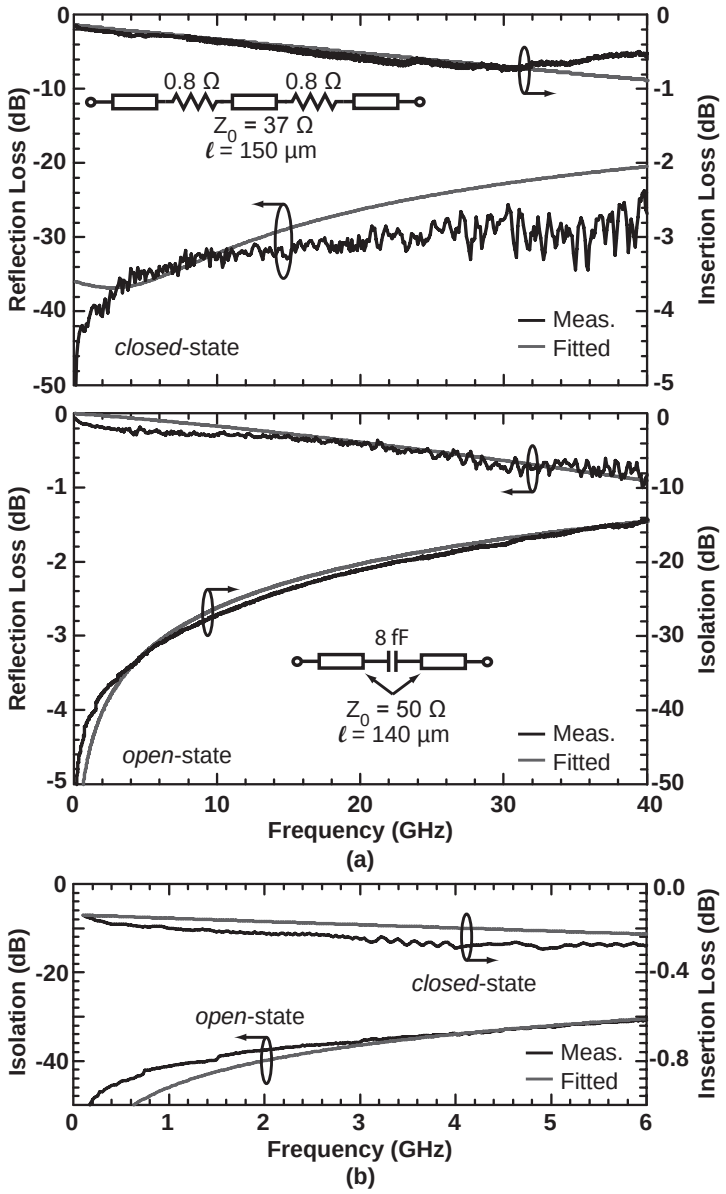

Figure 5.31: (a) Measured and fitted S-parameters with simplified circuit models from 0.1-40 GHz; and (b) expanded view of isolation and insertion loss from 0.1-6 GHz.

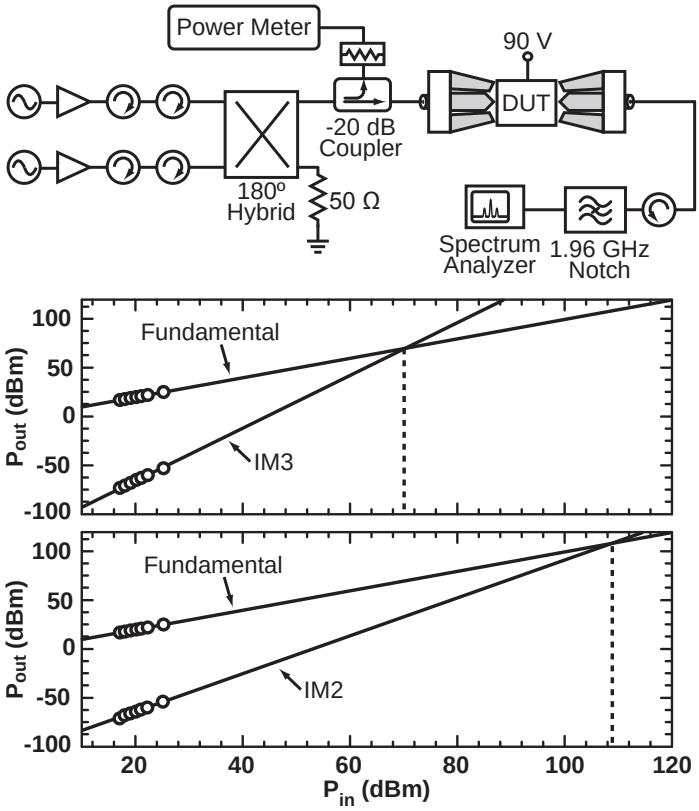

Figure 5.32: (a) Linearity test setup, and (b) measured IIP3 (top) and IIP2 (bottom). Limited by test setup.

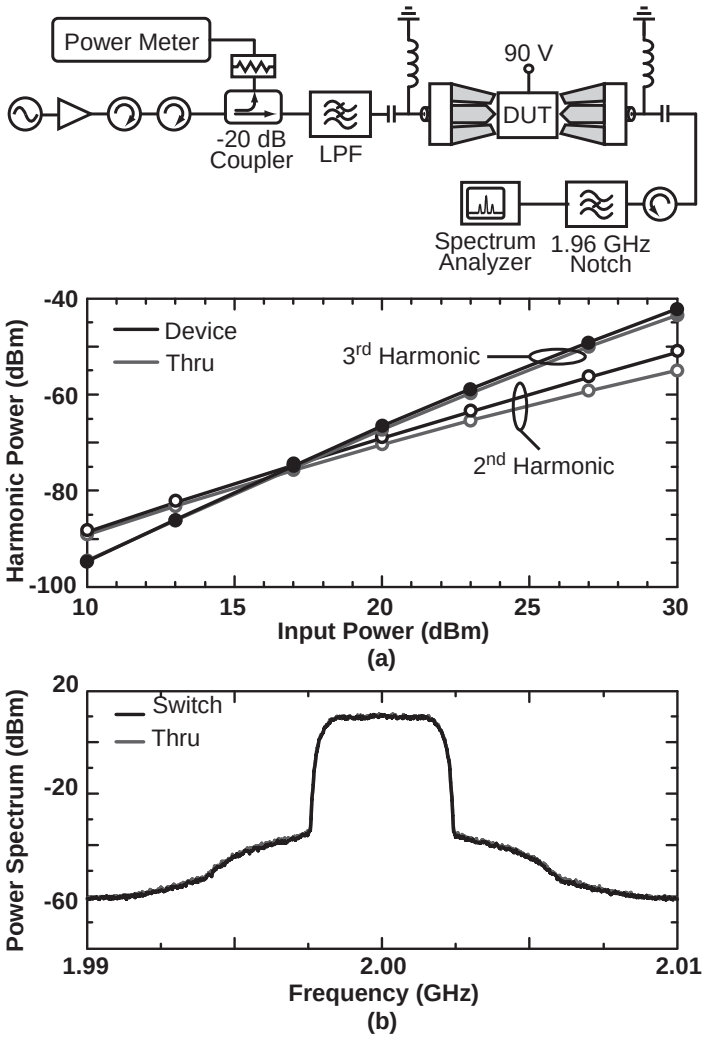

Figure 5.33: (a) Harmonics test setup and measured results, and (b) WCDMA signal at the output of a switch and a thru-line (channel power of 2 W). Limited by test setup.

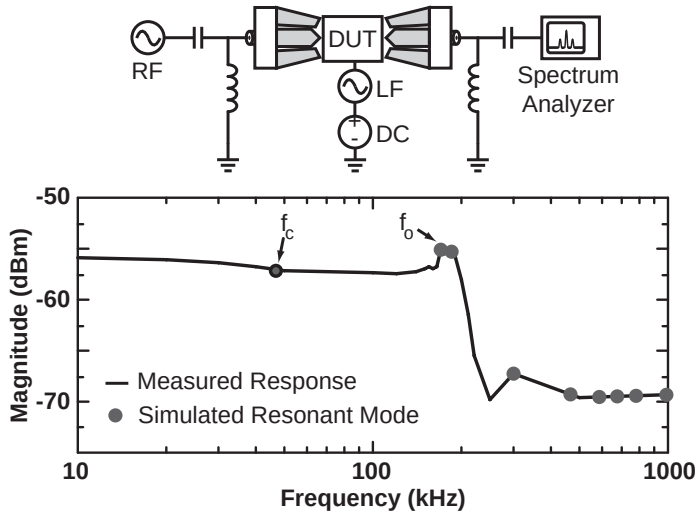

Figure 5.34: Test setup and measured mechanical response of the RF MEMS metal contact switch, along with resonant modes predicted by FEM.

signal is being fed into the device at f_{RF} = 20 GHz. The parallel plate component of the up-state capacitance, C_{pp}, is modulated by the electrostatic force at the frequency of the actuation signal, resulting in the actuation signal being AM modulated with the RF signal. The magnitude of the tones modulated around the RF carrier correspond to the mechanical response of the switch for the actuation frequency [1]. The DC voltage was 50 V and the AC low-frequency voltage was 12 V. The measured response is presented in Fig. 5.34. The resonant modes predicted by FEM are also shown in the figure. The measurement agrees well with simulation. The first two dominant modes are measured to be at 170 and 185 kHz and with fitted mechanical Q values of 1.08 and 1.06, respectively.

There is a slight decrease in the response prior to the first resonant mode due to the fact that the resonant frequency of the device is much greater than the squeeze-film cut-off frequency given by [1, 61],

$$\omega_c = \frac{\sigma_c g_0^2 P_a}{12\mu r^2} \tag{5.19}$$

$$\sigma_c = \pi^2(1 + \frac{1}{\eta^2}) \tag{5.20}$$

where g_0 is the nominal gap, P_a is the ambient pressure, μ is the viscosity of the gas, r is the characteristic length of the plate, and η is the aspect ratio of the movable plate.

For a square plate, the cut-off squeeze number is $\sigma_c = 2\pi^2 = 19.74$. For this device, at standard temperature and pressure, the squeeze-film cut-off frequency is 46 kHz.

5.4.5 Reliability, Creep, and Power Handling

The reliability, creep, and power handling measurements were performed with the test setup shown in Fig. 5.35. For the reliability test, the switch was cycled at 10 kHz with various levels of RF power at 500 MHz. Periodically, the switch resistance was measured with a 4-wire measurement to confirm that the switch was still operational. Fig. 5.36 presents the measured reliability results for several devices cold-switched at 2-5 W and hot-switched at 100-500 mW at 25°C and 85°C (2 W, 25°C data from [49]). The results show that for an incident RF power of 5 W, the reliability is >100M cycles at 25°C and >10M cycles at 85°C. At 2 W, the reliability was measured at >200M cycles at both temperatures. Finally, at 100 mW hot-switched, the reliability was measured to be >100M at 25°C and >1B at 85°C; and at 500 mW hot-switched, the reliability is >1M cycles. The increase in reliability at higher temperatures, in this particular case, may be due to the decomposition of certain contaminants at elevated temperatures. Note that in the 100 mW/hot-switched case, the contacts were subject to periodic electrical cleaning - in the other cases, the incident power levels were sufficient to self-clean the contacts.

Fig. 5.37 presents the measured reliability data for several devices under a cold-switched incident RF power of 10-25 W at 25°C. The results show a reliability of >10M cycles at 10-20 W of incident RF power, and >1M cycles for an incident power of 25 W. At 85°C, the devices failed at <10k cycles for these power levels. All experiments were performed without a hermetic package.

SEM scans of the contact area of a failed device after 500 million cycles at 2 W show that the failure in the device was due to excessive temperature increase arising from the build up of contaminants (which is expected due to the increase in the contact resistance). Thus, the lifetime of the switch is readily extendable with the implementation of a hermetic package [11, 32].

Fig. 5.38 presents the measured S-parameters of the switch before and after handling 10 W of RF power for 1 hour (no cycling, continuous actuation) [49]. The

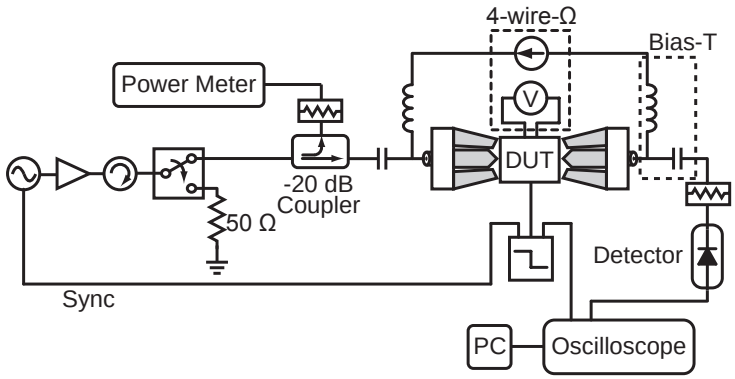

Figure 5.35: Test setup for creep, reliability, and power handling measurements.

results show that the switch is robust for an extended period of time under high-power conditions.

The device was also tested under prolonged hold-down conditions to test resistance to creep. For these tests, the 4-wire setup in Fig. 5.35 is removed, and the DC port of the bias-T is grounded. For the creep test, the device was held down continuously for 24 hours, and the pull-in voltage was measured every 5 minutes (with a pull-in measurement taking 15 seconds). The results are shown in Fig. 5.39 for several devices at 25 ^{o}C and 85 ^{o}C. The pull-in voltage drifts 3-4 V over the 24 period at 25°C. At 85°C the, the pull-in voltage drifts by about 12 V, but the measurement starts to fluctuate greatly after 16 hours due to substrate charging. However, when the device is pre-stressed with a 24 hour hold-down period at room temperature, there is very little drift after the initial break-in. This suggests that the creep and charging mechanisms tend to offset each other in this particular case.

In order to demonstrate the robustness of the switch under prolonged hold-down measurements, the device was held actuated continuously for 12 days while passing 2 W of RF power at 2 GHz. The resistance and pull-in voltage were measured once a day, and this was the only time the actuation voltage was removed ($\sim$2 minutes per day). The results are shown in Fig. 5.40. The device was still fully operational after the test, and showed no signs of degradation.

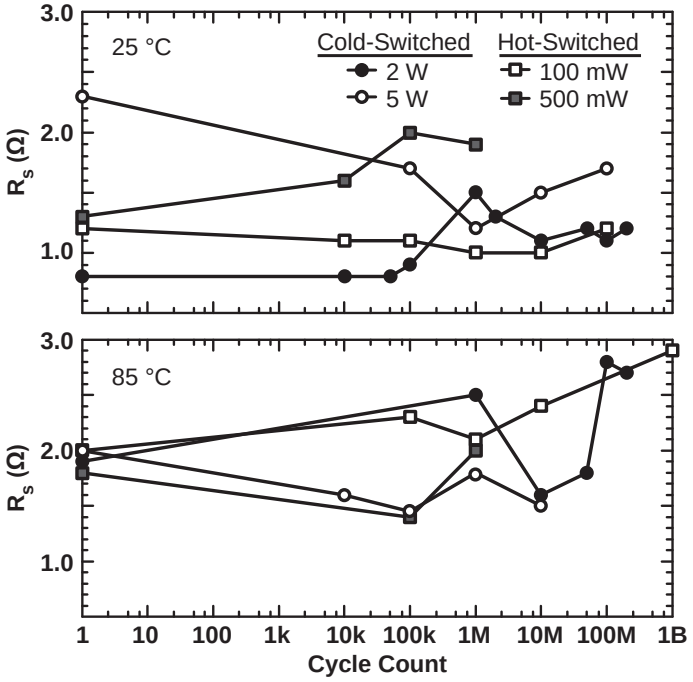

Figure 5.36: Reliability of the metal contact switch for 0.1-5 W of RF power and 90 V actuation at 25 ^{o}C (top) and 85°C (bottom). All devices failed as *open*.

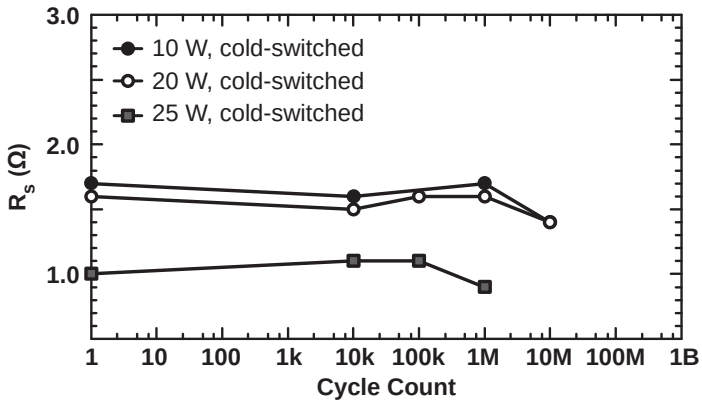

Figure 5.37: Reliability of the metal contact switch for 10-25 W of RF power and 90 V actuation at 25°C. All devices failed as *closed*.

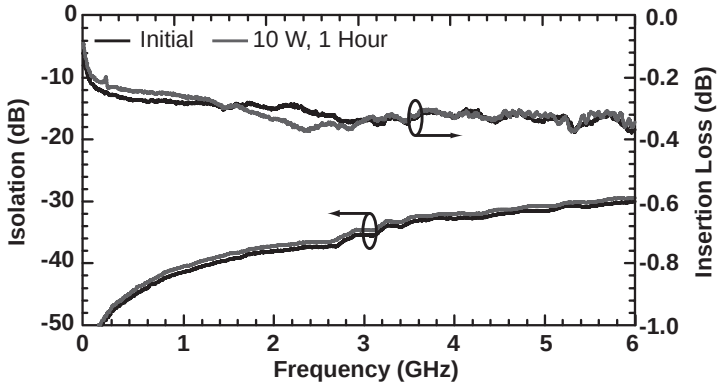

Figure 5.38: Measured s-parameters before and after passing 10 W of RF power continuously for 1 hour.

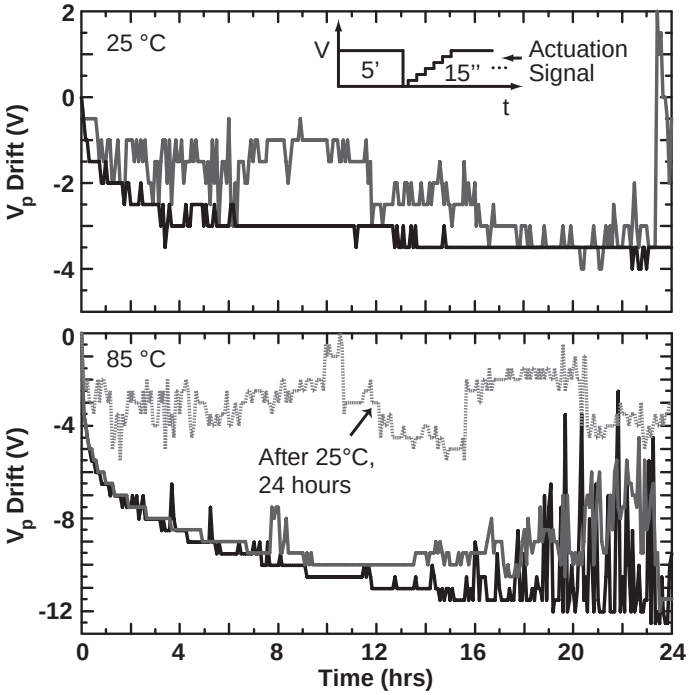

Figure 5.39: Measured pull-in voltage for several devices under prolonged actuation conditions at 25 ^{o}C and 85 ^{o}C.

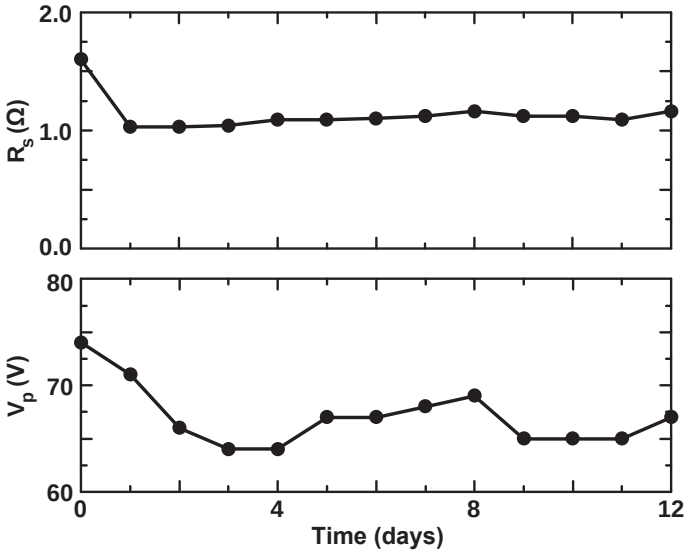

Figure 5.40: Measured switch resistance (top) and pull-in voltage (bottom) under prolonged hold-down conditions (unipolar actuation) and passing 2 W of RF power at 2 GHz.

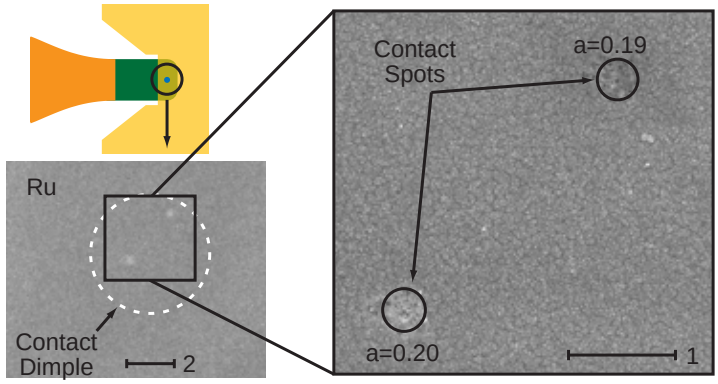

Figure 5.41: SEM image of the bottom contact area of the switch implemented with an Ru/Au contact. The power through the switch was <1 mW with <1000 cycles. All dimensions in μm.

5.4.6 Contact Area

Fig. 5.41 presents SEM images of a typical contact area of a device actuated with a bias voltage of 90 V and an Au/Ru contact. The equivalent contact radius of all of the spots taken together is $a = 0.28$ μm. The theoretical spot size calculated with (5.2) results in a spot size of $a = 0.22$ μm for a pure ruthenium contact and $a = 0.55$ μm for a pure gold contact for a contact force of 1.5 mN.

The contact area presented in Fig. 5.41 is under low-power/cold-switched conditions, where the effects of temperature and arcing are insignificant. Under these conditions, the contact area behaves as a classical contact described by (5.2). However, under high-power operation, the elevated temperatures will increase the contact area due to an increase in the viscoelasticity of the materials. Under hot-switching operations, arcing will cause material transfer and significantly damage the contact.

Fig. 5.42 shows functional contacts after 1M cycles operating at 10 W under cold-switched conditions and 500 mW under hot-switched conditions. Under cold-switched conditions, the contact area is increased to a = 0.41 μm, but the real contact area is still much smaller than the contact dimple area. Only a few asperities still come into contact. Conversely, for the hot-switched case, the material in contact is removed from the contact due to arcing and over time, the entire area of the contact dimple is damaged. The shape of the damaged area is exactly the shape of the contacting dimple.

Fig. 5.43 presents a set of failed contacts after 20M cycles - again at 10 W/cold-

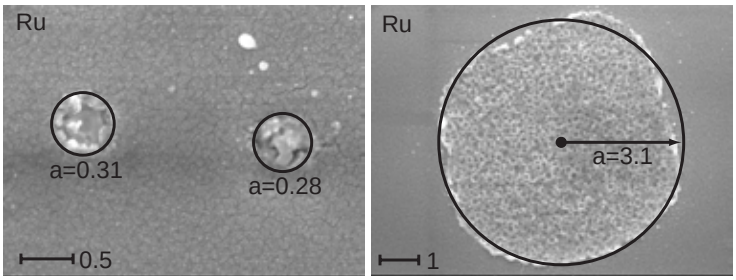

(a) (b)

Figure 5.42: SEM images of functional contacts after 1M cycling operations - (a) 10 W, cold-switched, and (b) 500 mW, hot-switched.

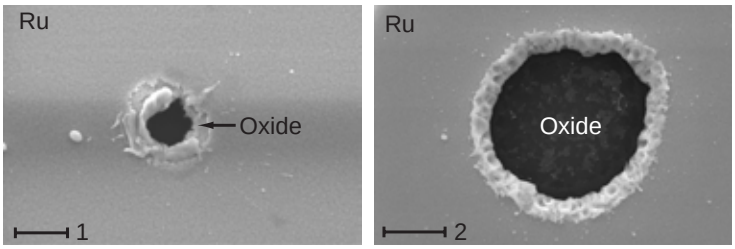

(a) (b)

Figure 5.43: SEM images of failed contacts after 20M cycling operations - (a) 10 W, cold-switched, and (b) 500 mW, hot-switched.

switched and 500 mW/hot-switched. The 10 W/cold-switched contact failed as a short-circuit, while the 500 mW/hot-switched contact failed as an open circuit. In both cases, the contact has been destroyed and the underlying oxide is visible. However, in the 10 W/cold-switched case, this damage may have occurred as the contact was broken to view under the SEM. In the 500 mW/hot-switched contact, the damage is a natural progression from what was seen in Fig. 5.42b, and the entire material underneath the contact dimple is removed.

It is clear that at medium power levels, hot-switching is far more damaging to the contacts than cold-switching at even high power levels. In order to improve the reliability, a thicker bottom metallization and ruthenium contact may be employed in addition to hermetic packaging and arc-suppression techniques [62, 63].

5.5 High Performance Switching Networks

The low loss, high power handling, high linearity, and good reliability of the metal-contact RF MEMS switch makes it ideal in implement high-performance switching networks. Fig. 5.44a presents the high-performance metal-contact switch in an SP4T configuration. The device has an active area of 750×720 μm^2 (1200×930 μm^2 including bias pads and CPW ground metallization). The bias lines are all routed to the top of the switching network using high-resistivity SiCr (∼5 k$\Omega/\square$) to facilitate probing or bonding.

Measured S-parameters are presented in Fig. 5.44b. Since the device is symmetric about port 1, the performance of port 2 and port 4 referenced to port 1 is identical to port 3 and port 5, respectively. The DC resistance is 2-2.5 Ω, and is mostly dominated by contaminants. The insertion loss is <0.5 dB up to 7 GHz and <0.8 up to 15 GHz. The SP4T provides >44 dB of isolation at 1 GHz, >30 dB of isolation at 6 GHz, and >22 dB of isolation at 15 GHz. Only two probes were used in the measurement, so the isolation performance is expected to improve with all ports terminated with 50 Ω (by about 6 dB).

Fig. 5.45a presents the high-performance metal-contact switch in an SP6T configuration. This configuration has an active area of 750×1020 μm^2 (1200×1250 μm^2

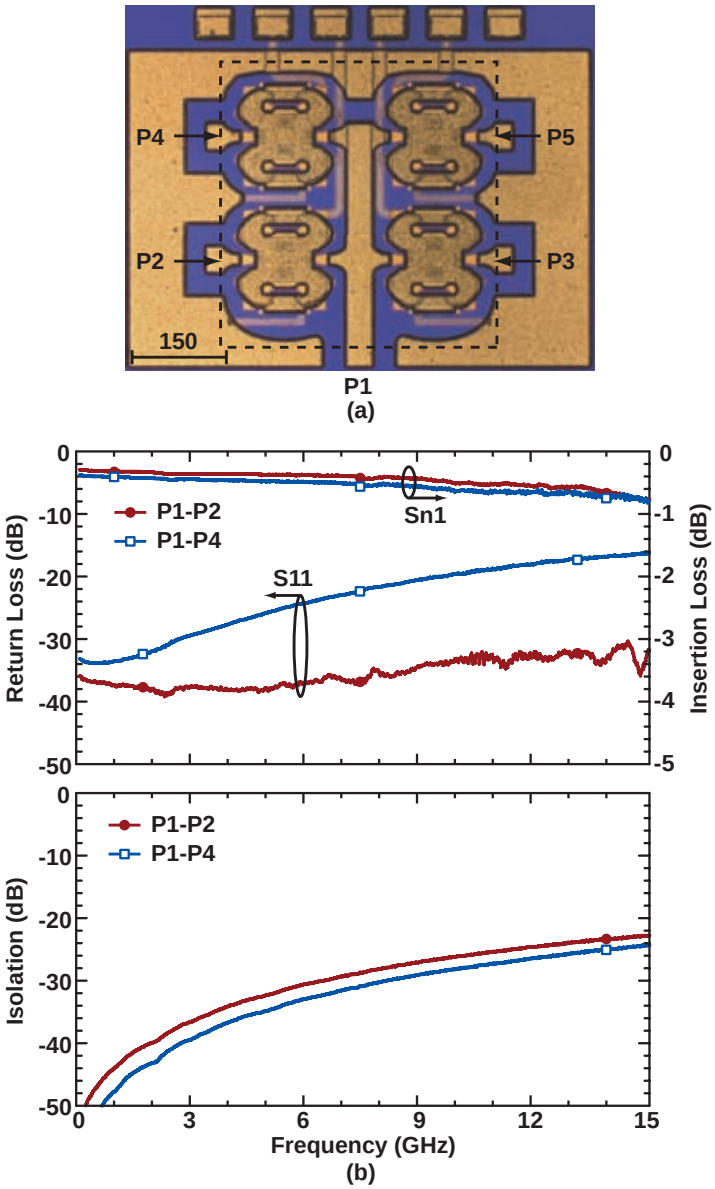

Figure 5.44: (a) Microphotograph of SP4T switching network, and (b) measured S-Parameters. All dimensions are in μm. Terminating all ports with 50 Ω will improve isolation performance by $\sim$6 dB.

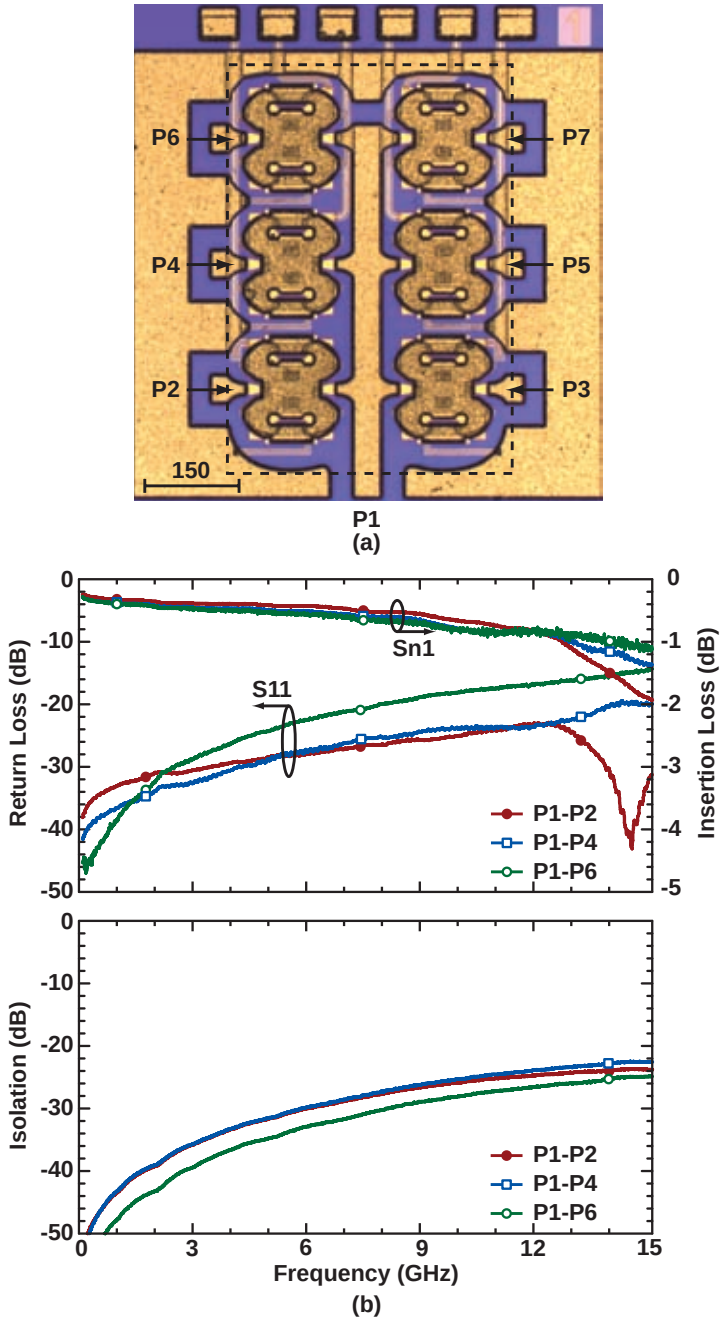

Figure 5.45: (a) Microphotograph of SP6T switching network, and (b) measured S-Parameters. All dimensions are in μm. Terminating all ports with 50 Ω will improve isolation performance by $\sim$6 dB.

including bias pads and CPW ground metallization). Due to the symmetry about port 1, the port pairs (P2,P3), (P4,P5), and (P6,P7) exhibit identical performance with reference to port 1. Measured S-parameters are presented in Fig. 5.45b. The device achieves a DC contact resistance of $\sim$2 Ω, again dominated by contaminants. The isolation is $>$44 dB at 1 GHz, $>$30 dB at 6 GHz, and $>$22 at 15 GHz. Again, the results are expected to improve with all ports terminated with 50 Ω ($\sim$6 dB improvement).

5.6 Conclusion

An RF MEMS switch exhibiting high reliability ($>$100 million cycles), high linearity, and high power handling ($>$10 W) has been demonstrated. The switch uses an inverted crab topology to achieve mN-level contact and restoring forces, and is able to maintain mN-level forces over a variety of stress effects and temperature ranges. The switch has been shown to be reliable under prolonged switching and hold-down conditions. With packaging, the reliability and power handling would be easily extendable without any change in the contact metallurgy. High-performance switching networks were also demonstrated with compact size and good isolation up to 15 GHz.

This chapter is largely a reprint of material submitted for publication to *IEEE Transactions on Microwave Theory and Techniques*, 2012; C. D. Patel and G. M. Rebeiz. The chapter also includes some material published in *IEEE MTT-S International Microwave Symposium Digest*, 2012; C. D. Patel and G. M. Rebeiz. In both cases, the dissertation author is the primary author of the source material.

Chapter 6

Conclusion and Future Work

6.1 Summary

Chapters 2 and 3 present mN-force metal-contact switches based on large-force electrostatic actuators. The use of the tethered-cantilever topology reduces device sensitivity to stress effects (z-directed stress gradients and biaxial stresses) and temperature. The devices are a significant improvement over traditional cantilever based RF MEMS switches for mN-force designs. Measured results show switch resistances of $<1\ \Omega$ with Au-Ru contact metals and little dependence of switch performance on temperature. Reliability measurements performed on the second generation tethered switch (chapter 3) show power handling >5 W, reliability >100 million cycles (cold-switched), and robust performance under long-term actuation.

Chapter 4 presents a compact metal-contact RF MEMS switch capable of achieving 0.38-0.72 μN of contact force at 90-100 V actuation, and 0.46 μN of release force. The high restoring force, relative to the contact force, makes the design less prone to stiction failures. Measured results showed a switch resistance of 2 Ω and the pull-in voltage changes by 2 V over a temperature range of 25-125 ^{o}C. The design, developed for medium-power applications (5-10 W), was also used to implement compact switching networks. Series/shunt, SP4T, and SP6T configurations were demonstrated, achieving low insertion loss and high isolation.

Chapter 5 presents a high performance RF MEMS metal-contact switch for high-power applications. The switch is based on an inverted crab topology to achieve

stress- and temperature-insensitivity and a uses a double-break contact for high-isolation and reliability. Measured results show low switch resistance ($< 1\ \Omega$), high isolation (C_{up}=8fF), high linearity (IIP3>69 dBm, IIP2>110 dBm), and high reliability and power handling (>100 million cycles at 2 W, and >10 million cycles at 10 - 20 W, cold-switched). The device was also robust under prolonged actuation conditions, and was tested under continuous actuation for 12 days passing 2 W of RF power. The switch was also used to demonstrate high performance SP4T and SP6T switching networks.

All switches presented in this dissertation were fabricated at the Nano3 cleanroom at UCSD. All measurements were performed on unpackaged devices in standard laboratory environments (not cleanroom).

6.2 Future Work

Low-cost packaging techniques, yield analysis, and failure analysis were not considered in this dissertation. The switches were tested to >100 million cycles in unpackaged environments, but the lifetime can be readily extended with packaging. Furthermore, the packaging can improve the yield and power handling of the devices, but the degree to which this is the case is not clear and needs further study. Process improvements, such as dry release and CVD sacrificial layers, can also improve the yield and performance of the switches.

To achieve higher-power switches, the design techniques described in the dissertation can be used to create actuators with even larger contact and release forces (>5-10 mN) - with minimal sensitivity to stress and temperature effects. Thick hard-metal contacts can be implemented to better withstand arcing and material transfer effects from hot-switching events [64]. The larger real contact area may make it feasible to implement micro-heat-sinks on the contacts to reduce the contact temperature and improve the power handling. Furthermore, the larger forces may reduce packaging requirements from hermetic to near-hermetic and may facilitate lower cost packaging.

On the other end of the scale, miniature switches (on the scale of 20-50 μm) can be designed to be CMOS compatible [52]. The switches would then be highly integrated and inexpensive. However, the materials in a typical CMOS process flow can exhibit

very large stresses and gradients, so the devices must be insensitive to stress effects by design - even with the small dimensions. Such switches can be implemented in arrays to achieve large power handling.

6.3 Summary of Appendices

Appendix A presents simulation and measurement results of various switching networks implemented with the devices presented in chapter 4 and chapter 5.

Appendix B presents the design, fabrication, and measurement of a high-Q 3- and 4-bit digitally tunable varactor based on RF MEMS switched capacitors.

Appendix C presents the detailed fabrication procedure for the UCSD metal-contact switch process used to fabricate the metal-contact RF MEMS switches presented in this dissertation.

Appendix A

Miscellaneous RF MEMS Switching Networks

A.1 Compact Double-Pole Double-Throw Switching Networks

Double-pole double-throw (DPDT) switching networks (also called cross-over switches) have many applications in electronic systems - such as antenna diversity in communications systems and switching matrices in satellite systems, among others. For this configuration, two non-adjacent devices are in the *closed*-state, while the other two non-adjacent devices are in the *open* state. Therefore, each of the two input ports can be switched to each of the two output ports - allowing this configuration to be used as a building block for the synthesis of $N \times M$ switching networks.

A compact DPDT switching network implemented with the metal-contact RF MEMS device presented in chapter 4 is presented in Fig. A.1a. The device has an active area of 610×490 μm^2 (710×720 μm^2 including bias pads and CPW ground planes), and is nearly symmetric at all four ports (resulting in identical performance at all four ports). In the center, a high-resistivity bias line connects the actuation electrodes of the two non-adjacent devices together, so that only two actuation pads are required to switch the device. Fig. A.1b presents measured S-parameters of the DPDT (with V=90 V at one pad, and V=0 V at the other). S11 is shown, but all Snn are identical.

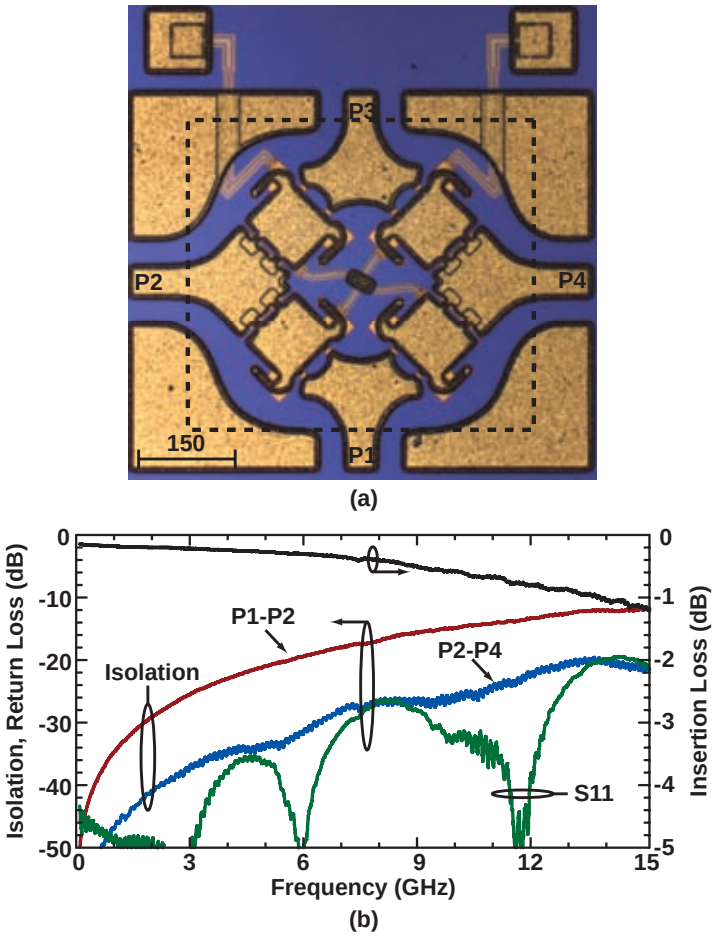

Figure A.1: (a) A compact DPDT switching network, and (b) measured S-parameters. All dimensions are in μm.

A high-performance DPDT switching network implemented with the metal-contact switch presented in the chapter 5 is presented in Fig. A.2a. The device has an active area of 820×820 μm^2 (920×1040 μm^2 including bias pads and CPW ground planes), and is symmetric at all four ports (resulting in identical performance at all four ports). Only two pads are used to actuate the switch, as with the DPDT presented in Fig. A.1, due to a bias line in the center of the switching network connecting the actuation electrode of the two non-adjacent devices together. Fig. A.2b presents measured S-parameters of the DPDT (with V=90 V at one pad, and V=0 V at the other). Again, S11 is shown but all Snn are identical.

For both switching networks, the mechanical performance of the networks (reliability, switching time, sensitivity to stress effects and temperature, etc.) are expected to be identical to the performance of a single device.

A.2 Simulations of a Single-Pole Double-Throw Switch for High Frequency Applications

This subsection presents the design and simulation of a single-pole double-throw (SPDT) switch based on a series/shunt configuration of the switch presented in chapter 4. Such switches are commonly used as transmit/receive switches in communication and radar systems, among other uses. The SPDT is implemented in a grounded-CPW configuration with a 100-μm-thick silicon substrate. The device, which is 890×370 μm, is shown in Fig. A.3. A lumped model is shown in Fig. A.4.

Simulation results are presented in Fig. A.5. For the simulation, port 3 is actuated (passing), while port 2 is un-actuated (blocking). The device shows a simulated insertion loss of $<$2 dB (with a DC switch resistance of 2 Ω per switch) and an isolation of $>$36 dB up to 67 GHz. The match is $>$10 dB, and can be improved with a matching network. With a lower switch resistance (which can be achieved with contact cleaning and packaging), the insertion loss and isolation performance can be improved. Thus, the switching network is a good candidate for compact, high-performance (linearity, reliability, loss, and power handling), broadband SPDT.

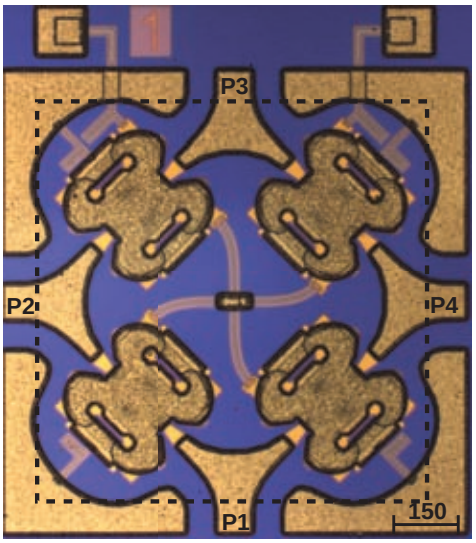

(a)

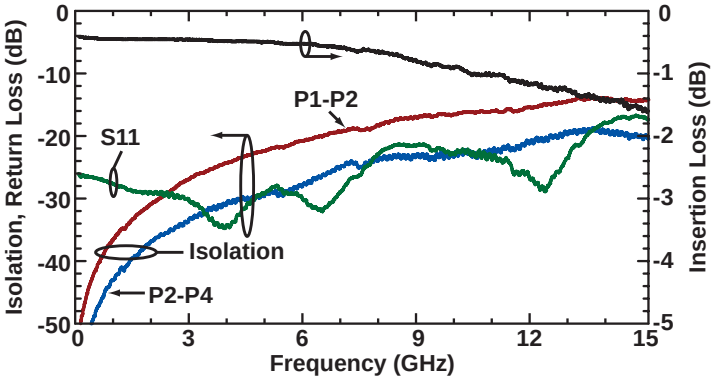

(b)

Figure A.2: (a) A high-performance DPDT switching network, and (b) measured S-parameters. All dimensions are in μm.

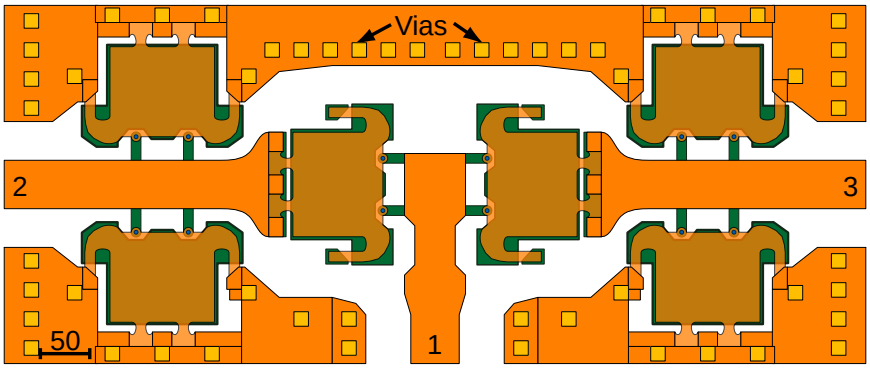

Figure A.3: Top view of series/shunt SPDT switching network. All dimensions are μm.

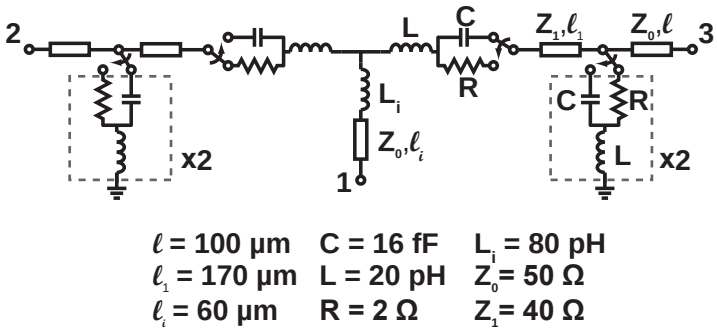

Figure A.4: A lumped element model of the SPDT switching network.

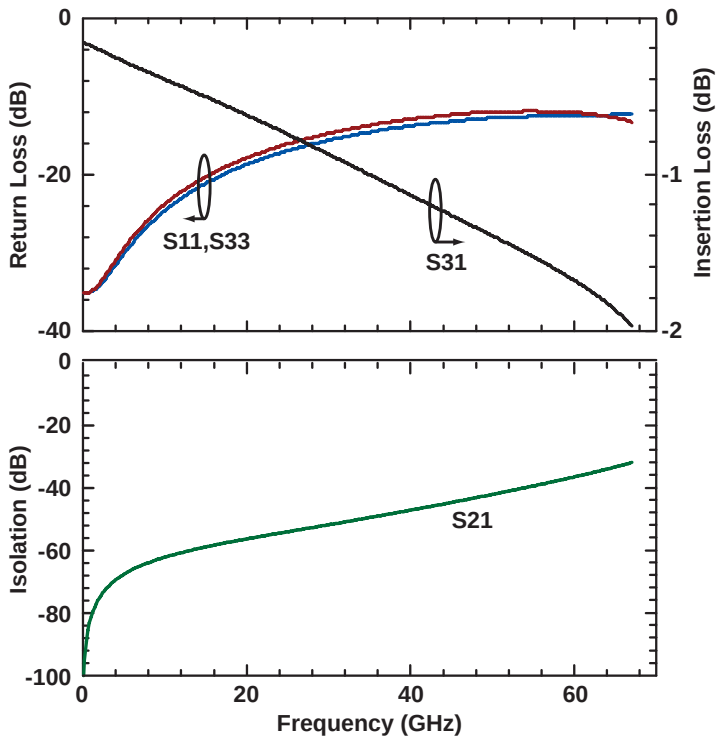

Figure A.5: Simulated S-parameters of the SPDT. Port 3 is actuated, and Port 2 is isolated.

Appendix B

High-Q 3-/4-Bit RF MEMS Digitally Tunable Capacitors for 0.8-3 GHz Applications

B.1 Introduction

RF MEMS varactors are attractive alternatives to solid-state devices as tuning elements for many applications, such as filters, antenna matching networks, and phase shifters. This is due to the lower loss, higher linearity, higher power handling of RF MEMS elements as compared to solid-state varactors [1]. There are many recent examples of RF MEMS based varactors, both analog and digitally tuned [40,65–67]. Digitally tuned varactors have an advantage in scalability and a linear tuning relationship with the digital code, and can have a large capacitance ratio without mechanical instability concerns.

In this appendix, a high-Q digitally tunable capacitor, based on the switched capacitor developed at UCSD [68] and suitable for 1-port applications, is described. The varactor is implemented in a circular configuration to minimize series inductance, and can be implemented in either planar circuits or in 3-D resonators with cavity posts. Furthermore, a thick bottom electrode process is implemented for the switched capacitor and results in a Q improvement of 25-65% at 2 GHz, depending on the tuning state.

B.2 Design

Fig. B.1a presents the top view of the digitally tunable capacitor. The design consists of binary weighted tunable capacitors implemented using the UCSD RF MEMS switched capacitor on a quartz substrate [68, 69]. The UCSD switched capacitor design features analog tuning capability in addition to its two digital states, as well as reduced dielectric charging due to the separation of the RF line from the actuation electrode. In order to maintain current-symmetry, each binary weighted bit is decomposed into two half-bits which are arranged symmetrically in a circular configuration. The digital capacitor is implemented in a 3- and 4-bit configuration (4-bit design is shown in Fig. B.1a). The two configurations are identical except that in the 3-bit configuration, the least significant bit (BIT 0) is removed. A circular design is chosen so as to reduce the parasitic inductance associated with 15 (or 14) different capacitors. The one-port device is fed using a short 70-Ω coplanar waveguide (CPW) line for S-parameter measurements.

Fig. 1b presents the lumped-element model of the digitally tunable capacitor. Each switched capacitor has a nominal up-state and down-state capacitance of 50 fF and 250 fF, respectively (a capacitance ratio of C_r=5). Table B.1 presents a comparison of simulated performance between designs with the switched capacitors arranged in straight and circular configurations, and fitted to a simple RLC model. All of the designs presented in Table B.1 have the same CPW feeds and the RF MEMS switched capacitors are spaced as close as possible (within fabrication limits).

The wide and long designs (see Table B.1) are 1.14$\times$2.52 mm^2 and 2.64$\times$0.91 mm^2, respectively. While the circular design occupies a larger area (2.0$\times$1.8 mm), its parasitic inductance is lower than the parasitic inductance of varactor designs with the RF MEMS arranged in a straight line. All of the designs exhibit roughly the same capacitance ratio, but the tuning range of the circular design is shifted slightly higher due to the larger offset capacitance. Thus, for a given capacitance value, the circular design is usable to higher frequencies.

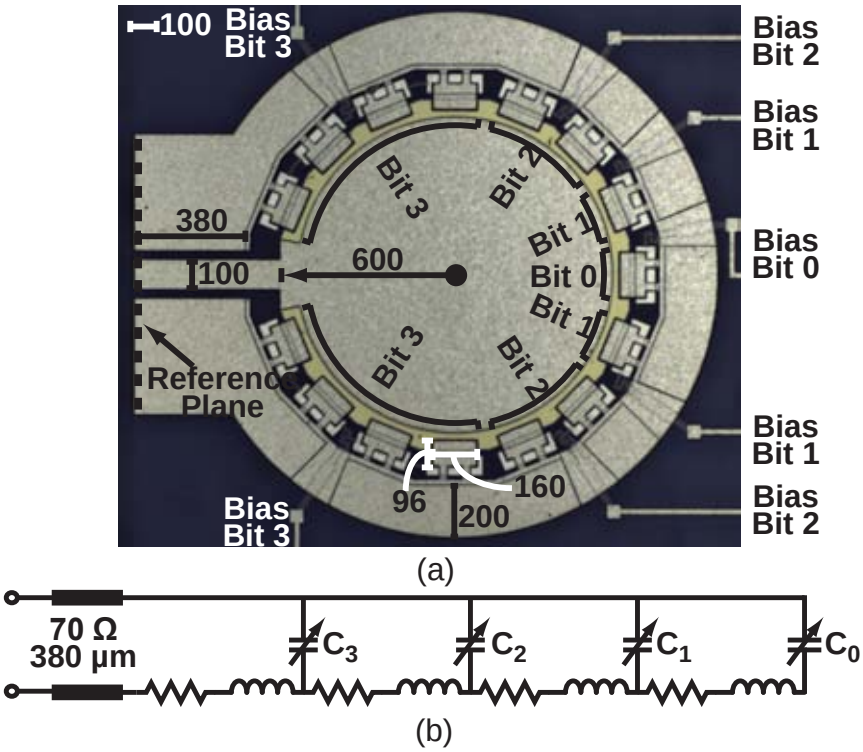

Figure B.1: (a) Micro-photograph of a 4-bit digitally tunable varactor and (b) lumped-element model. The 3-bit version is identical but implemented without BIT 0. All dimensions are in μm.

Table B.1: Comparison of Varactor Designs

	C_{min}			C_{max}			
	C (pF)	L (pH)	f_0 (GHz)	C (pF)	L (pH)	f_0 (GHz)	C_r
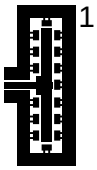 1	0.81	451	8.33	3.74	508	3.65	4.6
2	0.82	457	8.23	3.82	505	3.63	4.7
3	0.87	391	8.63	3.99	428	3.85	4.6

[1]The *wide* design, [2]the *long* design, and [3]the *circular* design.

B.3 Fabrication

Fig. B.2a presents a cross section of the standard UCSD switched capacitor process and the new ”thick-metal” process. Both are based on a 4 μm movable gold cantilever and an isolated actuation pad. The standard UCSD fabrication sequence employs a thin metal layer (0.3 μm) underneath the dielectric layer, and the resistance formed by this thin metal layer is the main limiting factor for the switched capacitor Q. In order to reduce the losses and increase the device Q, a ”thick metal” bottom-electrode process is employed to increase the metal thickness under the dielectric. The quartz substrate was first etched 0.7 μm deep with a reactive ion etch, and subsequently filled with gold using a self-aligned process to avoid alignment error (Fig. B.2b). From here, the process continues with the first step of the UCSD switched capacitor process [68]. The thick metal does not affect the C-V characteristics of the RF MEMS switched capacitor. To further improve the switched-capacitor Q on the ”thick-metal” devices, the ground ring was plated an extra 4 μm (8 μm total metal thickness) to reduce the RF losses.

Fig. B.3 presents the measured CV-curve of a single switched capacitor co-

fabricated with the digitally tunable capacitor. The up-state capacitance is 58 fF and the down-state capacitance is 230 fF, resulting in a C_r of 4. The C_r is reduced from a nominal of 4.5 due a negative stress gradient in the cantilever, resulting in a slight downwards curl and an increase in the up-state capacitance [68].

B.4 Measurement

All measurements were performed in a standard laboratory environment with unpackaged devices in open air conditions. The measured digitally tuned capacitance values are presented in Fig. B.4a. The data is representative of both the ”thick-metal” process and the standard UCSD process. The capacitance can be tuned from 1.0 - 1.25 pF to 3.75-3.85 pF in 8 or 16 linear steps, resulting in C_r=3.75-3.1, respectively. This is in good agreement with simulations, with differences arising from fabrication variations (stress gradient and dielectric roughness) resulting in a lower C_r for the unit RF MEMS switched capacitor. The 3-bit and 4-bit designs result in the same performance in Q, parasitic inductance, etc., except that the 4-bit design has BIT 0 (see Fig. B.1) which results in a finer resolution than the 3-bit design.

In addition to digital tuning, a DC bias can be applied on the RF line to obtain additional analog tuning due to the zipping effect on the down-state switched capacitors [68]. For example, in the 3-bit case, an additional 30 fF of analog tuning is available for the lowest capacitance state (all up) by applying a 5 V bipolar square-wave to the RF line. While in the highest tuning state, an additional 120 fF of analog tuning range is available (Fig. B.4b). With the exception of state 0, the capacitance for all of the states can also be reduced in an analog fashion by reducing the hold-down voltage from 60 V to 40 V. The local analog tuning range increases with the tuning state because the number of down-state RF MEMS devices increases.

Fig. B.5a presents the extracted parasitic inductance versus tuning state. The inductance arises mostly from the effective length of the return current path. For the first half of the tuning range (BIT 1 and 2 actuated), the current follows a longer path when compared to the second half of the tuning range (BIT 3 actuated), as shown in Fig. B.5a. This results in a difference of 100 pH when switching from state 3 to state 4 (or

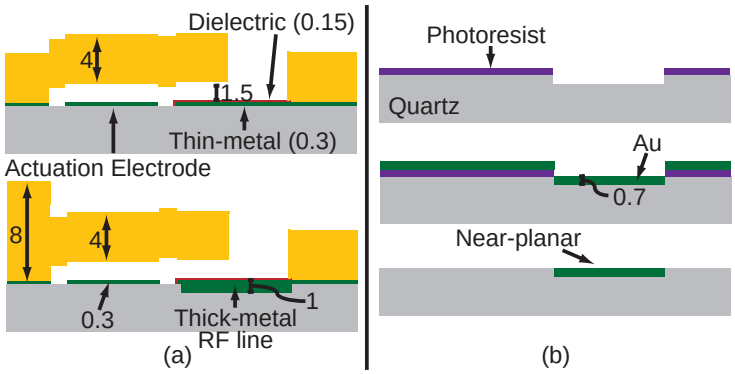

Figure B.2: (a) A comparison of standard and ”thick-metal” devices and (b) process sequence for forming the thick metallization. All dimensions μm.

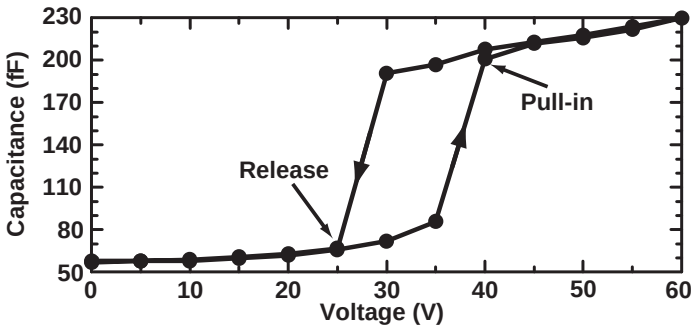

Figure B.3: Measured capacitance-voltage behavior of a single switched capacitor co-fabricated with the digitally tunable varactor.

state 7 to state 8 for the 4-bit design).

A similar effect is seen in the measured varactor Q versus digital tuning state (Fig. B.5b). Again, the resistance is due to the effective length of the return current and, as a result, the topology results in a device Q which can be kept high even for larger capacitance values. Fig. B.5b also presents measurements for ”thick-metal” devices versus devices fabricated with the standard process. The measurements show a 25-65% increase in the varactor Q for the ”thick-metal” devices due to a reduction in the series resistance. The data shown in Fig. B.5b was taken at 2 GHz. At 1 GHz, the measured Q was $>$100 for all tuning states for both the standard and ”thick-metal” processes.

The switched capacitor is usable up to $\sim$3 GHz with C_{max}=3.8 pF and L=300 pH (series resonance: $\sim$4.7 GHz). The measured Q and effective reactance ($X = -1/\omega C + \omega L$) versus frequency are shown in Fig. B.6 for the minimum and maximum capacitance state, as well as for the standard and ”thick-metal” processes. It is seen that the ”thick-metal” devices can maintain $Q > 60$ up to 2 GHz for all tuning states. At 3 GHz, the reactance at the maximum capacitance state is only -8 Ω which results in a Q of $\sim$26-20 for Rs=0.3-0.4 Ω. Detailed power handling measurements were not performed on this device, but it is expected to follow closely the power handling characteristics presented in [68], allowing watt-level operation.

B.5 Conclusion

This appendix presents the design, fabrication, and measurement of 3- and 4-bit digitally switched capacitors using a novel topology which maintains a high Q as the capacitance increases. The device Q was shown to increase substantially with a thicker bottom-electrode, and the device maintains a $Q > 60$ at 2 GHz for all capacitance values.

This appendix is largely a reprint of material accepted for publication to *IEEE Microwave and Wireless Components Letters*; C. D. Patel and G. M. Rebeiz. The dissertation author is the primary author of the source material.

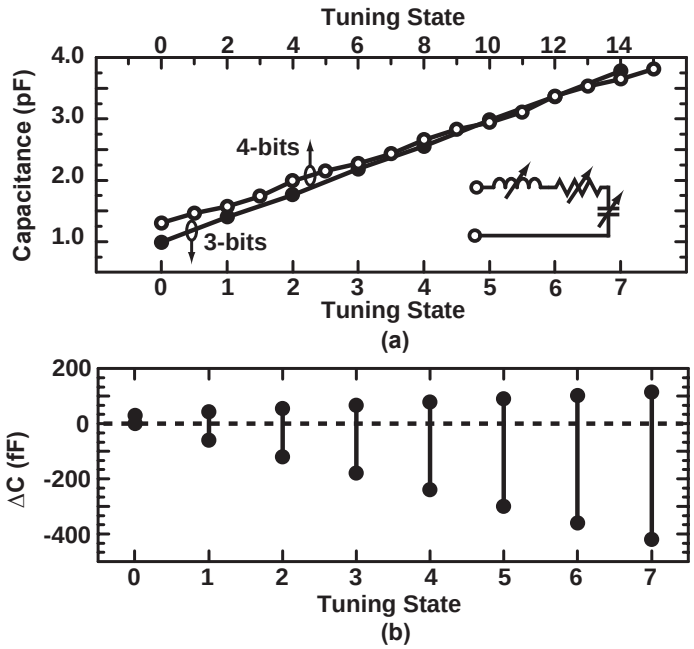

Figure B.4: (a) Digitally tuned capacitance states for 3- and 4-bit configurations, and (b) analog tuning range vs tuning state (3-bit design).

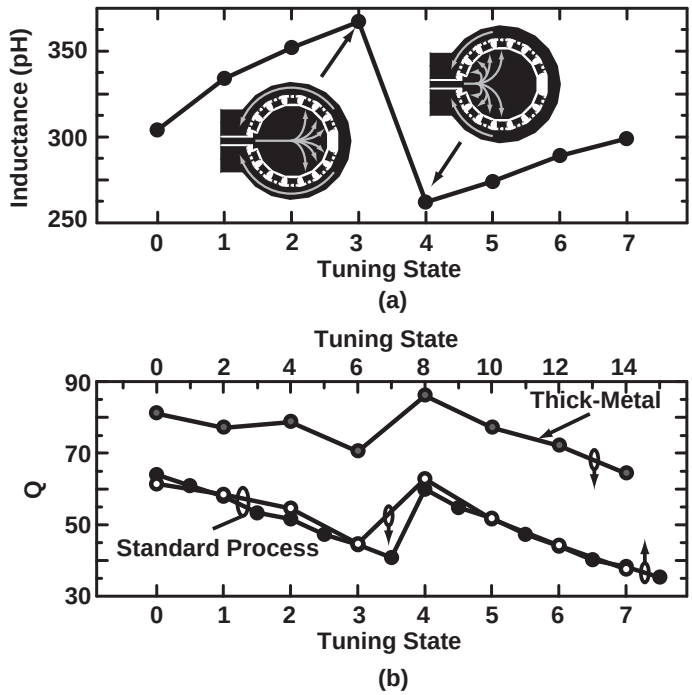

Figure B.5: (a) Parasitic inductance and (b) Q vs digital tuning state. Q is taken at 2 GHz.

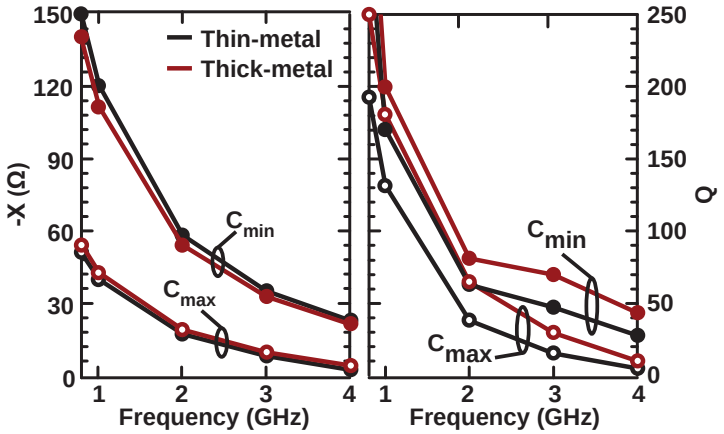

Figure B.6: Capacitive reactance and Q for min/max capacitances from 0.8 to 4 GHz.

Appendix C

The UCSD Metal-Contact Process in Detail

The slides on the following pages of this appendix describe the detailed fabrication sequence for the UCSD RF MEMS metal-contact switch process. This fabrication process was used to construct all metal contact switches described in this dissertation. The process was developed by the dissertation author at the Nano3 clean room facility at the University of California - San Diego in 2009 starting from the UCSD switched capacitor process [68] with input from Isak Reines, Rashed Mahameed, Alex Grichener, and Hojr Sedaghat-Pisheh.

Chirag Patel - 1

Bias Lines

- Clean Wafer:
  - Acetone/IPA/Methanol/DI Water
- Dehydrate Wafer:
  - 2' @ 100°C
  - 1' @ 150°C right before spin
- Photolithography
  - Spin NR9-1500PY @ 4K RPM, 40", ACCL=35
  - Prebake: 2' @ 150°C
  - Expose: 10" (for lamp intensity 7.5)
  - Postbake: 1' @ 100°C
  - Develop: RD6:DI 3:1 for 10", rinse with DI
- Sputter SiCr ~1200 °A (use test slides) (Denton Discovery)
  - Target 5 kΩ/square, use test slides for calibraton
  - RF Power=300W, rotation=65, pressure=4.2mT, ~30'
    - N2 = 3 for 10', 4 for 20', Ar = 41 (adjust Ar to get pressure)
- Lift-off
  - Lift-off in acetone with ultrasonic agitation
  - Soak in RR2 @110°C for 10'-30'
  - Clean and dry wafer
- Inspect and dektak

UCSD Jacobs | Electrical and Computer Engineering

Chirag Patel - 2

Bottom Metal

- Sputter Ti/Au/Ti (200/3000/200 °A) (Use test slides) (Denton)
  - Use substrate heater in denton for in-situ dehydration
    - Set temperature to 70 °C, wait for overshoot to 100 °C, turn off
  - DC Power=200W,rotation=65,pressure=4.1-4.3mT, 55"/6'/55"
    - Ar = 40, N2=0, adjust Argon to achieve pressure
    - Adjust sputtering times based on test slides
- Photolithography
  - Spin S1818 @ 4K RPM, t=35", ACCL=255
  - Prebake: 90" @ 105 °C
  - Expose: 15"
  - Develop: MF 319 for 35" (wait for PR to clean, add 10")
- Etch (use test slides)
  - Etch top Ti in HF:DI 1:10 for about 5", rinse with DI
  - Etch Au in KII Gold Etchant for ~1'10", rinse with DI
  - Remove PR in acetone/IPA/methanol/DI water
  - Etch bottom and top Ti in HF:DI 1:10 for about 5", rinse with DI
  - Clean and dry wafer
- Inspect and Dektak

UCSD Jacobs | Electrical and Computer Engineering

Dielectric

- PECVD Nitride (~1500 °A) (Oxford Plasmalab PECVD)
  - Use Filmmetrics and Si test pieces for calibration/test
  - Use recipe: OPT-SiNx-High Qual (HF/LF)
    - Temperature=350 °C
    - 5%SiH4 95%N2=400sccm
    - NH3=22sccm
    - Pressure=650mT
  - HF RF power (13.56MHz)=20W for 13”
  - LF RF power (100-300kHz) = 20W for 7”
  - Time=11’ (check with test sample)
- Photolithography
  - Spin 1818 @ 4K RPM, t=35”, ACCL=255
  - Prebake: 90” @ 105 °C
  - Expose: 15”
  - Develop: MF-319 for 35”
- Inspect
- RIE (Oxford P80) (use test slides!)
  - Use recipe: isotropic Ox/Nit/Si etch
    - CF4= 35sccm,
    - O2=3sccm
    - Pressure=75mT
  - RF Power=100W (not the default value, remember to change!)
  - Time= ~50”, use test pieces to check
- Clean Wafer (Acetone/IPA/Methanol/1165@80°C for 30’/rinse and dry
- Inspect and Dektak

UCSD Jacobs | Electrical and Computer Engineering

Bottom Contact

- Dehydrate wafer
  - 2’ @ 100°C
  - 1’ @ 150°C right before spin
- Photolithography (use test sample)
  - Spin NR9-1500 PY @ 4K RPM, t=40”, ACCL=35
  - Prebake: 2’ @ 150 °C
  - Expose: 10”
  - Postbake: 1’ @ 100 °C
  - Develop in RD6:DI 3:1 for 10”
  - Inspect
- Sputter Ru/Ti (Denton) (use test slides)
  - Use RF Bias for in-situ Argon plasma clean prior to sputtering
    - Pressure = 4.2mT, RF Bias = 100W for 30”
  - Sputter Ru
    - RF Bias=0W, DC Power = 100W, pressure = 4.2 mT, Ar=~43, time = ~6’ (calibrate with test slides)
  - Sputter Ti
    - DC Power = 200W, maintain other settings, time = 55”
- Lift-off
  - Lift-off in acetone with ultrasonic
  - Clean wafer with acetone/IPA/methanol/DI water
  - Soak in 1165 @ 80 °C for 30’, rinse thoroughly and dry
  - Descum with Tepla, 2’ @ 150W, 250mT
- Inspect and Dektak

UCSD Jacobs | Electrical and Computer Engineering

Contact Dimples

- Deposit sacrificial layer (use test sample)
  - PMMA-C4 (0.55um)
    - Pre-spin 500 RPM, ACCL=30, t=10”
    - Spin @ 1700 RPM, ACCL=255, t=40” (characterize)
    - Bake @ 135 °C for 10’ then 180 °C for 2’
    - Check thickness with filmmetrics on the side of the wafer*
  - PMGI-SF5 (or SF6) (0.3um)
    - Pre-spin 500 RPM, ACCL=30, t=10”
    - Spin @ 1400 RPM, ACCL=255, t=40”
    - Bake @ 135 °C for 10’, then 180 °C for 2’
    - Check thickness with filmmetrics using PMMA program*
- Pattern dimples (use test sample)
  - Spin S1805 @ 3K RPM, ACCL=255, t=40”
  - Prebake: 90” @ 105 °C
  - Expose: 15”
  - Develop: MF-319 for 50”
  - Flood expose: 45”
  - Remove PR in Microdev:DI 1:1 or MBIK:IPA 1:3**, rinse and dry
- Inspect and Dektak

*Verify filmmetrics accuracy with test sample and Dektak
** Avoid exposing sample to air until it is thoroughly rinsed

UCSD Jacobs | Electrical and Computer Engineering

Sacrificial

- Dehydrate wafer
  - 2’ @ 130 °C
- E-Beam hard mask (use test sample)
  - Evaporate ~700°A of Ti at 8-10°A/S (use crystal for thickness)
  - Tape on back side of wafer, placement on edge of ring
  - Real thickness will be less, ~35 nm or so (check with test sample)
- Sputter hard mask
  - Sputter ~35 nm of Ti to ensure good coverage
  - Power=150W for ~3’ (use test slides)
- Pattern hard mask
  - Spin 1818 @ 4K RPM, t=35”, ACCL=255
  - Bake, expose, develop as usual
  - Etch Ti in HF:DI water 1:10
  - Flood expose for 45”, develop in Microdev:DI 1:1 for 30”
- Dry etch sacrificial layer (Oxford P80)
  - Use O2 clean recipe
  - Chiller 35, power=50W, pressure=50mTorr,flow=50sccm, time=10’
  - Increase power to 150W, time=3’
- Veeco
- Remove Ti in HF:DI water 1:10, rinse and dry
- Inspect and Dektak

UCSD Jacobs | Electrical and Computer Engineering

Chirag Patel - 7

First Electroplating

- Sputter Seed Layer (Denton, 200 nm) (use test slides)
  - In-situ dehydrate at 110 °C (watch out for overshoot)
  - Sputter Ti/Au/Ti with parameters:
    - Power = 200/300/200 W
    - Pressure = 4.2/5.2/4.2 mT (adjust Ar ~42/48/42)
    - Rotation = 65
    - Time = 55”/3’/55” (check test slides)
- Electroplating mold
  - Dehydrate wafer (if significant time has passed)
  - Spin SPR-220-7 (use test sample)
    - Prespin @ 500 RPM for 10”, ACCL=30
    - Spin @ 1.7 RPM for 40”, ACCL=255 (check with test sample)
    - Bake 30” @ 60 °C then ramp to 105 °C and bake for 2’
  - Let it sit overnight
  - Expose and develop
    - Use edge bead mask to expose for 90”, and develop with MF24A
    - Align and expose for 25” (check with test sample)
    - Let sit for 2 hours
    - Develop with MF24A for ~4’ (check with test sample)
  - Inspect and Dektak (should be 9-10 um)
- Etch top Ti in dilute HF (1:10) (use test slide)
- Electroplate (BDT-510 and electroplating setup) (use test slide)
  - Heat solution to 55 °C, let stabilize for 45’, stir bar at 200 rpm
  - Set source for 2mA/cm^2 current density, plate 8um (check progress with dektak periodically, rotate wafer
- Flood Expose, remove PR, inspect and Dektak

UCSD Jacobs | Electrical and Computer Engineering

Chirag Patel - 8

Second Electroplating

- Photolithography
  - Spin SPR-220-3 @ 3K RPM, 40” (pre-spin 500 RPM, 10”)
  - Prebake 90” @ 105 °C
  - Expose 20”
  - Develop in MF24A for 40”
- Etch top Ti in dilute HF (1:10)
- Electroplate (BDT-510 and electroplating setup)
  - Heat solution to 55 °C, let temperature stabilize for 45’
  - Set source for 2mA/cm^2
  - Electroplate 2um
  - Periodically check the thickness with Dektak
  - Rinse thoroughly for at least 30” when removing sample from solution
- Strip PR
  - Flood expose for 1’
  - Develop in MF24A
- Clean electroplating setup
  - Rinse plating clip and backing plate thoroughly
- Inspect and Dektak

UCSD Jacobs | Electrical and Computer Engineering

Seed Metal Etch

- Photolithography
  - Spin 1827 @3K RPM for 40", ACCL=255
  - Prebake: 90" @ 100 °C
  - Expose: 30" (overexpose)
  - Develop: MF319 for 1'30"
  - Realign and expose for 30" (no new PR)
  - Redevelop: MF319 for 1'
  - Inspect, re-expose and develop as necessary
- Etch Ti
  - Dilute HF (1:10) (use test slides), inspect
- Etch Au
  - KII Gold Etchant (use test slides), inspect
- Etch Ti (same as above
- Rinse and dry
- Inspect and Veeco
  - Make sure that the seed metal is completely removed in areas that are not electroplated
  - Veeco scans to get pre-released profiles

Release

- Initial soak in 1165 at 80 °C for 20'
- Overnight soak in 1165 at 80 °C
  - ***Keep meniscus on wafer during transfer
  - Use larger glass crystallization dish
  - Stir speed 50-100 RPM
- DI rinse
  - Transfer wafer into fresh DI water, keep meniscus on wafer
  - Repeat 2 more times with fresh DI water
- Etch Ti (use test slides)
  - For small samples, use plastic tweezers to hold samples flat
  - For small samples, use small cup
  - Keeping the meniscus on the wafer, tranfer it to the dilute HF:DI (1:10) for the time found with test slides
  - Quickly transfer the wafer back into clean DI water, keeping meniscus (include transfer time in etch time)
  - Transfer wafer into fresh DI water, keep meniscus on wafer
  - Repeat 2 more times with fresh DI water
- Purge DI water
  - Transfer wafer into fresh methanol, keep meniscus on wafer
  - Repeat 2 or more times with fresh methanol
- CPD (Tousimis)
  - Clean machine, fill with methanol
  - Set purge time to 15'
  - Use settings written on machine

Bibliography

[1] G. M. Rebeiz, *RF MEMS Theory, Design, and Technology*. New Jersey: J. Wiley & Sons, 2003.

[2] R. P. Feynman, "There's plenty of room at the bottom," *Engineering and Science*, vol. 23, no. 5, pp. 22–36, Feb. 1960.

[3] A. Hartzell, M. G. da Silva, and H. R. Shea, *MEMs Reliability*. New York: Springer, 2011.

[4] Z. D. Milosavljevic, "RF MEMS switches," *Mikrotalasna revija*, 2004.

[5] B. C. Edwards, "A hoist to the heavens," *Spectrum, IEEE*, vol. 42, no. 8, pp. 36–41, Aug. 2005.

[6] R. Holm, *Electrical Contacts: Theory and Application*, 4th ed. New York: Springer, 1967.

[7] L. Chen, Z. J. Guo, N. Joshi, H. Eid, G. G. Adams, and N. E. McGruer, "An improved SPM-based contact tester for the study of microcontacts," *Journal of Micromechanics and Microengineering*, vol. 22, no. 4, p. 045017, 2012.

[8] J. Shimkat, "Contact materials for microrelays," in *IEEE Int. Conf. Microelectromech. Systems*, Heidelberg, Germany, Jan. 1998, pp. 1901–194.

[9] S. Majumder, J. Lampen, R. Morrison, and J. Maciel, "A packaged, high-lifetime ohmic MEMS RF switch," in *IEEE MTT-S Int. Microwave Symp. Dig.*, Philadelphia, PA, Jun. 2003, pp. 1935–1938.

[10] M. Fujii, I. Kimura, T. Satoh, and K. Imanaka, "RF MEMS switch with wafer level package utilizing frit glass bonding," in *Microwave Conference, 2002. 32nd European*, Sep. 2002, pp. 1 –3.

[11] O. Wunnicke, H. Kwinten, L. van Leuken-Peters, M. in 't Zandt, K. Reimann, V. Aravindh, H. Suy, M. Goossens, R. Wolters, W. Besling, J. van Beek, and P. Steeneken, "Small, low-ohmic RF MEMS switches with thin-film package," in *Micro Electro Mechanical Systems (MEMS), 2011 IEEE 24th International Conference on*, Jan. 2011.

[12] N. Sato, H. Ishii, S. Shigematsu, H. Morimura, T. Kamei, K. Kudou, M. Yano, K. Machida, and H. Kyuragi, "A sealing technique for stacking mems on lsi using spin-coating film transfer and hot pressing," *Japanese Journal of Applied Physics*, vol. 42, no. Part 1, No. 4B, pp. 2462–2467, 2003.

[13] M. Sakata, Y. Komura, T. Seki, K. Kobayashi, K. Sano, and S. Horike, "Micromachined relay which utilizes single crystal silicon electrostatic actuator," in *IEEE Int. Conf. Microelectromech. Systems*, Orlando, FL, 1999, pp. 21–24.

[14] Y. Uno, K. Narise, T. Masuda, K. Inoue, Y. Adachi, K. Hosoya, T. Seki, and F. Sato, "Development of SPDT-structured RF MEMS switch," in *Int. Conf. Transducers, Solid-State Sensors, Actuators and Microsystems*, 2009, pp. 541 –544.

[15] H. S. Newman, J. L. Ebel, D. Judy, and J. Maciel, "Lifetime measurements on a high-reliability RF-MEMS contact switch," *IEEE Microwave Wireless Compon. Lett.*, vol. 18, no. 2, pp. 100–102, Feb. 2008.

[16] D. A. Goins, R. D. Nelson, and J. S. McKillop, "Design of a 20 GHz low loss ohmic contact RF MEMS switch," in *IEEE MTT-S Int. Microwave Symp. Dig.*, Honolulu, HI, Jun. 2007, pp. 371–374.

[17] J. Costa, T. Ivanov, J. Hammond, J. Gering, E. Glass, J. Jorgenson, D. Dening, D. Kerr, J. Reed, S. Crist, T. Mercier, S. Kim, and P. Gorisse, "Integrated MEMS switch technology on SOI-CMOS," in *IEEE Solid-State Sensors, Actuators, and Microsystems Workshop*, Hilton Head, SC, Jun. 2008, pp. 18–21.

[18] N. Nishijima, J.-J. Hung, and G. M. Rebeiz, "Parallel-contact metal-contact RF MEMS switches for high power applications," in *IEEE Int. Conf. Microelectromech. Systems*, Maastricht, Netherlands, Jan. 2004, pp. 781–784.

[19] ——, "A low-voltage, high contact force RF-MEMS switch," in *IEEE MTT-S Int. Microwave Symp. Dig.*, Fort Worth, TX, Jun. 2004, pp. 577–580.

[20] J. Yao and M. Chang, "A surface micromachined miniature switch for telecommunications applications with signal frequencies from dc up to 4 ghz," in *Solid-State Sensors and Actuators, 1995 and Eurosensors IX.. Transducers '95. The 8th International Conference on*, vol. 2, jun 1995, pp. 384 –387.

[21] R. E. Mihailovich, M. Kim, J. B. Hacker, E. A. Sovero, J. Studer, J. A. Higgins, and J. F. DeNatale, "MEM relay for reconfigurable RF circuits," *Microwave and Wireless Components Letters, IEEE*, vol. 11, no. 2, pp. 53 –55, Feb. 2001.

[22] A. De Silva, C. Vaughan, D. Frear, L. Liu, S. Kuo, J. Foerstner, J. Drye, J. Abrokwah, H. Hughes, C. Amrine, C. Butler, S. Markgraf, H. Denton, and S. Springer, "Motorola MEMS switch technology for high frequency applications," in *Microelectromechanical Systems Conference, 2001*, Berkeley, CA, Aug. 2001.

[23] K. Suzuki, S. Chen, T. Marumoto, Y. Ara, and R. Iwata, "A micromachined RF microswitch applicable to phased array antennas," in *IEEE MTT-S Int. Microwave Symp. Dig.*, Anaheim, CA, Jun. 1999, pp. 1923–1926.

[24] D. Mercier, P. L. Charvet, P. Berruyer, C. Zanchi, L. Lapierre, O. Vendier, J. L. Cazaux, and P. Blondy, "A DC to 100 GHz high performance ohmic shunt switch," in *IEEE MTT-S Int. Microwave Symp. Dig.*, Fort Worth, TX, Jun. 2004, pp. 1931–1934.

[25] H. Sedaghat-Pisheh, J. Kim, and G. M. Rebeiz, "A novel stress-gradient-robust metal-contact switch," in *IEEE Int. Conf. Microelectromech. Systems*, Sorrento, Italy, Jan. 2009, pp. 27–30.

[26] H. Sedaghat-Pisheh and G. M. Rebeiz, "Variable spring constant, high contact force RF MEMS switch," in *IEEE MTT-S Int. Microwave Symp. Dig.*, Anaheim, CA, May 2010, pp. 304–307.

[27] A. Fruehling, R. Pimpinella, R. Nordin, and D. Peroulis, "A single-crystal silicon DC-40 GHz RF MEMS switch," in *IEEE MTT-S Int. Microwave Symp. Dig.*, Boston, MA, Jun. 2009, pp. 1633–1636.

[28] J. Oberhammer and G. Stemme, "Low-voltage high-isolation DC-to-RF MEMS switch based on an S-shaped film actuator," *IEEE Trans. Electron Devices*, vol. 51, no. 1, 2004.

[29] H. C. Lee, J. Y. Park, and J. U. Bu, "Piezoelectrically actuated RF MEMS DC contact switches with low voltage operation," *IEEE Microwave Wireless Compon. Lett.*, vol. 15, no. 4, pp. 202–204, Apr. 2005.

[30] R. Robin, O. Millet, K. Segueni, and L. Buchaillot, "Low actuation voltage SPDT RF-MEMS K-band switch using a single gold membrane," in *IEEE Int. Conf. Microelectromech. Systems*, Sorrento, Italy, Jan. 2009, pp. 872–875.

[31] E. Thielicke and E. Obermeier, "A fast switching surface micromachined electrostatic relay," in *Int. Conf. Transducers, Solid-State Sensors, Actuators and Microsystems*, vol. 1, 2003, pp. 899–902.

[32] Q. Ma, Q. Tran, T. A. Chou, J. Heck, H. Bar, R. Kant, and V. Rao, "Metal contact reliability of RF MEMS switches," *Proc. SPIE*, vol. 6463, p. 646305, Jan. 2007.

[33] C. D. Patel and G. M. Rebeiz, "An RF-MEMS switch with mN contact forces," in *IEEE MTT-S Int. Microwave Symp. Dig.*, Anaheim, CA, May 2010, pp. 1242–1245.

[34] P. M. Zavracky, N. E. McGruer, R. H. Morrison, and D. Potter, "Microswitches and mircorelays with a view toward microwave applications," *Int. J. of RF and Microwave Computer Aided Engineering*, vol. 9, no. 4, pp. 338–347, 1999.

[35] T. Seki, Y. Uno, K. Narise, T. Masuda, K. Inoue, S. Sato, F. Sato, K. Imanaka, and S. Sugiyama, "Development of a large-force low-loss metal-contact RF MEMS switch," *Sensors and Actuators A: Physical*, vol. 132, no. 2, pp. 683 – 688, 2006.

[36] Omron Electronic Components, LLC, "RF MEMS switch," www.components.omron.com.

[37] C. D. Patel and G. Rebeiz, "RF-MEMS metal-contact switches with mN-contact and restoring forces and low process sensitivity," *Microwave Theory and Techniques, IEEE Transactions on*, vol. 59, no. 5, pp. 1230–1237, May 2011.

[38] J. Harley and T. Kenny, "A high-stiffness axial resonant probe for atomic force microscopy," *Microelectromechanical Systems, Journal of*, vol. 10, no. 3, pp. 434 –441, Sep. 2001.

[39] Coventor Inc., "Coventorware version 2008," www.coventor.com.

[40] R. Mahameed and G. M. Rebeiz, "Electrostatic RF MEMS tunable capacitors with analog tunability and low temperature sensitivity," in *IEEE MTT-S Int. Microwave Symp. Dig.*, Anaheim, CA, May 2010, pp. 1254–1257.

[41] F. P. Beer, E. R. Johnston Jr, J. T. DeWolf, and D. F. Mazurek, *Mechanics of Materials*, 5th ed. New York: McGraw Hill, 2009.

[42] X. Yan, N. McGruer, G. Adams, and S. Majumder, "Finite element analysis of the thermal characteristics of MEMS switches," in *Int. Conf. Transducers, Solid-State Sensors, Actuators and Microsystems*, vol. 1, 2003, pp. 412 – 415.

[43] Sonnet Software Inc., "Sonnet version 12.02," www.sonnetsoftware.com.

[44] S. Gong, T. Reck, and N. S. Barker, "A temperature insensitive DC-contact RF-MEMS switch," in *40th European Microwave Conference*, Paris, France, 2010, pp. 1114–1117.

[45] G.-L. Tan, R. Mihailovich, J. Hacker, J. DeNatale, and G. Rebeiz, *Microwave Theory and Techniques, IEEE Transactions on*.

[46] J. Lee, C. H. Je, S. Kang, and C.-A. Choi, "A low-loss single-pole six-throw switch based on compact RF MEMS switches," *Microwave Theory and Techniques, IEEE Transactions on*, vol. 53, no. 11, pp. 3335 – 3344, nov. 2005.

[47] Radant MEMS, Inc, "Radant MEMS switch," www.radantmems.com.

[48] C. D. Patel and G. M. Rebeiz, "A high power (>5 w) temperature stable RF MEMS metal-contact switch with orthogonal anchors and force-enhancing stoppers," in *Microwave Symposium Digest (MTT), 2011 IEEE MTT-S International*, Baltimore, MD, Jun. 2011, pp. 1 –4.

[49] ——, "An RF-MEMS switch for high-power applications," in *Microwave Symposium Digest (MTT), 2012 IEEE MTT-S International*, Montreal, Canada, Jun. 2012.

[50] A. Tazzoli, G. Cellere, E. Autizi, V. Peretti, A. Paccagnella, and G. Meneghesso, "Radiation sensitivity of ohmic RF-MEMS switches for spatial applications," in *Micro Electro Mechanical Systems, 2009. MEMS 2009. IEEE 22nd International Conference on*, Sorrento, Italy, jan. 2009.

[51] P. Voskoboynik, R. D. Joos, W. E. D. Jr., and R. B. Goldfarb, "Low magnetic moment PIN diodes for high field MRI surface coils," *Medical Physics*, vol. 33, no. 12, pp. 4499–4501, 2006.

[52] R. Stefanini, M. Chatras, P. Blondy, and G. Rebeiz, "Miniature MEMS switches for RF applications," *Microelectromechanical Systems, Journal of*, vol. 20, no. 6, pp. 1324 –1335, dec. 2011.

[53] H. Hsu, M. Koslowski, and D. Peroulis, "An experimental and theoretical investigation of creep in ultrafine crystalline nickel RF-MEMS devices," *Microwave Theory and Techniques, IEEE Transactions on*, vol. 59, no. 10, pp. 2655 –2664, oct. 2011.

[54] C. Do, M. Lishchynska, K. Delaney, P. Fitzgerald, R. Goggin, and M. Hill, "Model-based analysis of switch degradation effects during lifetime testing," in *Micro Electro Mechanical Systems (MEMS), 2012 IEEE 25th International Conference on*, Paris, France, Feb. 2012, pp. 460 –463.

[55] A. Broue, J. Bhennin, F. Courtade, C. Dieppedal, P. Pons, X. Lafontan, and R. Plana, "Characterization of gold/gold, gold/ruthenium, and ruthenium/ruthenium ohmic contacts in MEMS switches iproved by a novel methodology," *Journal of Micro/Nanolithithography, MEMS, and MOEMS*, vol. 9, no. 4, p. 041102, Dec. 2010.

[56] F. Ke, J. Miao, and J. Oberhammer, "A ruthenium-based multimetal-contact RF MEMS switch with a corrugated diaphragm," *Microelectromechanical Systems, Journal of*, vol. 17, no. 6, pp. 1447 –1459, Dec. 2008.

[57] F. F. Ling, W. M. Lai, and D. A. Lucca, *Fundamentals of Surface Mechanics with Applications*, 2nd ed. New York: Springer, 2002.

[58] S. S. Rao, *Mechanical Vibrations*, 3rd ed. Massachusetts: Addison-Wesley, 1995.

[59] Z. J. Guo, N. E. McGruer, and G. G. Adams, "Modeling, simulation and measurement of the dynamic performance of an ohmic contact, electrostatically actuated RF MEMS switch," *Journal of Micromechanics and Microengineering*, vol. 17, no. 9, p. 1899, 2007.

[60] A. Garg, V. Ayyaswamy, A. Kovacs, A. Alexeenko, and D. Peroulis, "Direct measurement of field emission current in E-static MEMS structures," in *IEEE Int. Conf. Microelectromech. Systems*, Cancun, Mexico, Jan. 2011, pp. 412–415.

[61] M. Bao and H. Yang, "Squeeze film air damping in MEMS," *Sensors and Actuators A: Physical*, vol. 136, pp. 3–27, May 2007.

[62] C. Keimel, G. Claydon, B. L., J. Park, and M. Valdes, "Micro-electromechanical-system (MEMS) based switches for power applications," in *Industrial and Commercial Power Systems Technical Conference (I CPS), 2011 IEEE*, may 2011, pp. 1 –8.

[63] L. Chow, J. Volakis, K. Saitou, and K. Kurabayashi, "Lifetime extension of RF MEMS direct contact switches in hot switching operations by ball grid array dimple design," *Electron Device Letters, IEEE*, vol. 28, no. 6, pp. 479 –481, june 2007.

[64] Teledyne Technologies, Inc, "RF power handling capability application note," www.teledynerelays.com/appnotes/RFpowerapnote.pdf.

[65] J. D. Luis, A. Morris, Q. Gu, and F. D. Flaviis, "Tunable antenna systems for wireless transceivers," in *Antennas and Propagation (APSURSI), 2011 IEEE International Symposium on*, Jul. 2011, pp. 730 –733.

[66] A. van Bezooijen, M. de Jongh, C. Chanlo, L. Ruijs, F. van Straten, R. Mahmoudi, and A. van Roermund, "A GSM/EDGE/WCDMA adaptive series-LC matching network using RF-MEMS switches," *Solid-State Circuits, IEEE Journal of*, vol. 43, no. 10, pp. 2259 –2268, Oct. 2008.

[67] B. Lacroix, A. Pothier, A. Crunteanu, C. Cibert, F. Dumas-Bouchiat, C. Champeaux, A. Catherinot, and P. Blondy, "CMOS compatible fast switching RF MEMS varactors," in *Microwave Conference, 2006. 36th European*, Sep. 2006, pp. 1072 –1075.

[68] A. Grichener and G. Rebeiz, "High-reliability RF-MEMS switched capacitors with digital and analog tuning characteristics," *Microwave Theory and Techniques, IEEE Transactions on*, vol. 58, no. 10, pp. 2692 –2701, 2010.

[69] M. A. El-Tanani and G. M. Rebeiz, "High-performance 1.5-2.5-GHz RF-MEMS tunable filters for wireless applications," *Microwave Theory and Techniques, IEEE Transactions on*, vol. 58, no. 6, pp. 1629 –1637, Jun. 2010.